AEDC-TR-72-169

HEAT-TRANSFER AND FLOW-FIELD TESTS OF THE NORTH AMERICAN ROCKWELL/ GENERAL DYNAMICS CONVAIR SPACE SHUTTLE CONFIGURATIONS

W. R. Martindale, R. K. Matthews, and L. L. Trimmer
ARO, Inc.

January 1973

VON KÁRMÁN GAS DYNAMICS FACILITY
ARNOLD ENGINEERING DEVELOPMENT CENTER
AIR FORCE SYSTEMS COMMAND
ARNOLD AIR FORCE STATION, TENNESSEE

NOTICES

When U. S. Government drawings specifications, or other data are used for any purpose other than a definitely related Government procurement operation, the Government thereby incurs no responsibility nor any obligation whatsoever, and the fact that the Government may have formulated, furnished, or in any way supplied the said drawings, specifications, or other data, is not to be regarded by implication or otherwise, or in any manner licensing the holder or any other person or corporation, or conveying any rights or permission to manufacture, use, or sell any patented invention that may in any way be related thereto.

Qualified users may obtain copies of this report from the Defense Documentation Center.

References to named commercial products in this report are not to be considered in any sense as an endorsement of the product by the United States Air Force or the Government.

HEAT-TRANSFER AND FLOW-FIELD TESTS OF THE NORTH AMERICAN ROCKWELL/ GENERAL DYNAMICS CONVAIR SPACE SHUTTLE CONFIGURATIONS

W. R. Martindale, R. K. Matthews, and L. L. Trimmer
ARO, Inc.

FOREWORD

The work reported herein was conducted by the Arnold Engineering Development Center (AEDC) at the request of the Marshall Space Flight Center (NASA-MSFC), Huntsville, Alabama, under Program Element 921E-2.

The results of tests presented were obtained by ARO, Inc. (a subsidiary of Sverdrup & Parcel and Associates, Inc.), contract operator of the AEDC, Air Force Systems Command (AFSC), Arnold Air Force Station, Tennessee. The tests were conducted in June and September 1971, under ARO Project No. VT1162. The final data package was completed on May 10, 1972. The manuscript was submitted for publication on August 1, 1972.

The authors wish to express their appreciation to Dr. J. C. Adams, Jr., for developing the flow-field and boundary-layer calculation methods and to Mr. G. E. Gilley for his efforts in developing the phase-change paint data reduction program. The above personnel are members of the Aerodynamics Division of the von Kármán Gas Dynamics Facility (VKF) of ARO, Inc.

This technical report has been reviewed and is approved.

JIMMY W. MULLINS
Lt Colonel, USAF
Chief Air Force Test Director, VKF
Directorate of Test

A. L. COAPMAN
Colonel, USAF
Director of Test

ABSTRACT

Aerothermodynamic tests of Phase B space shuttle configurations proposed by North American Rockwell/General Dynamics Convair were conducted at Mach number 8. Test conditions provided both Mach number and Reynolds number simulation for typical ascent and reentry trajectories. This report provides a comprehensive analysis of the major test results and also presents data comparisons with theoretical calculations. Specific areas covered are: ascent heating and shock interference, booster reentry heating and flow fields, and orbiter reentry including leeside heating, windward shock angles and flow fields, windward surface heating, and boundary-layer transition.

CONTENTS

APPENDIXES

I. ILLUSTRATIONS

Figure

NOMENCLATURE

BL	Boundary layer
b	Model skin thickness, ft
c	Specific heat, Btu/lbm-°R, or local wing cord, in.
H_o	Stagnation enthalpy, Btu/lbm
h	Heat-transfer coefficient, $\dot{q}/(T_o - T_w)$, Btu/ft^2-sec-°R or metric coefficient (Appendix V)
k	Conductivity of Stycast, Btu/ft-sec-°R
L	Axial length of model, in. (see Figs. 2 and 4)
M	Mach number
M^*	Local Mach number at a distance y^* from surface
n	$(d\omega/d\phi)_{\phi=0}$
p	Pressure, psia
$p_{o'}$	Stagnation pressure downstream of a normal shock, psia
$\dot{q}$	Heat-transfer rate, Btu/ft^2-sec
Re	Unit Reynolds number, ft^{-1}

$Re_{\infty, L}$	Free-stream Reynolds number based on length
$Re_{e, \theta}$	Reynolds number based on edge conditions and momentum thichness at x_t location
r	Local model span, ft
s	Surface distance normal to centerline, ft (see Fig. 4)
T	Temperature, °F or °R as noted
TC	Thermocouple
t	Time, sec
Δt	Time increment that model has been exposed to uniform flow, sec
U	Velocity, ft/sec
u	Crossflow velocity, ft/sec
v	Axial velocity, ft/sec
w	Model skin density, lbm/ft^3
X	Axial distance between orbiter and booster noses, in.
x	Axial distance from model nose or from wing leading edge, in.
$\bar{x}$	Surface distance from the model nose in the axial direction, in.
x_t	Axial distance from model nose to beginning of transition, in.
y	Distance from model surface, in.
y^*	Distance from model surface where $T_p/T_o \approx 1.0$ (see Fig. 23), in.
Z	Gap between orbiter and booster, in.
α	Angle of attack, deg
δ_s	Angle between local tangents to model surface and bow shock, deg
θ	Hemisphere angle (see Fig. II-1), deg
θ_s	Angle between free-stream velocity vector and tangent to local bow shock, deg
Λ	Sweep angle, deg
ρ	Density, lbm/ft^3

σ	Angle between model axis and local tangent to model surface, deg
ϕ	Local ray angle (see Fig. IV-1), deg
ω	Inviscid streamline angle (see Fig. IV-1), deg

SUBSCRIPTS

aw	Adiabatic wall conditions
e	Edge conditions
eq	Equivalent
i	Initial conditions
ℓ	Local conditions
o	Stilling chamber conditions
pc	Phase change
R	Rake measurement
ref	Heat-transfer parameter based on Fay-Riddell theory and a 1-ft nose radius scaled down to the model scale (i.e., 0.013 ft or 0.009 ft)
w	Wall conditions
∞	Free-stream conditions
2D	Two dimensional

SECTION I
INTRODUCTION

During the Phase B design studies of the Space Transportation System, commonly known as the Space Shuttle, a fully reusable concept requiring a booster and an orbiter was investigated by NASA. In support of the Phase B program, extensive aerothermodynamic tests of several proposed configurations were conducted at the von Kármán Facility of the AEDC. The tests were sponsored by NASA-MSFC; however, the configurations were determined by the two Phase B contractor teams which were composed of McDonnell Douglas - Martin Marietta and North American Rockwell - General Dynamics Convair. This report presents results from the North American Rockwell/General Dynamics Convair configurations. A parallel report (Ref. 1) documents test results from the McDonnel Douglas - Martin Marietta configurations. Additionally, tests of basic delta wing shapes were included in the test program, and these results will be documented in a separate report. All data generated during this test program were submitted to the NASA-sponsored "System for Automated Development of Static Aerothermodynamic Criteria" (SADSAC) and are documented in data reports (Refs. 2 through 17).

The objectives for the North American Rockwell/General Dynamics Convair configuration tests are summarized below.

1. Provide aerodynamic heating data for the ascent (launch) configuration including booster-orbiter interference effects,
2. Provide aerodynamic heating data for both booster and orbiter entry conditions, and
3. Obtain flow-field and boundary-layer transition data at reentry conditions.

To accomplish these objectives, the continuous hypersonic Tunnel B was used. Tunnel B was chosen because of its unique combination of high data quality, high productivity, and large model size capability. The test conditions for Tunnel B are compared with representative Space Shuttle trajectories in Fig. 1 (Appendix I).

Heat-transfer rates were determined using the phase-change paint technique on 0.013-scale ascent and orbiter reentry models and by using the thin-skin thermocouple technique on 0.009-scale reentry models. The nominal test conditions were Mach number 8 and free-stream Reynolds numbers, based on model length, from 1.4 million to 9 million. To produce a maximum amount of fully turbulent flow on

the reentry models, boundary-layer trips were used during some of the tests. Model surface pressures and flow-field pressure and temperature data were obtained for the 0.013-scale orbiter.

In addition to the experimental program described above, a parallel analytic research program was conducted by the VKF under Air Force sponsorship. One particularly valuable result of this research was the development of a prediction technique for the laminar and turbulent windward surface heating of space shuttle configurations at large angles of attack. These predictions are compared with the experimental results from the present program in this report while a thorough description of the analytical procedures and additional data comparisons are presented in Ref. 18.

SECTION II
APPARATUS

2.1 MODELS

2.1.1 Phase-Change Paint Models

Model drawings were provided ARO, Inc. by the appropriate contractors, and fabrication of the 0.013-scale Stycast models was subcontracted to the Grumman Aerospace Corporation. A sketch of the booster model is shown in Fig. 2, and a photograph is shown in Fig. 3. Two phase-change paint orbiter models were fabricated to improve utilization of the wind tunnel. The models were geometrically the same, but one had a 1.0-in.-long steel nose and 10 windward centerline pressure orifices. A sketch showing overall orbiter model dimensions is shown in Fig. 4, and a photograph is shown in Fig. 5. A photograph of the booster and orbiter in the mated (launch) configuration is shown in Fig. 6. Additional booster and orbiter configuration details may be found in the SADSAC data reports (Refs. 14 and 15).

The phase-change paint technique which was selected to provide heat-transfer-rate measurements requires a model material of relatively low thermal diffusivity to permit extraction of accurate heating data. The data are reduced by assuming that the model is a thermally semi-infinite slab. Several materials have been used in wind tunnel tests which satisfy the semi-infinite slab requirement (within reasonable limits of time and material thickness). Probably the most commonly used material at the present is Stycast®, which is a filled, high-temperature epoxy. Stycast 2762 was selected as the model material for the present tests because of its proven performance.

One important requirement for phase-change paint data reduction is knowledge of the model material thermophysical properties. To provide this information for these models, two approaches were taken. First, a laboratory analysis of samples of the material was made; second, 6-in.-diam hemispheres were cast from the same batch of Stycast used to cast each model. Calibration runs were made during the tests with each hemisphere model. The results of these tests are discussed in Appendix II.

Chromel®-Alumel® thermocouples were cast into all the Stycast models approximately 1/8 in. from the surface to measure the initial model temperature.

2.2.1 Thermocouple Models

The thermocouple booster model was a 0.009-scale replica of the Convair B-15B-2 delta-wing booster furnished by the Convair Aerospace Division of General Dynamics Corporation. It was machined from 17-4PH steel to a nominal skin thickness of 0.04 in. A model photograph is shown in Fig. 7.

The orbiter model was a 0.009-scale replica of the North American Rockwell 9992-161B delta-wing orbiter and was furnished by North American Rockwell. It was machined from 17-4PH steel to a nominal skin thickness of 0.04 in. A model photograph is shown in Fig. 8.

The booster model was instrumented with 342 iron-constantan thermocouples of which 184 were used during the mated tests and 291 were used during the reentry tests. The orbiter model was instrumented with 204 iron-constantan thermocouples of which 97 were used during the mated tests and 193 were used during the reentry tests. The locations of the thermocouples and configuration geometry details are given in Refs. 9, 10, and 11.

2.2 WIND TUNNEL

Tunnel B is a continuous, closed-circuit, variable density wind tunnel with an axisymmetric contoured nozzle and a 50-in.-diam test section. The tunnel can be operated at nominal Mach numbers of 6 and 8 at stagnation pressures from 20 to 300 and 50 to 900 psia, respectively, at stagnation temperatures up to 1350°R. The model can be injected into the tunnel for a test run and then retracted for model cooling or model changes without interrupting the tunnel flow. The present tests were performed at a nominal Mach number of 8.

SECTION III
PROCEDURES

3.1 TEST CONDITIONS

The nominal test conditions for each phase of the test are shown below. The specific test conditions and tabulated data are documented in the series of SADSAC reports (Refs. 9 through 15).

Test Phase	Model Scale	Reference Length, in.	p_o, psia	T_o, °R	$Re_\infty \times 10^{-6}$ Ft^{-1}	$Re_{\infty,L} \times 10^{-6}$	α, deg	Data Type
Ascent	0.009	27.04	150	1235	0.8	1.7	-5, 0, 5	TC, S
			860	1340	3.7	8.4	-5, 0, 5	TC, S
	0.013	39.05	265	1270	1.3	4.1	-5, 0, 5	P
			570	1310	2.6	8.4	-5, 0, 5	P, S
Booster Reentry	0.009	24.82	860	1340	3.7	7.7	0, 10, 20, 30, 40, 50, 60	TC, S
Orbiter Reentry	0.009	20.01	165	1240	0.8	1.4	10, 20, 30	TC, S
			555	1310	2.5	4.2	10, 20, 30, 40, 50	TC, S
			860	1340	3.7	6.2	10, 20, 30, 40, 50	TC, S
			860	1340	3.7 (trips)	---	10, 30, 40, 50	TC, S
	0.013	28.90	555	1310	2.5	6.1	10, 20, 30, 40	P, S
			860	1340	3.7	9.0	10, 20, 30, 40, 50	P, S, SP, FF
			860	1340	3.7 (trips)	---	10, 20, 30, 40, 50	P, S

TC - Thermocouple
SP - Surface Pressure
FF - Flow Field
P - Phase-Change Paint
S - Snadowgraph

Uncertainty in the basic tunnel flow parameters p_o, T_o, and p_o' was estimated from repeat calibrations of the instrumentation and from repeatability and uniformity of the test section flows during tunnel calibrations. The individual contributions of these uncertainties were propagated through the appropriate flow equations to obtain the remaining uncertainties.

Approximate uncertainties in tunnel flow conditions are:

Parameter	Uncertainty, percent
p_o	±0.5
p_o'	±0.3
T_o	±1.0

Parameter	Uncertainty, percent
M_∞	±0.3
p_∞	±2.0
ρ_∞	±1.1
U_∞	±0.5
H_O	±1.4
h_{ref}	±1.0
Re_∞	±2.0

3.2 TEST PROCEDURES AND DATA REDUCTION

3.2.1 Phase-Change Paint Data

The phase-change paint technique of obtaining heat-transfer data uses an opaque coating which changes phase from a solid to a liquid (melts) at a specific temperature. Tempilaq®, a paint consisting of calibrated melting point materials suspended in an inert carrier, was used as the phase-change indicator. The specific melting temperatures of the Tempilaq paints used were 100, 113, 125, 150, 156, 175, 200, 225, 250, 300, 350, 400, and 500 degrees Fahrenheit. Uncertainties in the phase-change temperatures are estimated by the manufacturer to be ±1 percent.

The primary data were obtained by photographing the progression of the melt lines with 70-mm sequenced cameras. During the ascent phase of the test, one camera was mounted in the top window of the tunnel and two in the upstream side window. During the reentry phase, three sides of the model were photographed simultaneously with cameras mounted in the top and side windows and with the third camera underneath in the model injection tank. The cameras used Kodak® TRI-X Pan black-and-white film, and the time from the start of model injection, and of each shutter opening, was recorded on magnetic tape. The cameras were operated nominally at two frames/sec.

Backup data were obtained with 16-mm motion-picture cameras. These cameras were operated at 24 frames/sec, and Kodak Ektachrome EF color film was used. The models were lighted with fluorescent light banks.

Prior to each run, the model was cleaned and cooled with alcohol and then spray painted with Tempilaq. The models were installed on

the model injection mechanism at the desired test attitude and the model initial temperature was measured with a thermocouple probe or with the model-embedded thermocouples. During the course of the test, many of the embedded thermocouples became inoperative and the probe was generally used to determine the model initial temperature. The model was then injected into the airstream for approximately 20 sec and during this time the model surface temperature rise produced isotherm melt lines.

Since the maximum available Reynolds number was not sufficient to produce fully turbulent flow, boundary-layer trips were used to induce transition during the reentry phase so that turbulent heating levels could be determined. For angles of attack of 30 deg and higher, the trip application method consisted of dabbing small dots of Barco Bond® adhesive in about 1-in. intervals on the bottom surface of the model and then sprinkling the surface with No. 46 grit (≈0.015-in. diam). Several pieces of grit adhered to each dot, resulting in a small surface irregularity approximately 0.025 in. high.

For angles of attack of 10 and 20 deg, the grit did not trip the boundary layer. For these angles, 0.030-in.-diam steel spheres were welded about one diameter apart on the steel nose cap of the orbiter paint model.

The data reduction procedures used were somewhat more involved than previously used for paint data since the melt lines were transformed into body coordinates and were then associated with the corresponding heat-transfer coefficient.

During each run, the tunnel conditions and time of each picture were recorded on magnetic tape. The heat-transfer coefficient for each picture was calculated from the semi-infinite slab transient heat conduction equation.

$$\frac{T_{pc} - T_i}{T_{aw} - T_i} = 1 - e^{\beta^2} \operatorname{erfc} \beta$$

where $\beta = \dfrac{h\sqrt{\Delta t}}{\sqrt{\rho ck}}$ and $\sqrt{\rho ck} = 0.11 - 0.008\sqrt{\Delta t}$

The equation for the thermal properties ($\sqrt{\rho ck}$) of Stycast was obtained by evaluation of a considerable amount of hemisphere calibration data and supplemented by VKF laboratory measurements (Appendix II). The indicated variation of properties with time is actually due to nonuniformities of the material in the direction normal to the wall.

Heat-transfer coefficients were calculated for assumed adiabatic wall temperatures of T_o, $0.9T_o$, and $0.85T_o$ (see tabulated data sheets in Refs. 9 through 15). The use of three values of T_{aw} provides an indication of the sensitivity of the heat-transfer coefficient (h) to the values of T_{aw} assumed. For the sake of consistency, all plots and melt lines in this report are based on $T_{aw} = T_o$. A discussion of other assumptions associated with the phase-change paint technique is presented in Appendix III.

All heat-transfer coefficients were nondimensionalized by dividing by the stagnation point heat-transfer coefficient (Ref. 19) on a 1-ft radius sphere scaled down by the model scale (0.013 ft or 0.009 ft).

The transformation of the melt line coordinates as viewed by the camera (picture plane) to heat-transfer coefficients in model coordinates is discussed below. The 70-mm film was projected onto an 8-by10-in. glass plate, and an experienced engineer traced the melt line contours and recorded them on magnetic tape. In regions of relatively constant heating, a distinct melt line is frequently difficult to define, and in some cases, the melt line tracings were terminated because of poor definition. Of course, the melt line tracings are in picture plane coordinates, whereas body coordinates are desired. The transformation of body coordinates was accomplished as follows:

1. The model surface coordinates were measured at many model stations with a modified Sheffield Cordax coordinate measuring machine (Model 200);
2. The camera location relative to the model was determined;
3. Using the principles of photogrammetry and the information obtained in steps 1 and 2, the model coordinates were transformed into the picture plane;
4. The body coordinates of a given melt line were then obtained by interpolation in the picture plane, with the results being stored on magnetic tape.

The level of the heat-transfer coefficient associated with each melt line was obtained by the solution of the semi-infinite slab conduction equation as previously discussed. With the level and location of the heat-transfer coefficients stored on magnetic tape, any desired machine-generated plot with the limits of available data can be produced. Much of the phase-change paint data in this report are presented as data fairings obtained from machine-generated plots.

3.2.2 Thermocouple Data

Thermocouple outputs were recorded on magnetic tape by a Beckman 210 digital data system at the rate of 20 times per second from the start of the model injection cycle until about 5 seconds after the model reached tunnel centerline. After each injection the model was cooled to an isothermal state prior to the next injection.

The reduction of thin-skin thermocouple data normally involves only the calorimetric heat balance which, in coefficient form, is:

$$h = wbc \frac{dT_w/dt}{T_o - T_w} \tag{1}$$

Radiation and conduction losses are neglected in this heat balance, and data reduction simply requires evaluation of dT_w/dt from the temperature-time data and determination of model properties. For the present tests, radiation effects were negligible; however, conduction effects were significant in several regions of the models. To permit identification of these regions and improve evaluation of the data, the following procedure was used.

Separation of variables and integration of Equation (1) assuming constant w, b, c, and T_o yields

$$\frac{h}{wb\,c}(t - t_i) = \ell n \left(\frac{T_o - T_{wi}}{T_o - T_w}\right) \tag{2}$$

Since $\frac{h}{wb\,c}$ is a constant, plotting $\ell n \left(\frac{T_o - T_{wi}}{T_o - T_w}\right)$ versus time gives a straight line if conduction is negligible. Thus, deviation from a straight line can be interpreted as a conduction effect.

The data were evaluated in this manner and generally a reasonably linear portion of the curve could be found for all thermocouples. For high heating rates, such as experienced in the nose, leading edge, and interface regions, the linear portion was quite short. A linear least squares curve fit of

$$\ell n \left(\frac{T_o - T_{wi}}{T_o - T_w}\right)$$

versus time was applied to the data beginning at the time when the model reached uniform flow and extending for a time span which was a function of the heating rate as shown below:

Heating Rate, °R/sec	Time Span of Data Used, sec	Number of Data Points Used
$16 \leq dT_w/dt$	0.2	5
$4 \leq dT_w/dt < 16$	0.4	9
$2 \leq dT_w/dt < 4$	0.6	13
$dT_w/dt < 2$	1.0	21

In general, the above time spans were adequate to keep the evaluation of the right side of Equation (2) within the linear region. Strictly, the value of c is not constant as assumed and the relation

$$c = 0.0608 + 1.295 \times 10^{-4} T_w - 6.35 \times 10^{-8} T_w^2 \qquad (3)$$

was used with the value of T_w at the midpoint of the curve fit. The maximum variation of c over any curve fit was less than one percent; thus the assumption of constancy was not grossly violated. A constant 485 Lb_m/ft^3 was used for w and measured values of b for each thermocouple were used.

At angles of attack of 30 deg and above the application of boundary-layer trips was the same as for the phase-change paint model. For the 10-deg case a thin uniform coat of Barco Bond adhesive was applied to the nose region. No. 20 grit (≈0.043-in. diam) was then sprinkled on the surface resulting in a uniformly roughened nose.

3.2.3 Pressure Data

Orbiter centerline static pressures and flow-field surveys were obtained at the conditions outlined in Section 3.1. Static-pressure orifice locations are shown in Fig. 4, and details of the survey rake are shown in Fig. 9. The static pressures were measured with 15-psid transducers referenced to a near vacuum while the rake pressures required an atmospheric reference in some cases. From repeat calibrations, the estimated pressure measurement precision is ±0.003 psia or ±0.5 percent, whichever is greater.

The model flow field was surveyed with pitot-pressure and single-shield total-temperature probe rakes. The rakes were mounted so that pressure and temperature measurements could be made simultaneously.

By assuming the flow-field static pressure equal to the wall static pressure, the local Mach number (M_ℓ) was calculated from the Rayleigh pitot formula,

$$\frac{p_R}{p_\ell} = \left(\frac{6M_\ell}{5}\right)^{7/2} \left(\frac{6}{7M_\ell^2 - 1}\right)^{5/2} \quad \text{for } M_\ell \geq 1$$

or from the compressible Bernoulli equation,

$$\frac{p_R}{p_\ell} = (1 + 0.2\ M_\ell^2)^{7/2}, \quad \text{for } M_\ell < 1.$$

In general, the assumption of constant static pressure becomes less valid as the distance from the model surface increases.

Estimated uncertainties of the primary measurements are given below:

Parameter	Uncertainty
p_ℓ	±1.0 percent
p_R	±0.015 psia (for $p_R \leq$ 15 psia)
	±0.021 psia (for $p_R >$ 15 psia)
T_R	±2.0 percent

SECTION IV
RESULTS AND DISCUSSION

4.1 ASCENT

The space shuttle Phase B design studies were being completed during the time period of these tests and shortly thereafter the fully reusable, flyback, two-stage system was abandoned by NASA. At present, a water recovery of an unmanned booster is planned and the orbiter, while retaining its basic delta wing shape, is about two-thirds the size of the Phase B orbiter. The use of external fuel tanks for the orbiter ascent engines has made this size reduction possible without serious compromise of the payload capabilities.

In light of these developments, much of the data obtained from these tests must be considered academic. However, in the course of testing and data analysis, a wealth of knowledge which can be applied to future programs was accumulated. With these facts in mind, the major objective of this report is to review the basic results and the techniques employed during the course of the test program.

The ascent configurations tested consisted of 0.009-scale thermocouple models (Figs. 7 and 8) and 0.013-scale phase-change paint models (Fig. 6). The relative positioning of the models was:

	X, in. Orbiter to Booster Nose Distance	Z, in. Gap Between Models
Thermocouple Models (0.009)	2.22	~ 0.23
Phase-Change Paint Models (0.013)	3.21	~ 0.31
X/L and Z/L	0.089	~ 0.009

During the thermocouple model tests, these parameters were varied, but no significant trends were observed. A complete set of the data and additional model information are presented in Refs. 9, 11, 14, and 15.

Because of the complexity of the ascent configurations, the phase-change paint data are illustrated by presentation of the data photographs. Typical phase-change paint photographs are presented in Figs. 10 through 13, and, of course, the heat-transfer-rate ratios shown apply only to the melt lines in the corresponding photographs. The hotter regions are vividly depicted as the white paint melts and the black model shows through. Each figure presents four sequential photographs, hence four levels of heat-transfer rate ratios (h/h_{ref}). In most cases, at least two different paint temperatures were required to span the range of (h/h_{ref}) shown.

As expected, the leading edges and noses were regions of relatively high heating ($h/h_{ref} \approx 0.241$, Fig. 10). Shock interference produced relative "hot spots" in several other areas on both models. In the third picture of Fig. 10 ($h/h_{ref} = 0.113$) "hot spots" were observed in the region between the models and on the orbiter side panel. In fact, inspection of the first picture in Fig. 10 ($h/h_{ref} = 0.501$) reveals that the paint melted in the interference region (between the configurations) before melting on the leading edges, implying higher heating. The orbiter canopy was obviously another region of relatively high heating.

The photographs presented in Fig. 10 were obtained at a Reynolds number of 1.3×10^6 ft^{-1}, while those of Fig. 11 correspond to a Reynolds number of 2.5×10^6 ft^{-1}. Comparison of the melt patterns of these two figures does not indicate any detectable Reynolds number effect. The last photograph of Fig. 11 ($h/h_{ref} = 0.024$) shows heating patterns downstream of the booster canard. Comparison of this picture with those of Figs. 12 and 13 illustrates the effect of angle of attack on the shape of this melt pattern. In some of these photographs the streaks caused by melted paint provide an indication of the local flow direction.

Bow shock interference heating patterns on both the booster and orbiter models are also evident in these figures. Plots of the booster top centerline heating distribution and orbiter bottom centerline heating distribution which show the effects of interference heating are presented in Figs. 14 and 15, respectively. In these figures thermocouple data and phase-change paint data are used to complement each other and provide a complete representation of the heating distributions. Agreement of the levels of the thermocouple and phase-change paint data helps to substantiate the phase-change paint data, and the phase-change paint data were used to obtain more complete distributions and the location of peak heating rates.

The booster centerline heating (Fig. 14) shows that two peaks exist with the first peak at $x/L \approx 0.08$ being about five times higher than the booster-alone data (flagged symbols), and the second peak at $x/L \approx 0.16$ being about fifteen times higher than the noninterference data. It is interesting to note that the second peak was obtained from the thermocouple data, not from the phase-change paint data. This is because of the difficulty in seeing between the models, which, of course, is required to obtain data from the phase-change paint photographs.

The orbiter centerline heating is presented in Fig. 15, and here the value of the phase-change paint data is clearly illustrated. The thermocouple instrumentation happened to be located in a region of relatively low interference heating at $x/L = 0.3$, and only one peak is indicated by the fairing of the thermocouple data. However, the phase-change paint data show two peaks and clearly illustrate that the fairing of the thermocouple data could lead to erroneous conclusions. Unfortunately, the maximum value of the first peak was not obtained, but the implication is that the level was about 100 times the noninterference data (flagged symbols). The second peak appears to be approximately twenty times higher than the noninterference data. The thermocouple noninterference data were influenced by Reynolds number; however, no measurable Reynolds number effects could be detected from the phase-change paint data, and the data shown represent all the paint data.

The shadowgraph picture presented in Fig. 16 shows the bow shock interactions which caused the high interference heating of the previous two figures. Edney (Ref. 20) classified shock interference patterns, and the associated heating amplifications, into six types. The initial bow shock intersection between the models shown in Fig. 16 can be classified as Type I which was associated with a heating amplification factor of 10. The present heating amplification on the booster was of a similar magnitude (5 for first peak, 15 for second peak). However, the amplification factor of the first peak on the orbiter (~100) is considerably higher. The probable reason for the difference in amplification factors can be determined by inspection of the shadowgraph picture (Fig. 16). The shock impingement on the orbiter is significantly downstream of that of the booster and probably should not be classified as Type I because of the complex interaction of the reflected shocks. The implication is that the local geometry and relative location of the bow shock intersection can significantly affect interference heating amplification factors.

4.2 BOOSTER REENTRY

The 0.009-scale thermocouple booster model was tested at simulated reentry conditions. The complete set of data may be found in Ref. 10. Windward fuselage centerline heating rates at angles of attack of 0, 20, 40, and 60 deg are shown in Fig. 17. Also shown are heating rate calculations from the three-dimensional boundary-layer theory of Ref. 18. A parallel shock flow field was assumed and the centerline velocity gradients were obtained from Newtonian theory in the nose region, the method of integral relations of Ref. 21 in the canard region (see Fig. 2), and the experimental data correlation of Ref. 22 for the rest of the body.

Comparison of untripped data with laminar theory (Figs. 17b, c, d) is good over the forward portion of the body. The slight rise in the calculated heat-transfer coefficient between x/L values of 0.20 and 0.35 is caused by a change in the body cross section, and the data tend to confirm this trend, especially at 20- and 40-deg angles of attack. The deviations from laminar values over the last half of the body at α = 20, 40, and 60 deg are attributed to transition to turbulent flow. However, only for the 60-deg angle-of-attack case was transition apparently completed and the fully turbulent value reached.

At α = 40 and 60 deg, boundary trips were used to induce fully turbulent flow and the resulting data (Figs. 17c and d) are in excellent agreement with turbulent theory (Ref. 18). There is good agreement

at x/L values of 0.7 to 0.9 (wing region) even though the theory of Ref. 18 is not strictly applicable in this region.

Windward heat-transfer coefficients on the booster wing at quarter span are shown in Fig. 18 for angles of attack of 0, 20, 40, and 60 deg. The 20-, 40-, and 60-deg untripped data exhibit somewhat irregular trends with angle of attack which were probably caused by the combined effects of complex flow and boundary-layer transition. The boundary-layer tripped data at 40- and 60-deg angles of attack are more regular and are higher than the untripped data, probably indicating that turbulent flow was achieved. Note the convergence of the tripped and untripped data at the back of the wing which also confirms the existence of turbulent flow in this region. The bump in the data at $x/L \approx 0.9$ may have been caused by the elevon joint which was just upstream of this location.

Leeward centerline heat-transfer coefficients for angles of attack of 0, 20, 40, and 60 deg are shown in Fig. 19. These heating distributions are similar in character to those shown in Fig. 12 of Ref. 23 for a space shuttle configuration and for a blunted cone. The erratic behavior of these data was attributed to vortex interaction with the lee side boundary layer. The result of this apparent vortex interaction in the present tests was heating levels higher than the zero angle-of-attack values at the higher angles of attack and x/L greater than 0.35.

Heat-transfer coefficients on the lee side of the booster wing at quarter span are shown in Fig. 20. These heating rates were generally quite low but once again were sometimes higher than the zero angle-of-attack values for $\alpha > 40$, possibly indicating vortex interaction effects.

4.3 ORBITER REENTRY

The orbiter reentry tests used both the 0.009-scale, thin-skin thermocouple model (Fig. 8) and the 0.013-scale, phase-change paint models (Fig. 5). In addition to heat transfer, measurements included windward centerline shock angle, surface pressures, and flow-field pitot pressure and total temperature. The complete results from these tests may be found in Refs. 11, 12, and 13.

Experimental shock angles presented in terms of the incremental angle between the local body slope and the local shock angle are shown in Fig. 21. Local body slopes are shown at the bottom of the figure. Also shown are shock angles obtained from tangent cone theory. The agreement is good except for values of x/L greater than 0.8 where the body curves away from the flow.

In Fig. 22 experimental centerline surface pressures are compared with tangent cone and modified Newtonian values. For values of x/L less than 0.8, the data are in good agreement with tangent cone theory. In the expansion region (x/L greater than 0.8) the data are in better agreement with modified Newtonian theory except for the 10-deg angle-of-attack case.

Orbiter windward centerline flow-field data were obtained at four model stations (x/L = 0.3, 0.5, 0.7, and 0.9) and angles of attack of 10, 20, 30, and 40 deg. Typical flow-field measurements are shown in Fig. 23 for α = 10 deg and x/L = 0.7. These profiles are representative of the case where the nose shock-induced entropy layer has not been completely absorbed by the boundary layer. To approximate the lower bound of inviscid flow, a value y* was defined as the minimum value of y where $T_R/T_o \approx 1.0$. The actual boundary-layer thickness may be slightly less than y*, since continuous profiles would be required to precisely define the boundary-layer thickness. The need for both pressure and temperature measurements for boundary-layer definition is well demonstrated by these data, since it would be impossible to locate the boundary-layer edge with only the pitot pressure measurements. The measured pitot pressure at y* and the local surface pressure at the corresponding station were then used to calculate M*, the local flow-field Mach number. These Mach numbers are presented in Fig. 24 and show good agreement with tangent cone theory except for α = 10 deg where the theoretical values are slightly high (≈10 percent).

Orbiter windward centerline heat-transfer measurements are compared with theoretical calculations (Appendixes IV and V) in Fig. 25. Laminar, transitional, and turbulent data are shown. Reasonable agreement between the phase-change paint and thermocouple data is shown for the laminar results at α = 10 deg (Fig. 25a). The laminar theory is low in the nose region and high on the aft portion. These disagreements are attributed to violations of the conical and two-dimensional flow assumptions made (see Appendix IV). Transitional data, indicated by a departure from the laminar level, were obtained with both models, and excellent agreement is noted between the two at $Re_{\infty, L} = 6.2 \times 10^6$.

Fully turbulent data were obtained over a large portion of the windward surface of the 0.013-scale paint model at α = 10 deg (Fig. 25a) by the use of boundary-layer trips. The use of trips on the 0.009-scale model (in this case No. 20 grit on the nose only) only moved transition to x/L ≈ 0.4 at this angle of attack. Agreement with the turbulent theory (Ref. 18) is reasonably good; however, it is noted that the paint data were consistently 20 percent higher than theory, whereas the

thermocouple data (tripped, $x/L > 0.7$) agreed almost exactly with the theory. The paint data in this case were obtained very early in the test run ($\Delta t \approx 3$ sec) and may be subject to errors, as discussed in Appendix III. The paint data wall temperatures listed in the figure correspond only to the conditions at the time and location at which the data point was read. Hence, wall temperature gradients along the body existed. The effect of axial temperature gradients on heat-transfer distributions can be significant, as discussed in Ref. 24.

The laminar data and theory are in good agreement at $\alpha = 20$ deg, as shown in Fig. 25b. No reliable turbulent data were obtained for this attitude; hence, verification of the turbulent theory was not possible.

Windward centerline heating rates at $\alpha = 30$, 40, and 50 deg are shown in Figs. 25c, d, and e. In general, the cross-flow theory used for both the laminar and turbulent calculations is in excellent agreement with the data. The agreement extends even beyond $x/L = 0.6$ where the body cross section changes rapidly in the axial direction, because of the wing, which violates the two-dimensional swept cylinder approximation used by the theory (Ref. 18).

The very rapid transition from laminar to turbulent heating levels measured on the thermocouple model at $\alpha = 40$ and 50 deg and $Re_{\infty, L} = 6.2 \times 10^6$ (Figs. 25d and e) may have been caused by a small step in the model surface caused by a joint at $x/L = 0.55$. At the higher angles of attack the windward surface boundary layer becomes quite thin; hence, it is concluded that surface roughness which did not trip the flow at lower angles of attack may have done so as the boundary layer thinned.

A correlation of boundary-layer transition data from Figs. 17 and 25 is presented in Fig. 26 in terms of the Kipp-Masek (Ref. 24) correlation parameter. The data tend to fall on or above the correlation curve except for cases where unintentional boundary-layer tripping was suspected. The boundary-layer momentum thickness and edge conditions were obtained by the same methods used to calculate the heating rates presented earlier.

Windward heating data on the orbiter wing at quarter span are shown in Fig. 27 for angles of attack of 10, 30, and 50 deg. As in the booster case, the boundary-layer trips appeared to be successful in promoting fully turbulent flow. Note in particular the excellent agreement between the tripped and untripped data for $x/L \geq 0.4$ at $\alpha = 50$ deg (Fig. 27c).

Typical side-view phase-change paint photographs of the orbiter are shown in Fig. 28. A "hot streak" emanating from the wing-body junction is clearly evident, particularly at α = 30. These photographs illustrate the usefulness of the phase-change paint technique, since it would be very difficult to resolve these complex patterns using the thermocouple technique. Examples of phase-change paint photographs of the lee surface of the orbiter are shown in Fig. 29. Note once again the complexity of the heating patterns, particularly around the canopy and centerline area.

Leeward centerline data from the phase-change paint and thermocouple techniques are presented in Fig. 30. Good agreement between the two techniques is evident except at α = 50 deg (Fig. 30e). The canopy region ($0.2 < x/L < 0.3$) is clearly a "hot spot" at all angles of attack, and the peak heating rates were generally recorded by the paint technique. Note that a peak was measured by the paint at $x/L \approx 0.45$ and α = 10 deg (Fig. 30a) which was essentially missed by the thermocouple placement. Reynolds number effects on the lee side heating were generally evident in the thermocouple data between the lower Reynolds number, 1.4×10^6 and 6.1×10^6. The variations in heating in the nose region ahead of the canopy ($x/L < 0.2$) with Reynolds number are consistent with the results of Ref. 23.

Leeward heating rates at quarter span of the orbiter wing are shown in Fig. 31. Very low rates are seen for the 30- and 50-deg cases. These data appear to be very similar to those obtained for the booster (Fig. 20).

SECTION V
SUMMARY OF RESULTS

Extensive wind tunnel tests of the North American Rockwell/General Dynamics Convair space shuttle configurations have been conducted at the von Kármán Gas Dynamics Facility of the Arnold Engineering Development Center (AEDC). The tests were conducted in Tunnel B at Mach number 8. The major results of these tests are presented below.

Ascent Phase

1. "Hot spots" ($h/h_{ref} > 0.2$) were observed between the models and on the side of the orbiter.

2. Comparison of phase-change paint and thermocouple data on the booster centerline showed reasonable agreement, the peak value being 5 to 15 times higher than the booster-alone values.

3. Comparison of phase-change paint and thermocouple data for the orbiter centerline indicated that the phase-change paint data gave better resolution of the peak heating values, and the levels were from 20 to 100 times the orbiter-alone values.

Booster Reentry

4. Boundary-layer trips were successfully used to provide fully turbulent flow over the entire lower surface.

5. Three-dimensional boundary-layer theory from Ref. 18 was in excellent agreement with both laminar and fully turbulent data.

6. Trends in leeward heating rates were similar to those shown in Ref. 23, which were attributed to vortex interaction effects.

Orbiter Reentry

7. The angle between the local body slope and the shock wave agreed well with tangent cone theory.

8. Centerline surface pressure distributions agreed well with tangent cone theory except in the expansion region at the rear of the body.

9. Windward centerline thermocouple heating data were in excellent agreement with theoretical calculations except at a 10-deg angle of attack.

10. Untripped transition data fell on or above the Kipp-Masek correlation curve of Ref. 24.

11. "Hot streaks" were observed on the orbiter side panel emanating from the wing body junction.

12. Leeward centerline heating measurements from the phase-change paint and thermocouple techniques were in general agreement, and high rates were measured in the canopy region.

REFERENCES

1. Matthews, R. K., Eaves, R. H., Jr., and Martindale, W. R. "Heat Transfer and Flow-Field Tests of the McDonnell Douglas-Martin Marietta Space Shuttle Configurations." AEDC-TR-(to be published).

2. Matthews, R. K., Martindale, W. R., and Warmbrod, J. D. "Heat Transfer Tests of the McDonnell Douglas Delta Wing Orbiter Mated with -17A Booster at Mach Number 8." NASA CR-120, 067, May 1972.

3. Mattews, R. K., Martindale, W. R., and Warmbrod, J. D. "Heat Transfer Test of the McDonnell Douglas Delta Wing Orbiter and the -17A Booster (not Mated) at Mach Number 8." NASA CR-120, 068, May 1972.

4. Matthews, R. K., Martindale, W. R., and Warmbrod, J. D. "Heat Transfer Rate Distributions on McDonnell Douglas Booster Determined by Phase Change Technique for Nominal Mach Number of 8." NASA CR-120, 043, April 1972.

5. Matthews, R. K., Martindale, W. R., and Warmbrod, J. D. "Surface Pressure and Inviscid Flow Field Properties McDonnell Douglas Booster at a Nominal Mach Number of 8." NASA CR-120, 047, March 1972.

6. Matthews, R. K., Martindale, W. R., and Warmbrod, J. D. "Heat Transfer Rate Distribution on McDonnell Douglas Delta Wing Orbiter Determined by Phase-Change Paint Technique for Nominal Mach Number of 8." NASA CR-120, 025, July 1972.

7. Warmbrod, J. D., Martindale, W. R., and Matthews, R. K. "Surface Pressure and Inviscid Flow Field Properties of the McDonnell Douglas Delta-Wing Orbiter for Nominal Mach Number of 8." NASA CR-120, 037, January 1972.

8. Eaves, R. H., Buchanan, T. D., and Warmbrod, J. D. "Heat Transfer Investigation of the McDonnell Douglas Delta Wing Orbiter at a Nominal Mach Number of 10.5." NASA-CR-120, 024, May 1972.

9. Warmbrod, J. D., Martindale, W. R., and Matthews, R. K. "Heat Transfer Rate Measurements on Convair Booster (B-15B-2) and North American Rockwell Orbiter (161B) at Nominal Mach Number of 8." NASA CR-120, 009, November 1971.

10. Warmbrod, J. D., Martindale, W. R., and Matthews, R. K. "Heat Transfer Rate Measurements on Convair Booster (B-15B-2) at Nominal Mach Number of 8." NASA-CR-119, 987, November 1971.

11. Warmbrod, J. D., Martindale, W. R., and Matthews, R. K. "Heat Transfer Rate Measurements on North American Rockwell Orbiter (161B) at Nominal Mach Number of 8." NASA CR-120, 029, December 1971.

12. Matthews, R. K., Martindale, W. R., and Warmbrod, J. D. "Heat Transfer Rate Distribution on North American Rockwell Delta Wing Orbiter Determined by Phase Change Paint Technique at a Mach Number of 8." NASA-CR-120, 048, March 1972.

13. Matthews, R. K., Martindale, W. R., and Warmbrod, J. D. "Surface Pressure and Inviscid Flow Field Properties of the North American Rockwell Delta-Wing Orbiter for Nominal Mach Number of 8." NASA-CR-120-046, March 1972.

14. Matthews, R. K., Martindale, W. R., and Warmbrod, J. D. "Ascent Heat Transfer Rate Distributions on Tests of the NR Delta Wing Orbiter and GD/C Booster at Mach Number 8 (Mated)." NASA CR 120, 049, July 1972.

15. Matthews, R. K., Martindale, W. R., and Warmbrod, J. D. "Ascent Heat Transfer Rate Distributions on the NR Delta Wing Orbiter and the GD/C Booster at Mach Number 8 (not Mated)." NASA CR 120, 071, July 1972.

16. Matthews, R. K., Martindale, W. R., Warmbrod, J. D., and Johnson, C. B. "Heat Transfer Investigation of Langley Research Center Transition Models at a Mach Number of 8." NASA CR-120, 045, March 1972.

17. Eaves, R. H., Buchanan, T. D., Warmbrod, J. D., and Johnson, C. B. "Heat Transfer Investigation of Two Langley Research Center Delta Wing Configurations at a Mach Number of 10.5." NASA CR-120, 036, March 1972.

18. Adams, John C., Jr. and Martindale, William R. "Hypersonic Lifting Body Windward Surface Flow-Field Analysis for High Angles of Incidence." AEDC-TR-(to be published).

19. Fay, J. A. and Riddell, F. R. "Theory of Stagnation Point Heat Transfer in Dissociated Air." Journal of Aerospace Sciences, Vol. 25, No. 2, pp. 73-85, 121, February 1958.

20. Edney, Barry E. "Shock Interference Heating and the Space Shuttle." NASA TMX-52876, Vol. I, July 1970.

21. South, Jerry C., Jr. "Calculation of Axisymmetric Supersonic Flow Past Blunt Bodies with Sonic Corners, Including a Program Description and Listing." NASA TN D-4563, May 1968.

22. Stallings, Robert L., Jr. "Experimentally Determined Local Flow Properties and Drag Coefficients for a Family of Blunt Bodies at Mach Number From 2.49 to 4.63." NASA TR R-274, October 1967.

23. Whitehead, Allen H., Hefner, Jerry N., and Rao, D. M. "Lee-Surface Vortex Effects Over Configurations in Hypersonic Flow." AIAA Paper No. 72-77, January 1972.

24. Kipp, H. W. and Masek, R. O. "Aerodynamic Heating Constraints on Space Shuttle Vehicle Design." ASME Paper 70-HI/SPI-45, June 1970.

25. Jones, Robert A. and Hunt, James L. "Use of Fusible Temperature Indicators for Obtaining Quantitative Aerodynamic Heat-Transfer Data." NASA-TR-R-230, February 1966.

26. Throckmorton, David A. "Heat Transfer Testing Procedures In Phase B Shuttle Studies with Emphasis on Phase-Change Data Improvement." NASA Tech. Memo, NASA TMX-2507, February 1972.

27. Thomas, Alfred C. and Perlbachs, Andrew "Application of Ground Test Data to Reentry Vehicle Design." AFFDL-TR-66-229, January 1967.

28. Nagel, A. L., Fitzsimmons, H. D., and Doyle, L. B. "Analysis of Hypersonic Pressure and Heat Transfer Tests on Delta Wings with Laminar and Turbulent Boundary Layers." NASA CR-535, August 1966.

29. Whitehead, A. H., Jr., and Dunavant, James C. "A Study of Pressure and Heat Transfer Over an 80° Sweep Slab Delta Wing in Hypersonic Flow." NASA TN D-2708, March 1965.

30. Eckert, E. R. G. "Engineering Relations for Friction and Heat Transfer to Surfaces in High Velocity Flow." Journal of the Aeronautical Sciences, Vol. 22, August 1955, pp. 585-587.

31. Marvin, J. G., Seegmiller, H. L., Lockman, W. K., Mateer, G. G., Pappas, C. C., and DeRose, C. E. "Surface Flow Patterns and Aerodynamic Heating on Space Shuttle Vehicles." AIAA Paper No. 71-594 presented at the AIAA 4th Fluid and Plasma Dynamics Conference, Palo Alto, California, June 21-23, 1971.

APPENDIXES

I. ILLUSTRATIONS
II. EVALUATION OF STYCAST THERMAL PROPERTIES
III. PHASE-CHANGE PAINT DATA REDUCTION ASSUMPTIONS
IV. FLOW-FIELD REGIMES ON THE WINDWARD SURFACE OF THE NORTH AMERICAN ROCKWELL ORBITER
V. BOUNDARY-LAYER CALCULATIONS

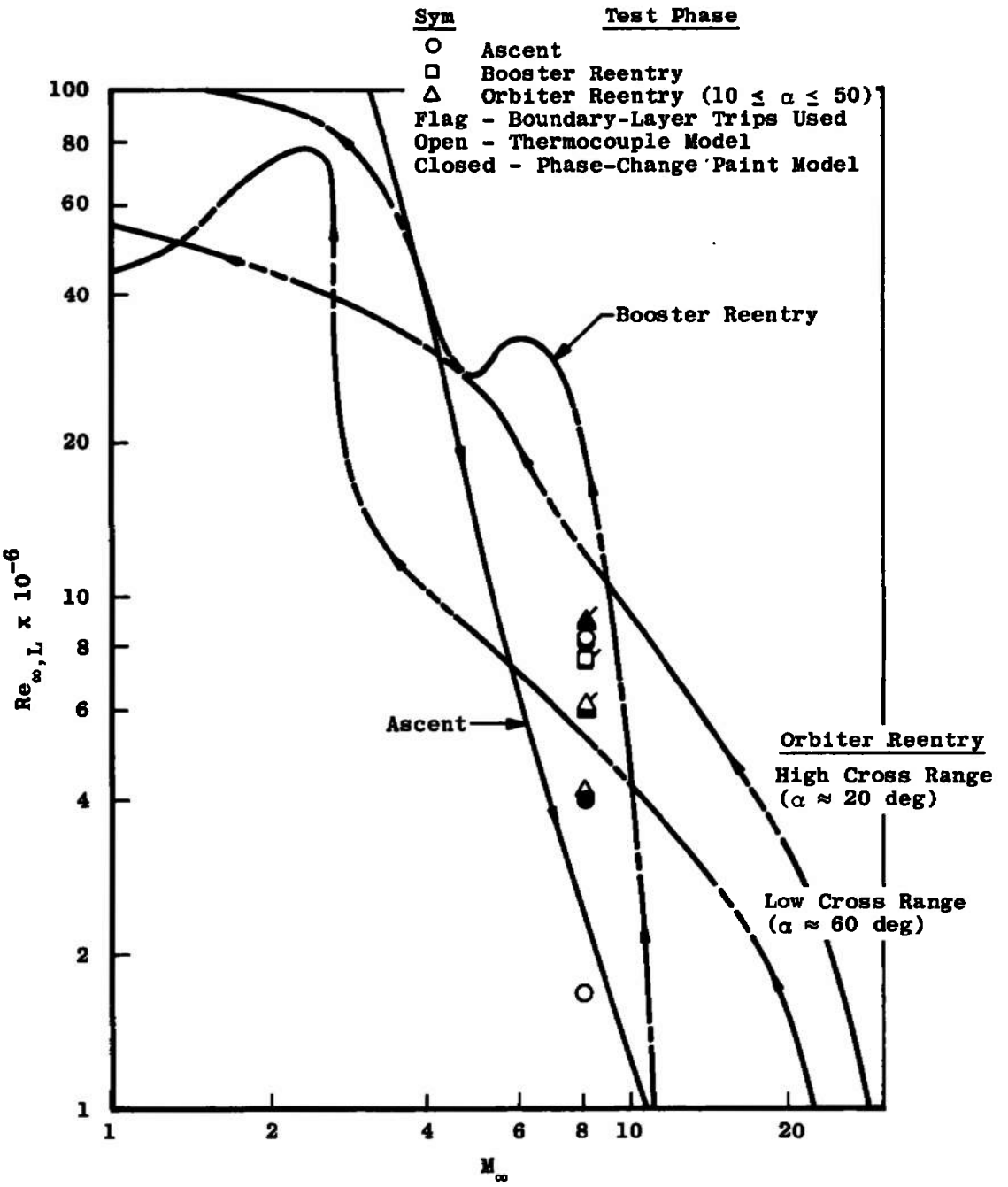

Fig. 1 Typical Space Shuttle Trajectories and VKF Simulated Conditions

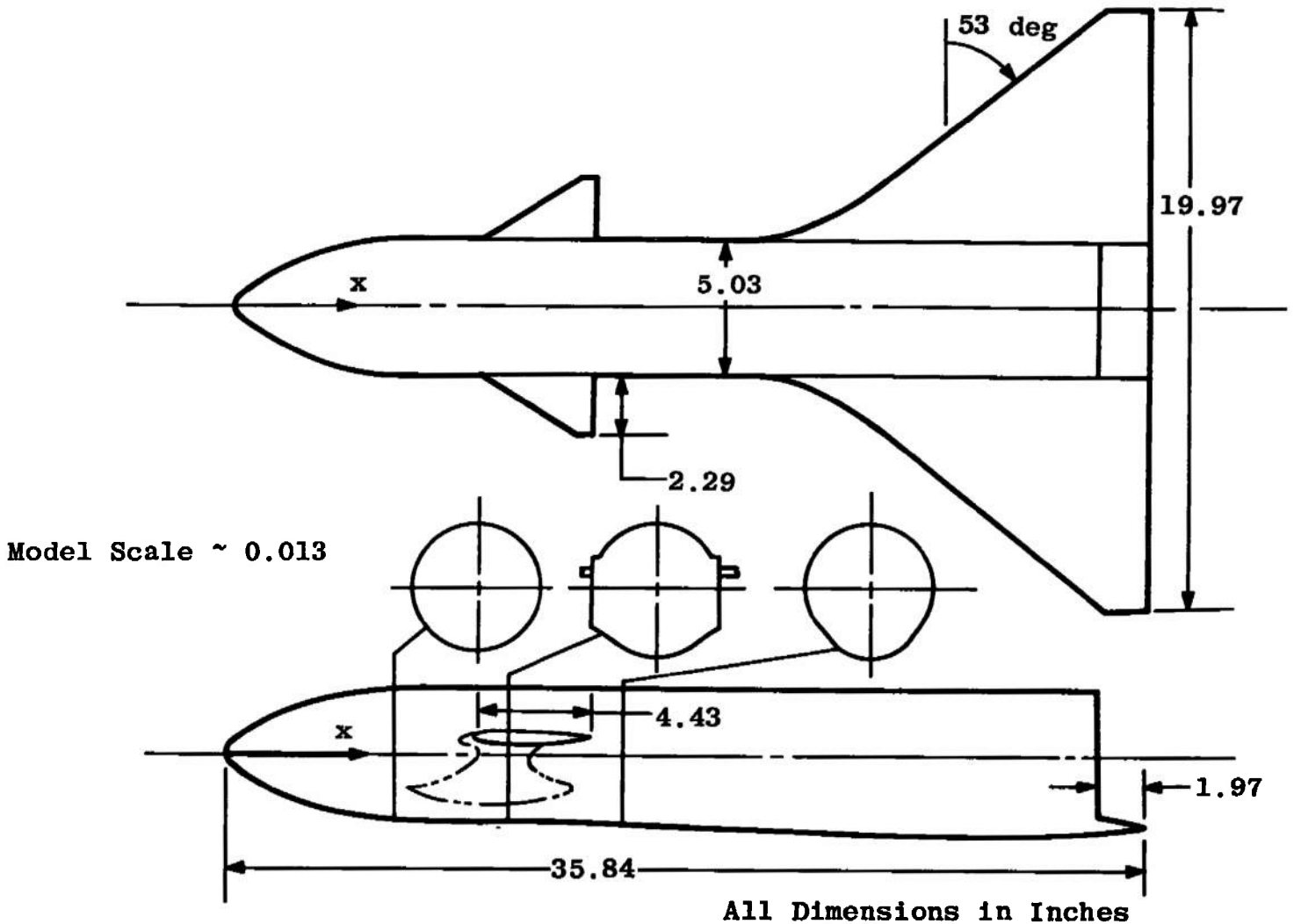

Fig. 2 Sketch of the General Dynamics Convair Booster Paint Model

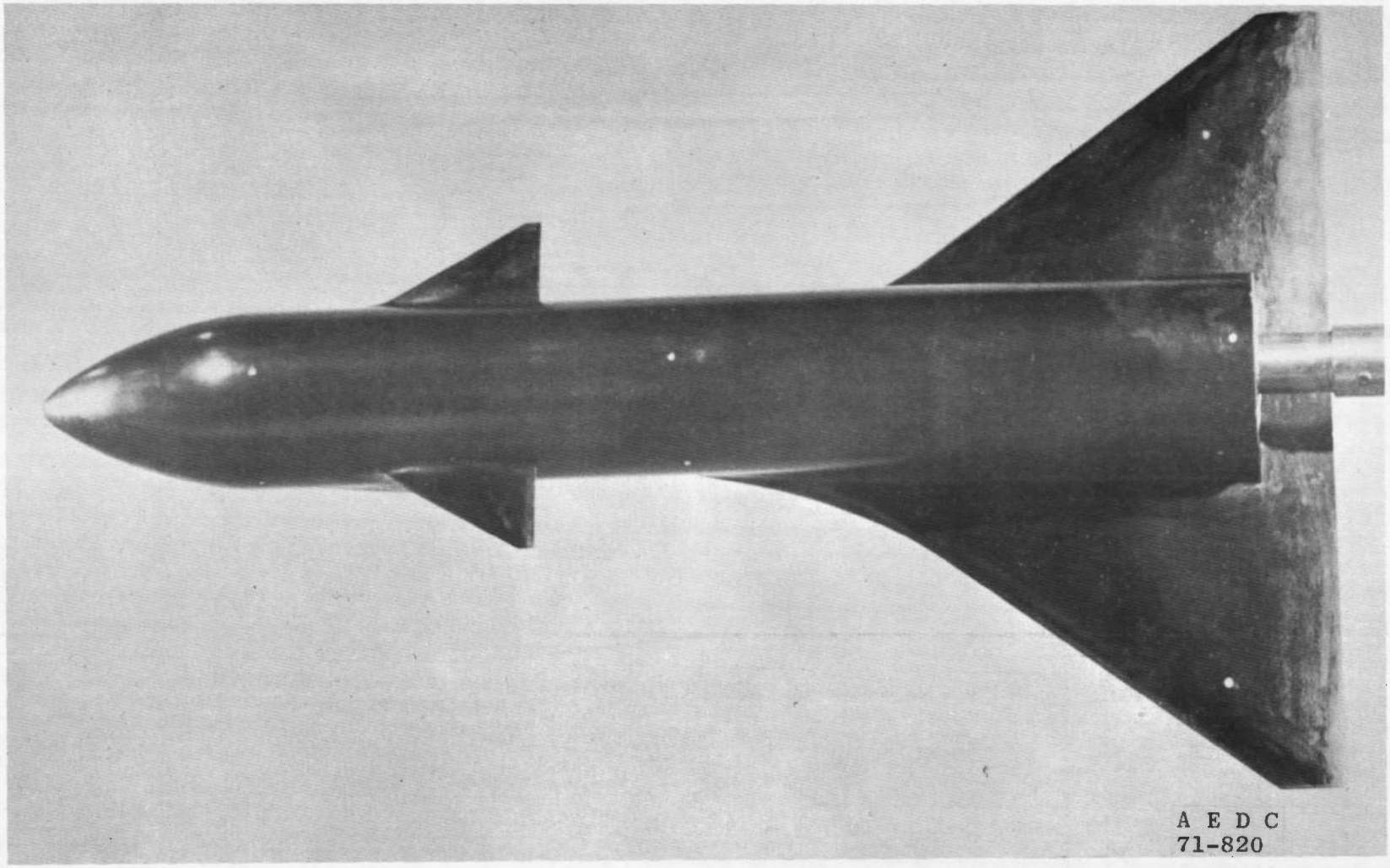

Fig. 3 Photograph of the General Dynamics Convair Booster Paint Model

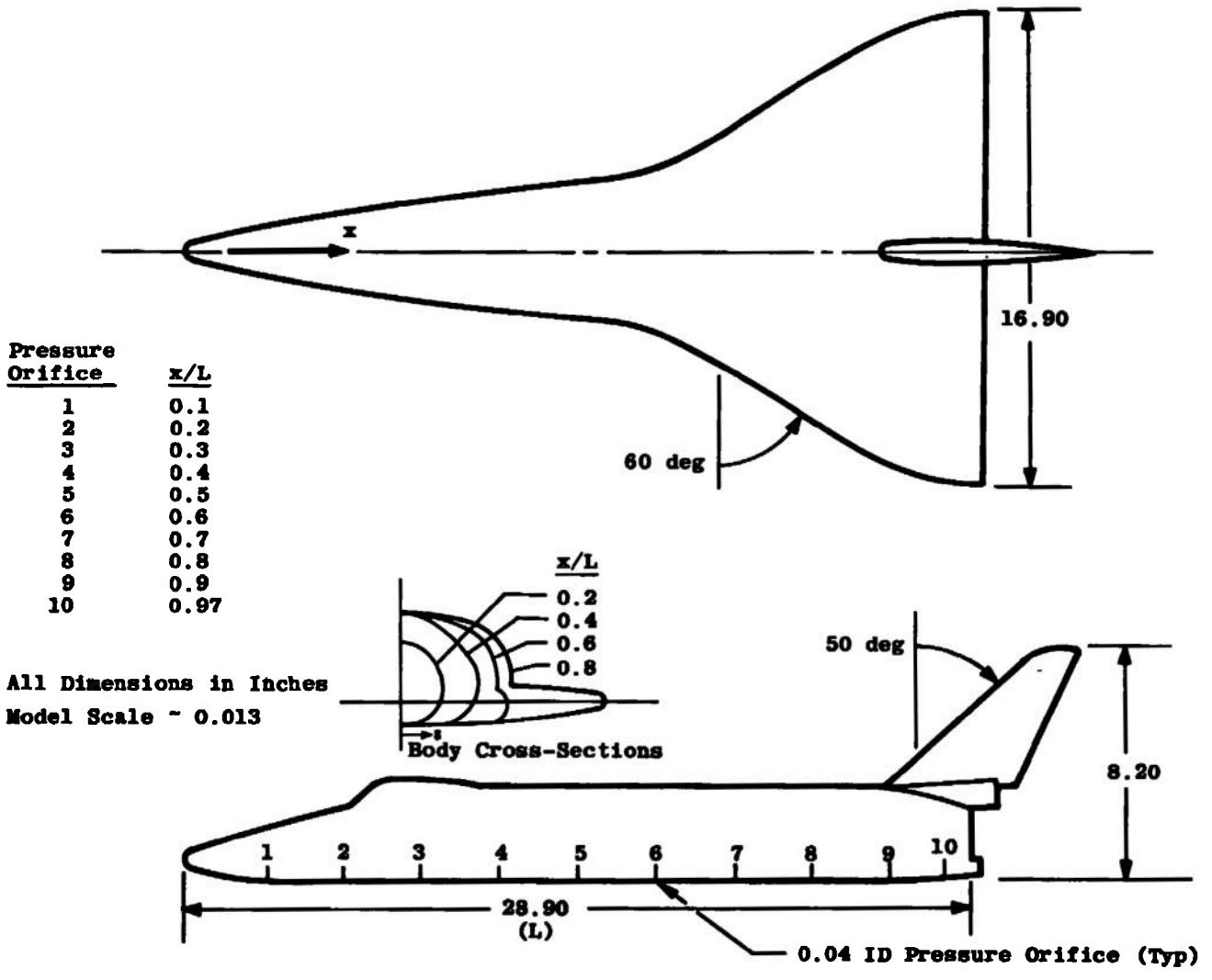

Fig. 4 Sketch of the North American Rockwell Orbiter Pressure and Paint Model

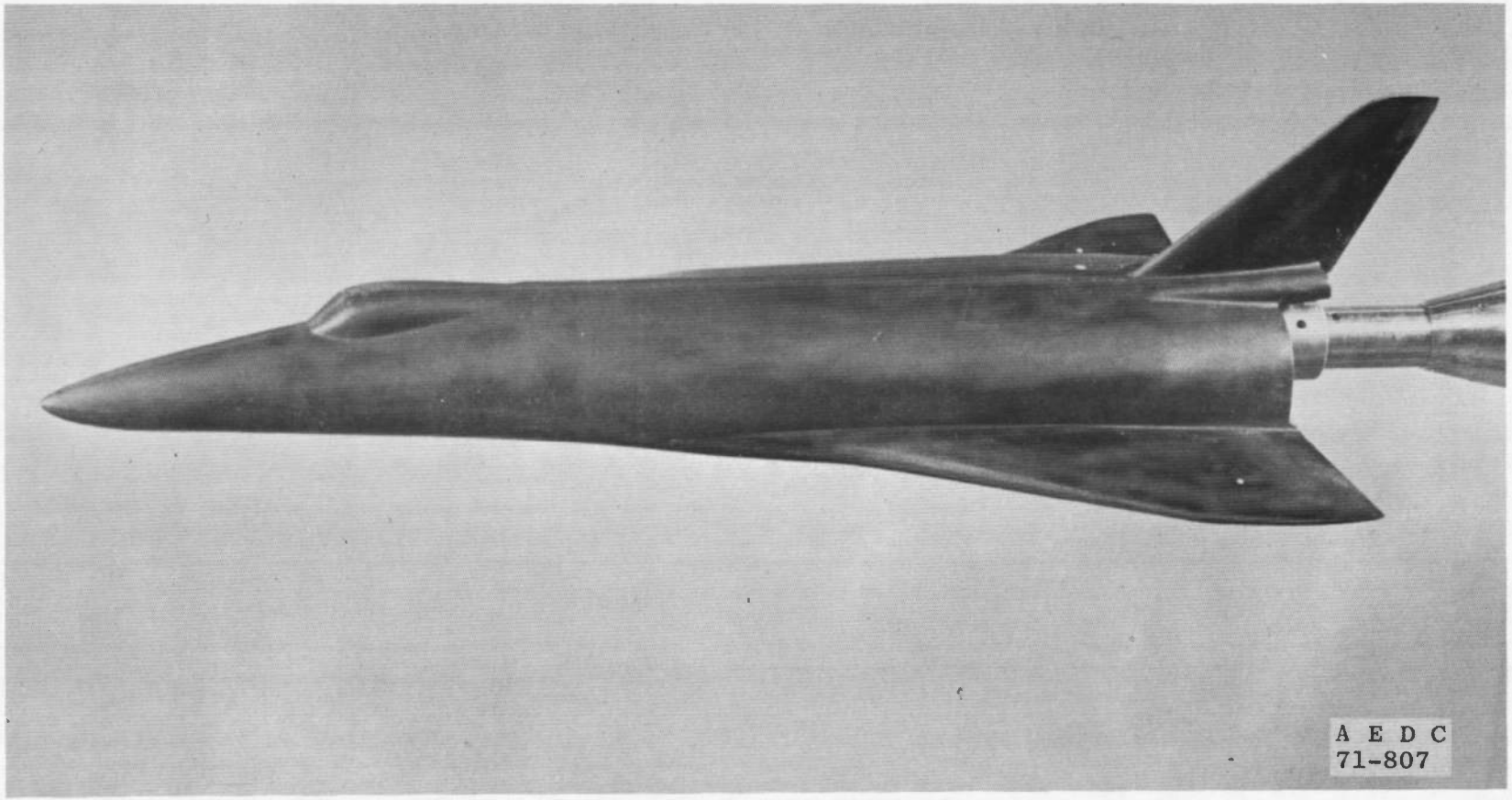

Fig. 5 Photograph of the North American Rockwell Orbiter Paint Model

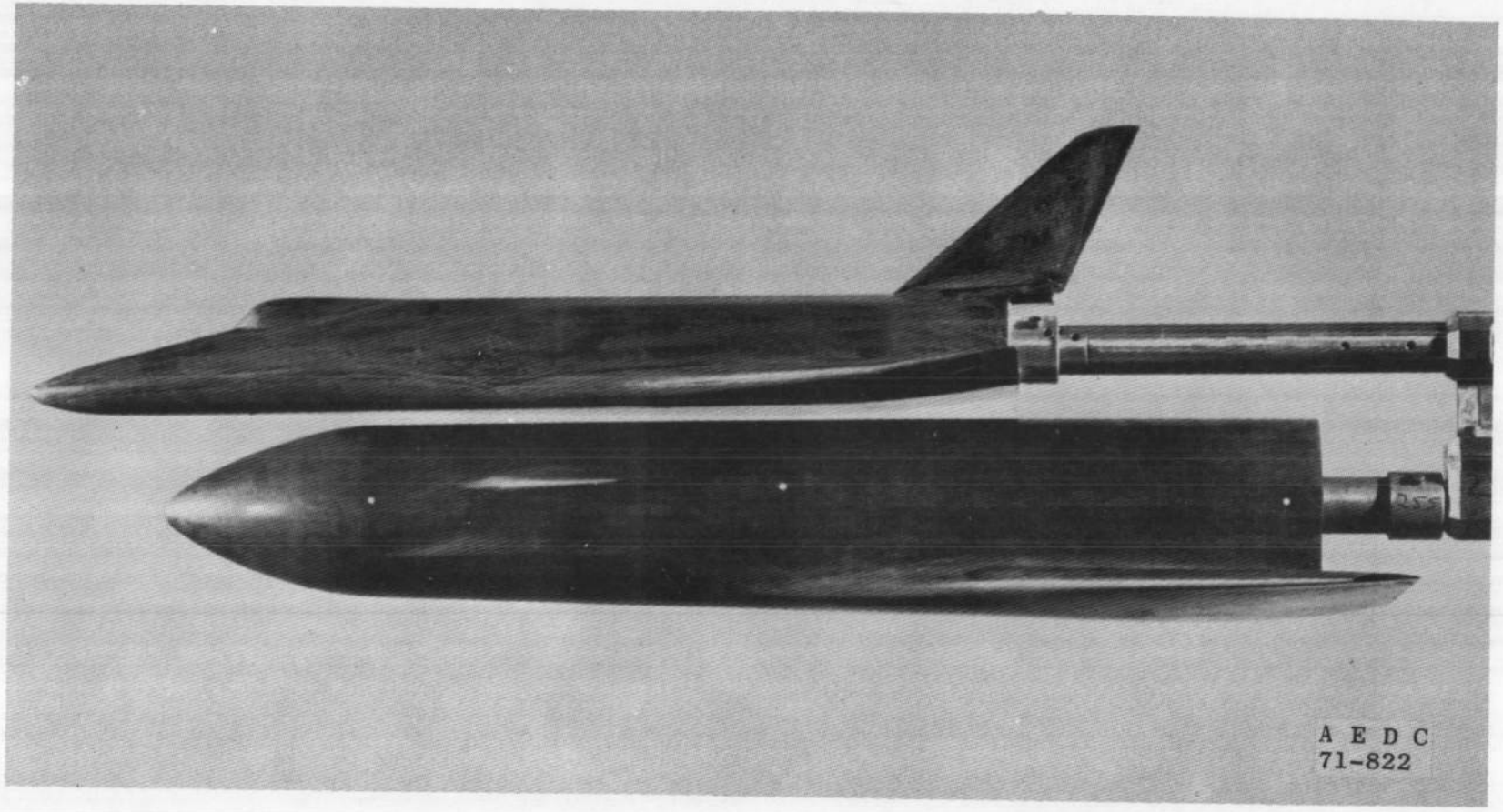

Fig. 6 Photograph of the Mated Orbiter and Booster Paint Models

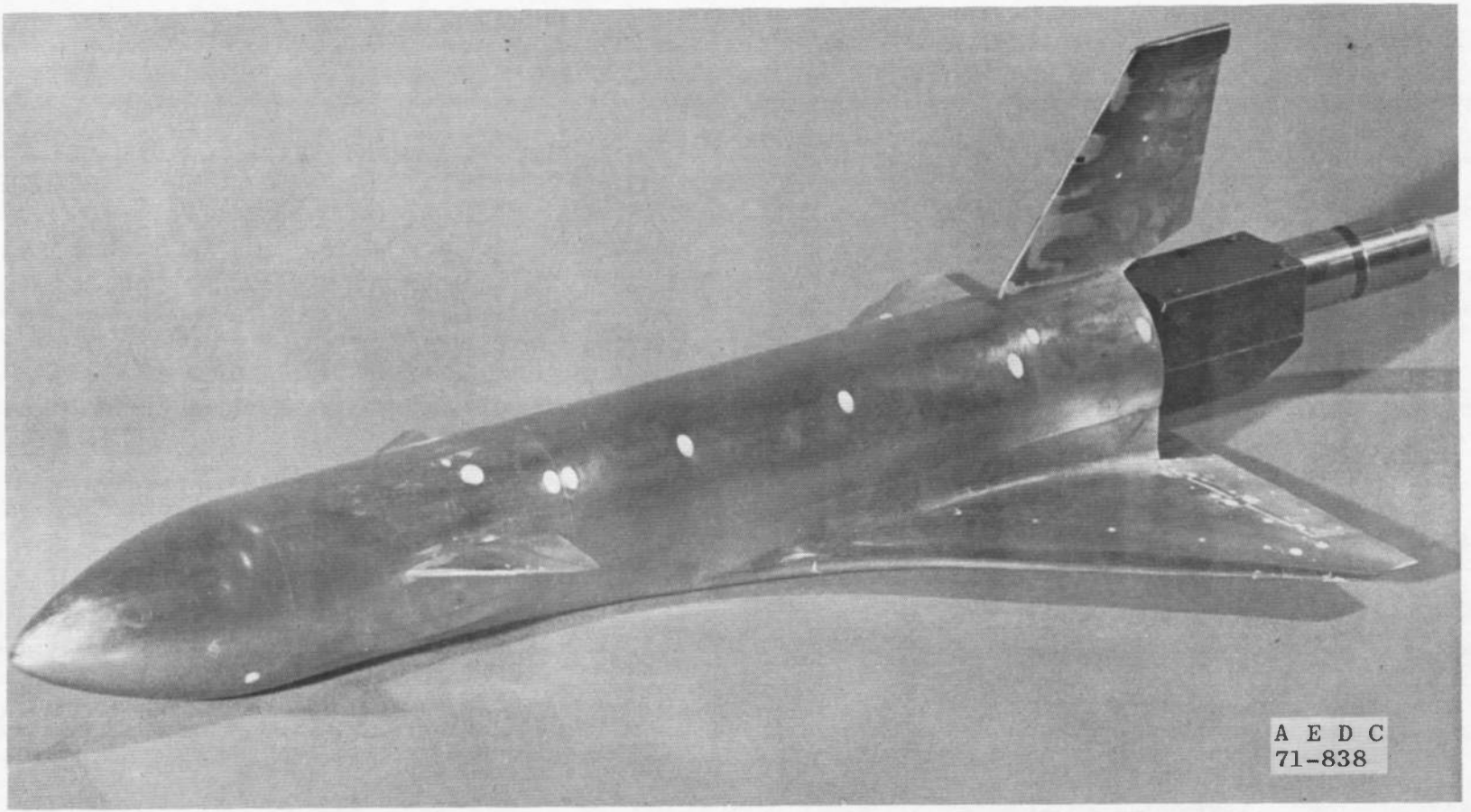

Fig. 7 Photograph of the General Dynamics Convair Booster Thermocouple Model

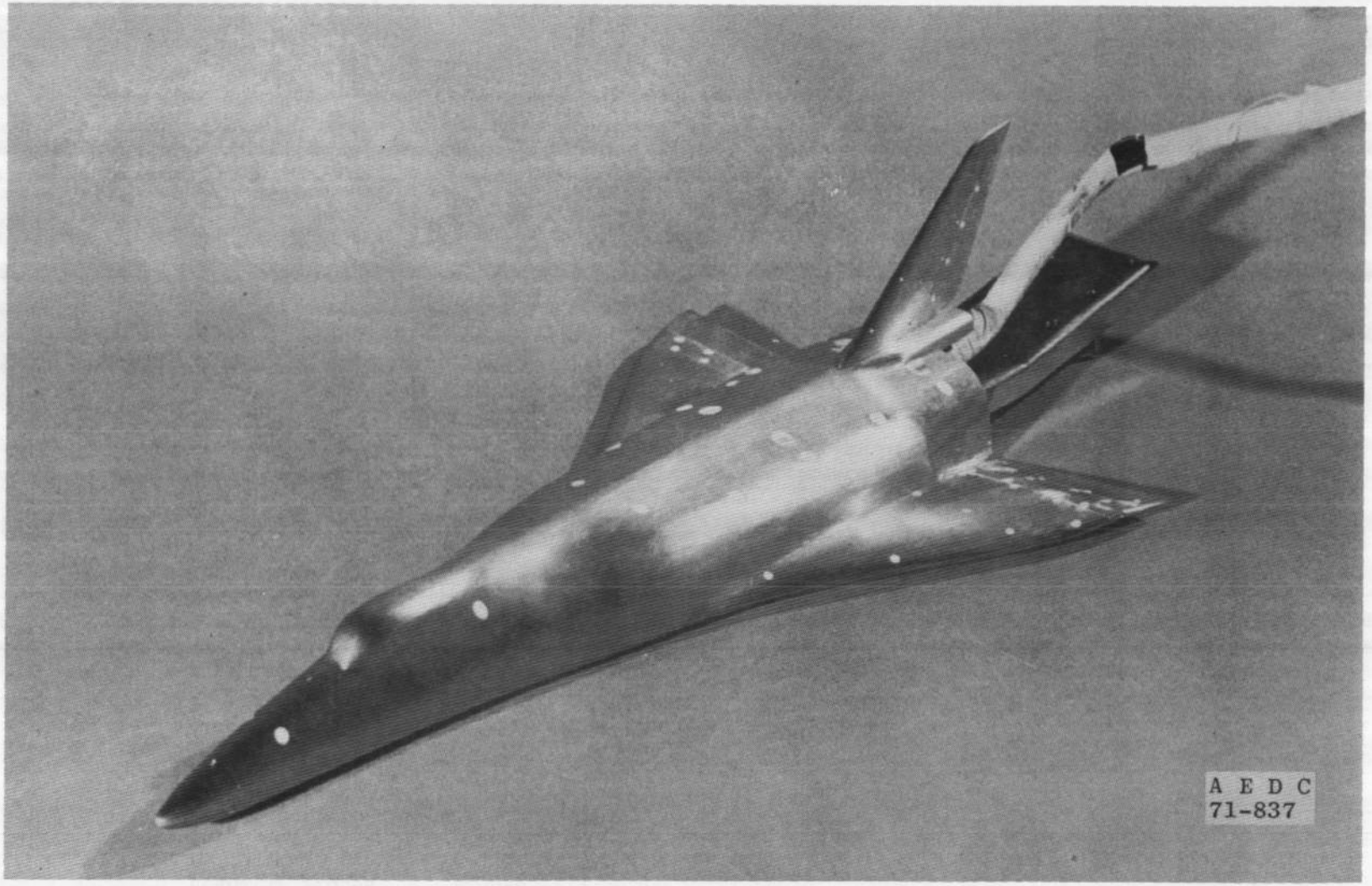

Fig. 8 Photograph of the North American Rockwell Orbiter Thermocouple Model

Probe Height, y, in.		
No.	Pressure Probes	Temperature Probes
1	0.014	0.051
2	0.066	0.131
3	0.112	0.202
4	0.163	0.303
5	0.216	0.402
6	0.258	0.599
7	0.313	
8	0.365	
9	0.415	
10	0.499	
11	0.606	
12	0.702	
13	0.802	
14	0.892	
15	0.981	

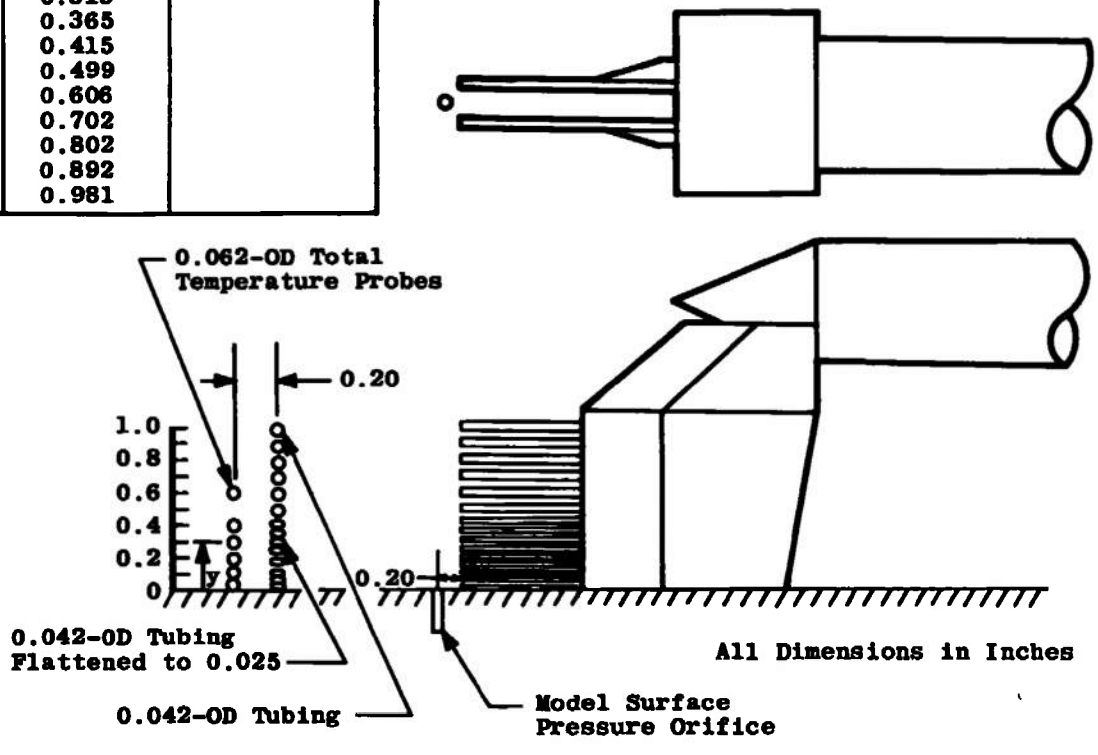

Fig. 9 Probe Rakes and Support

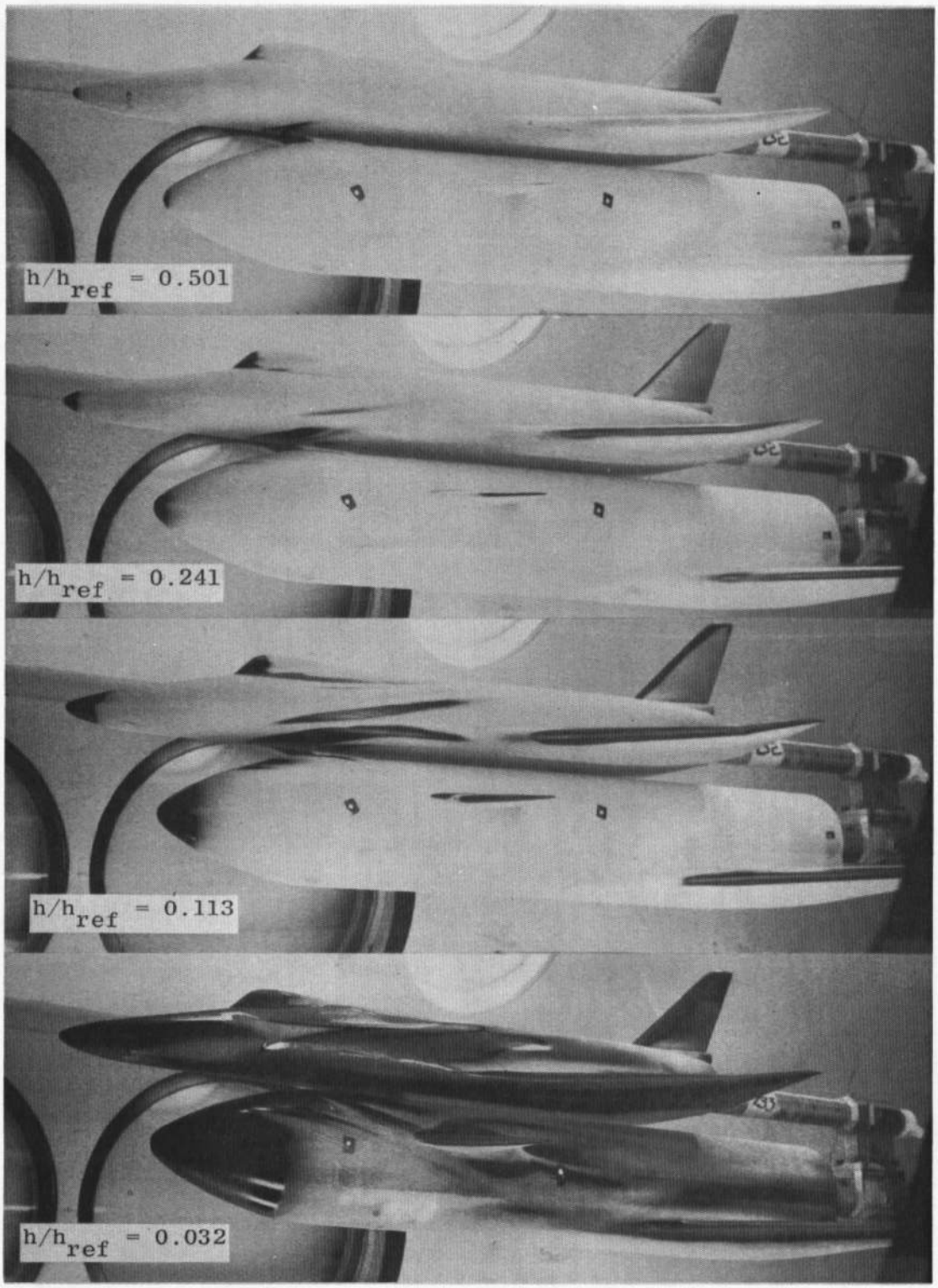

Fig. 10 Mated Configuration at α = 0, Re_∞ = 1.3 x 10^6 ft^{-1}

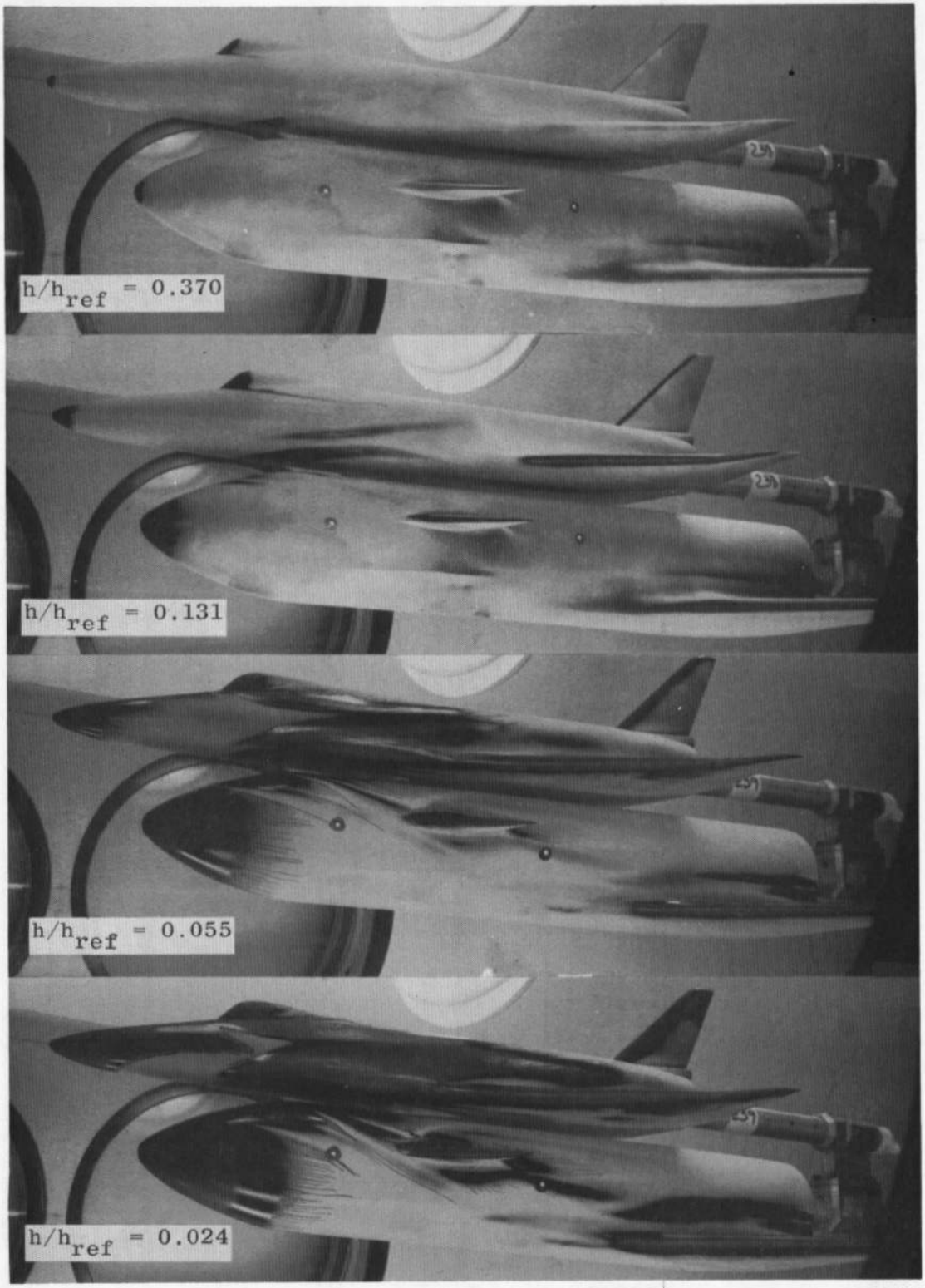

Fig. 11 Mated Configuration at α = 0, Re_∞ = 2.5 x 10^6 ft^{-1}

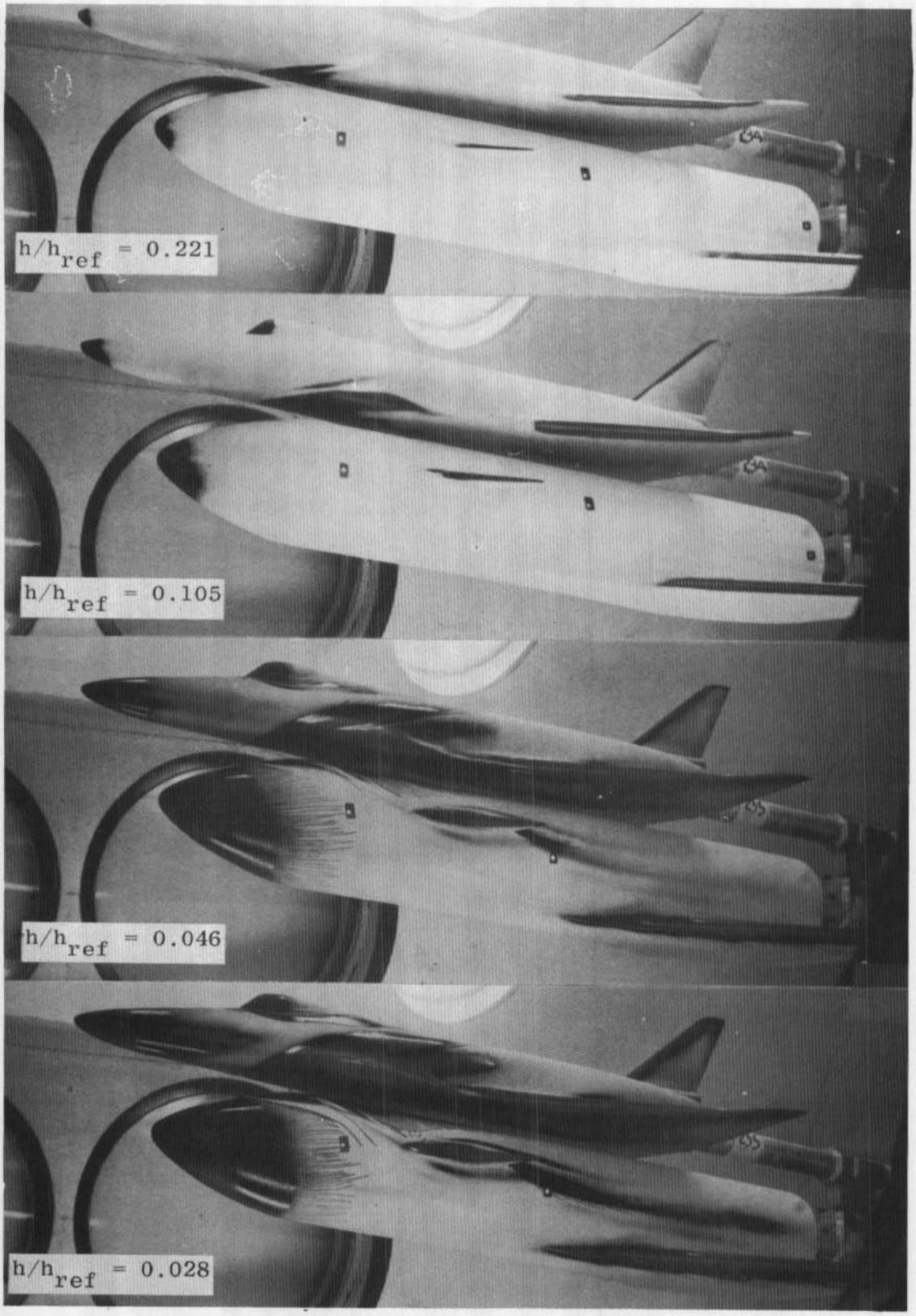

Fig. 12 Mated Configuration at α = 5, Re_∞ = 2.5 x 10^6 ft^{-1}

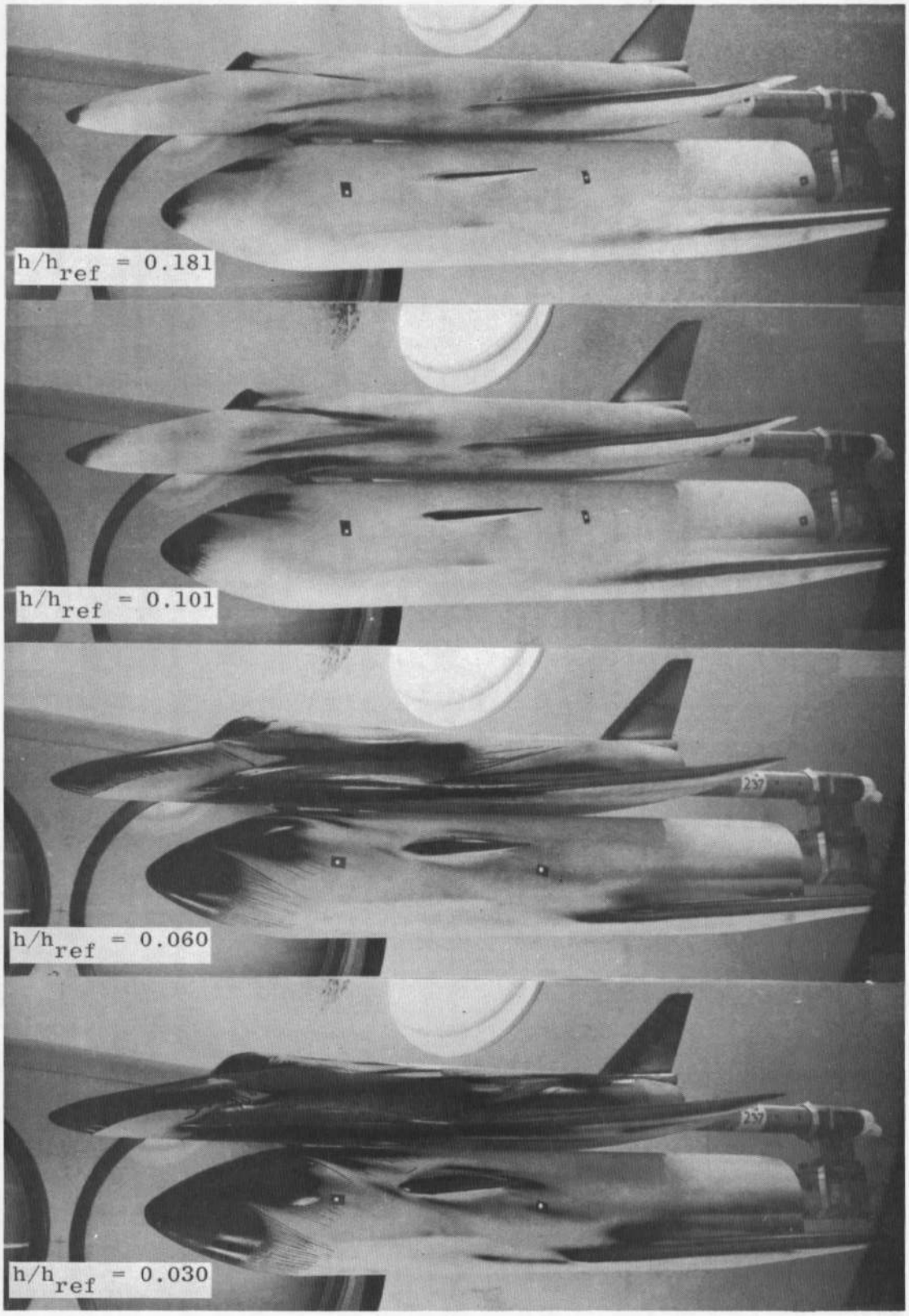

Fig. 13 Mated Configuration at α = -5, Re_∞ = 2.5 x 10^6 ft^{-1}

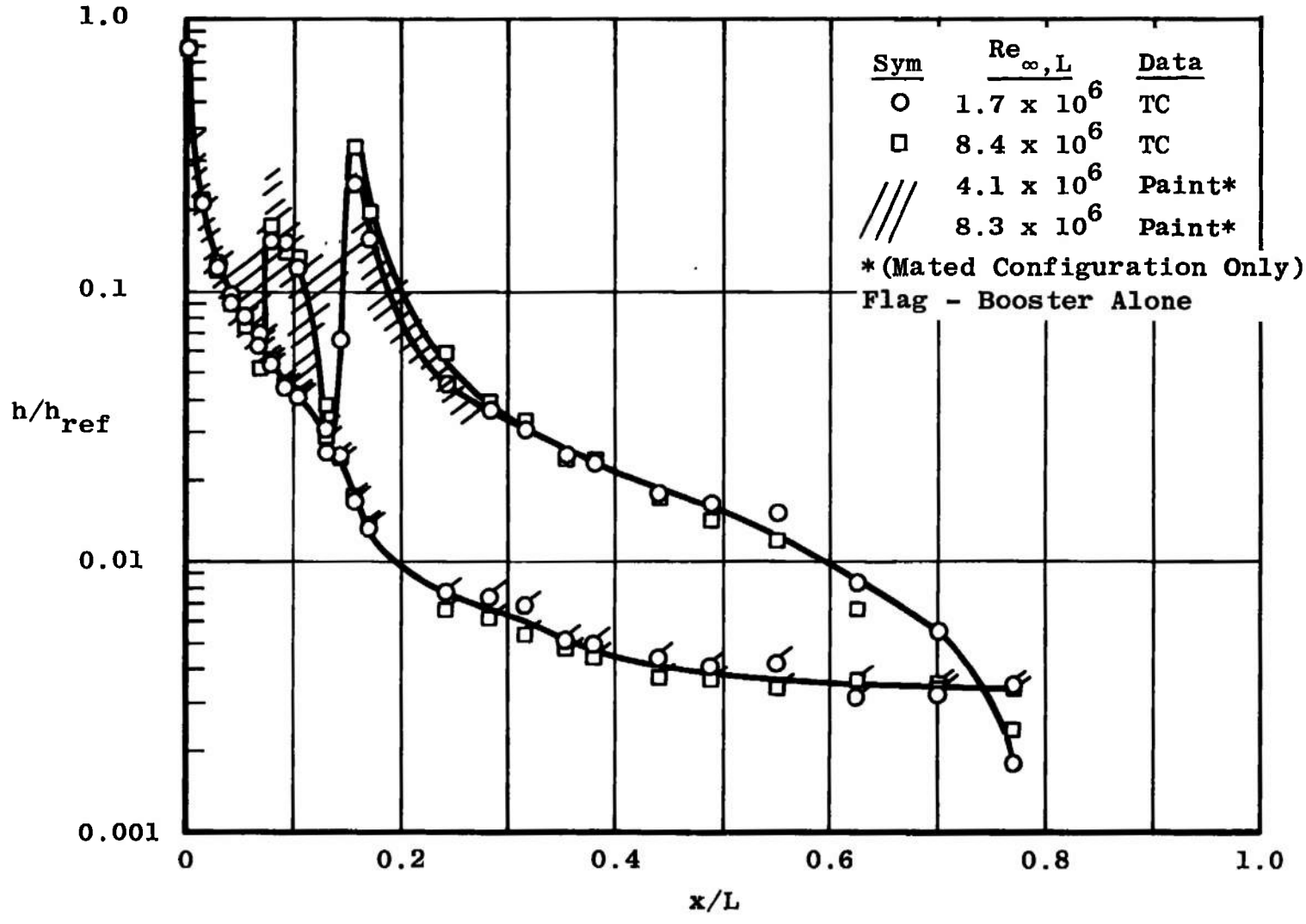

Fig. 14 Upper Centerline Heat-Transfer Distributions on the Booster in the Mated Configuration, $\alpha = 0$

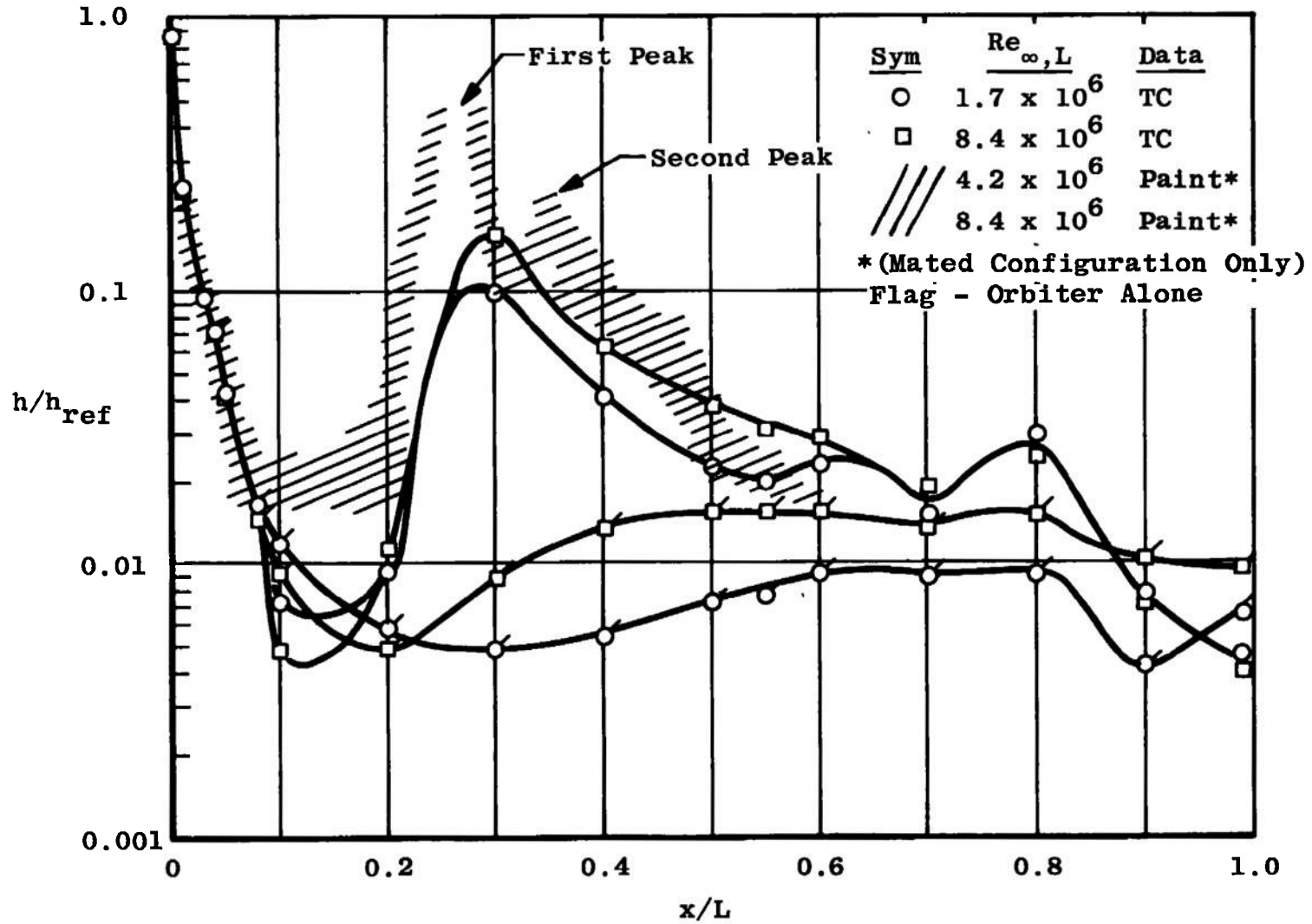

Fig. 15 Lower Centerline Heat-Transfer Distribution of Orbiter in the Mated Configuration, $\alpha = 0$

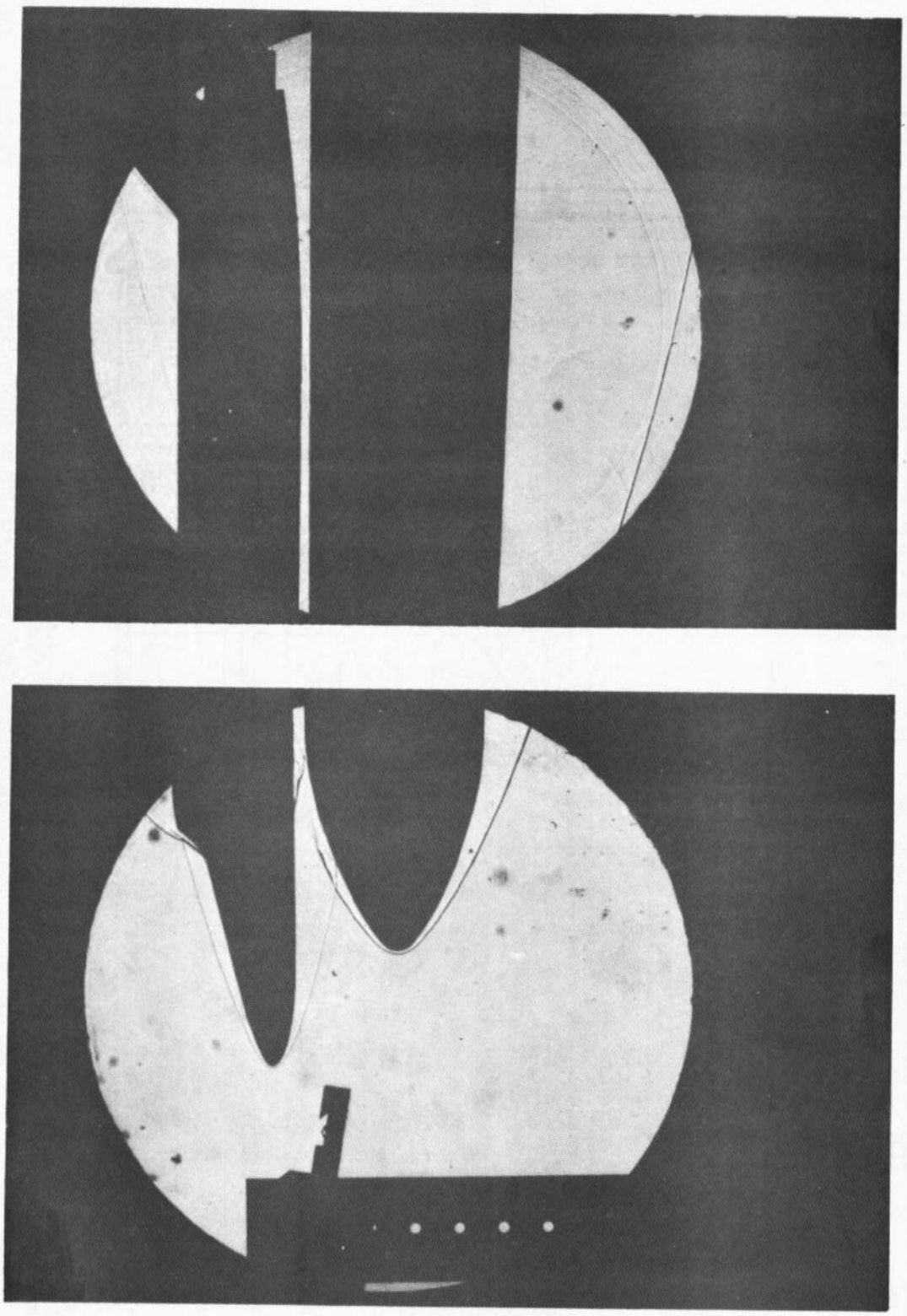

Fig. 16 Shadowgraph Photograph of the Mated Configuration, $\alpha = 0$, $Re_\infty = 2.5 \times 10^6$ ft^{-1}

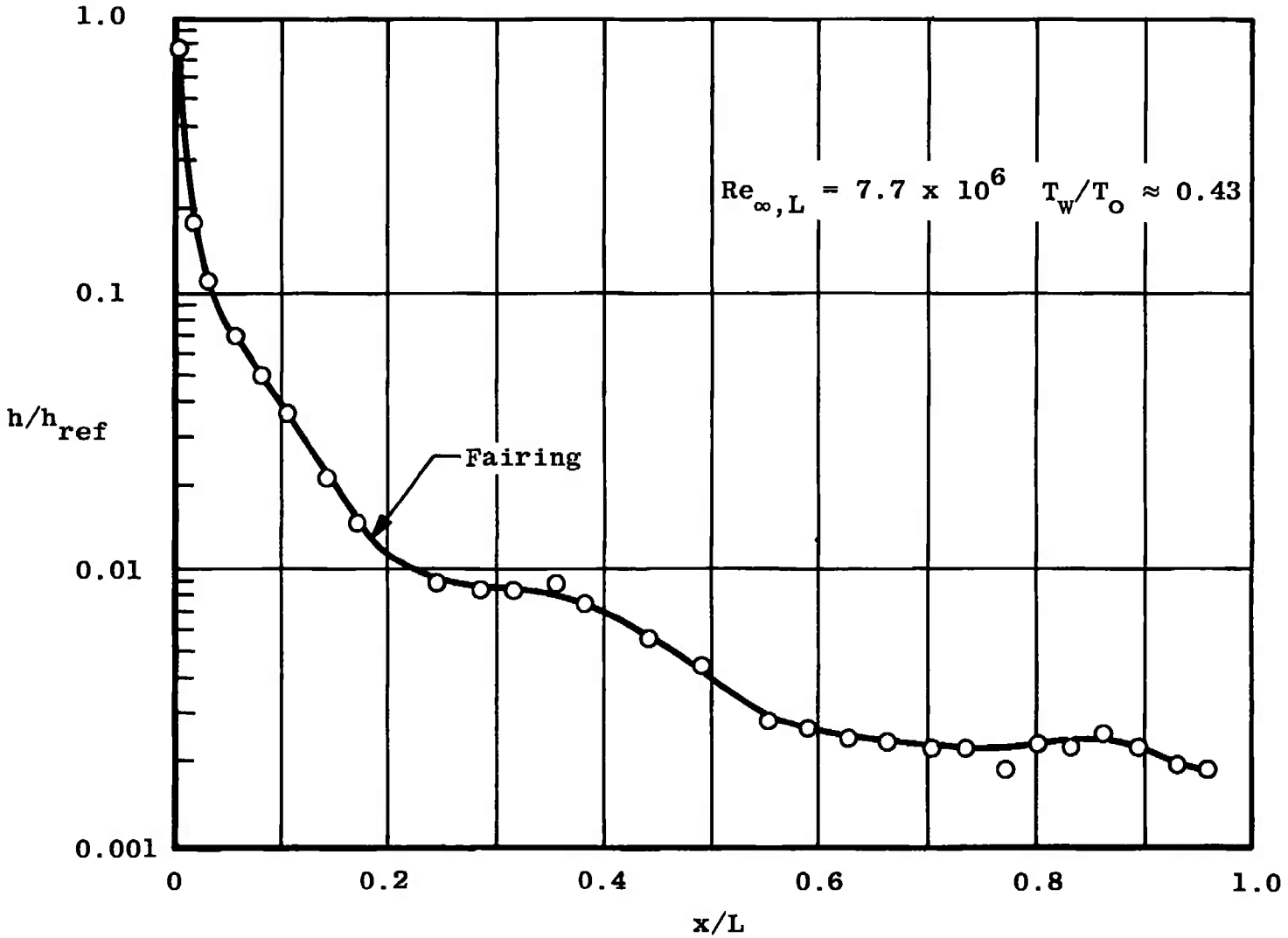

a. $\alpha = 0$

Fig. 17 Comparison of Experimental and Theoretical Booster Windward Centerline Heat-Transfer Distributions

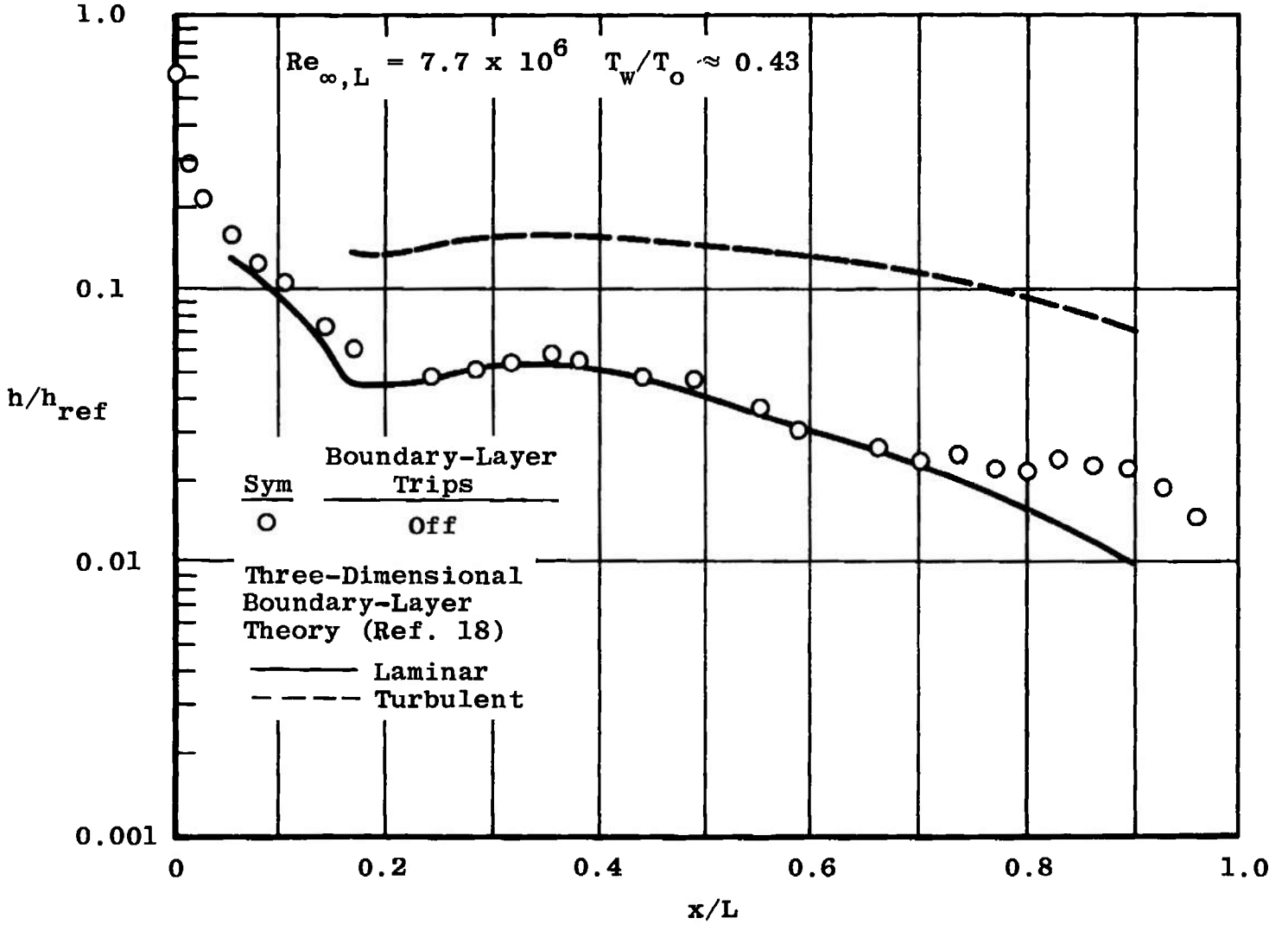

b. α = 20 deg

Fig. 17 Continued

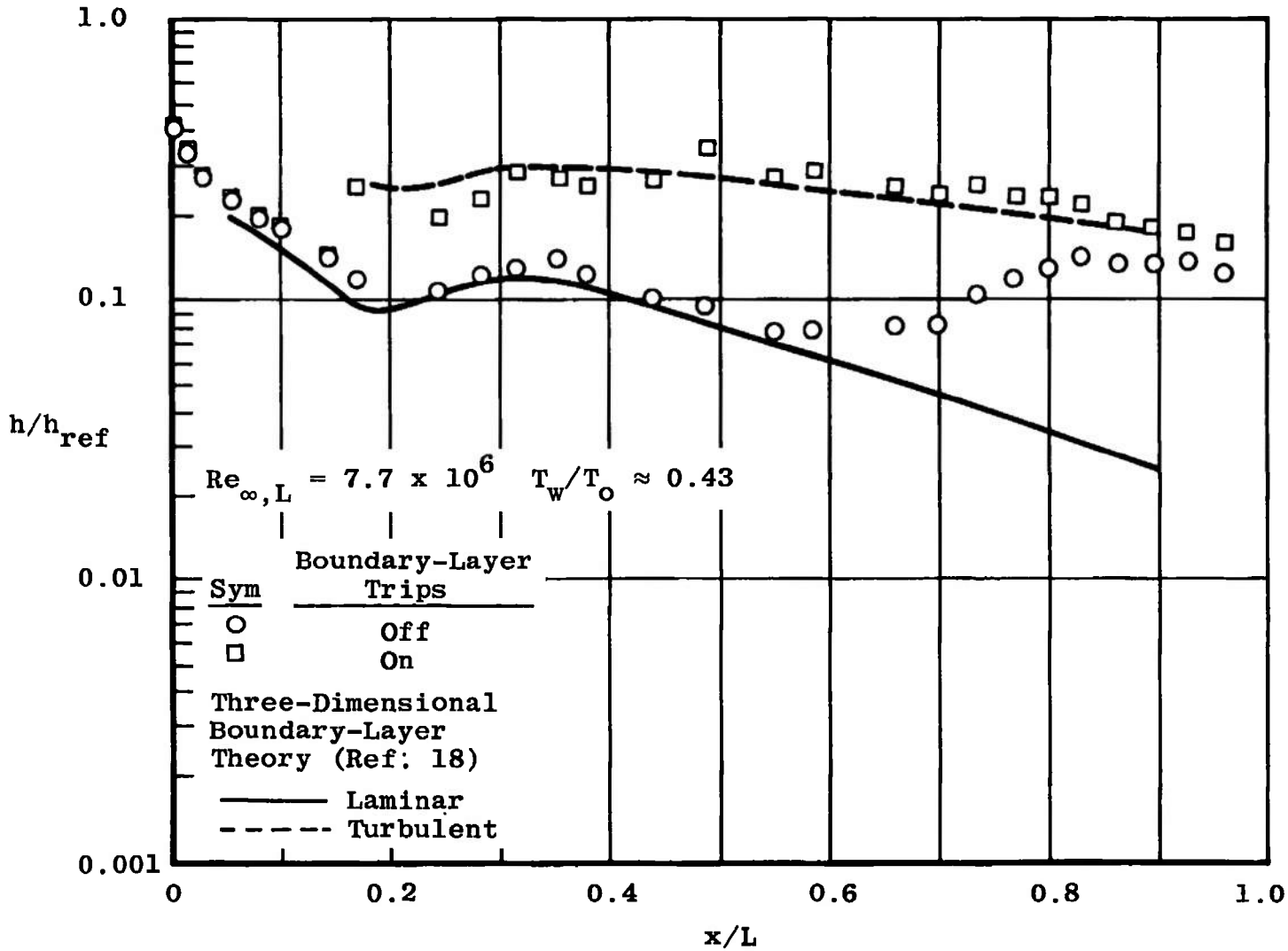

c. α = 40 deg

Fig. 17 Continued

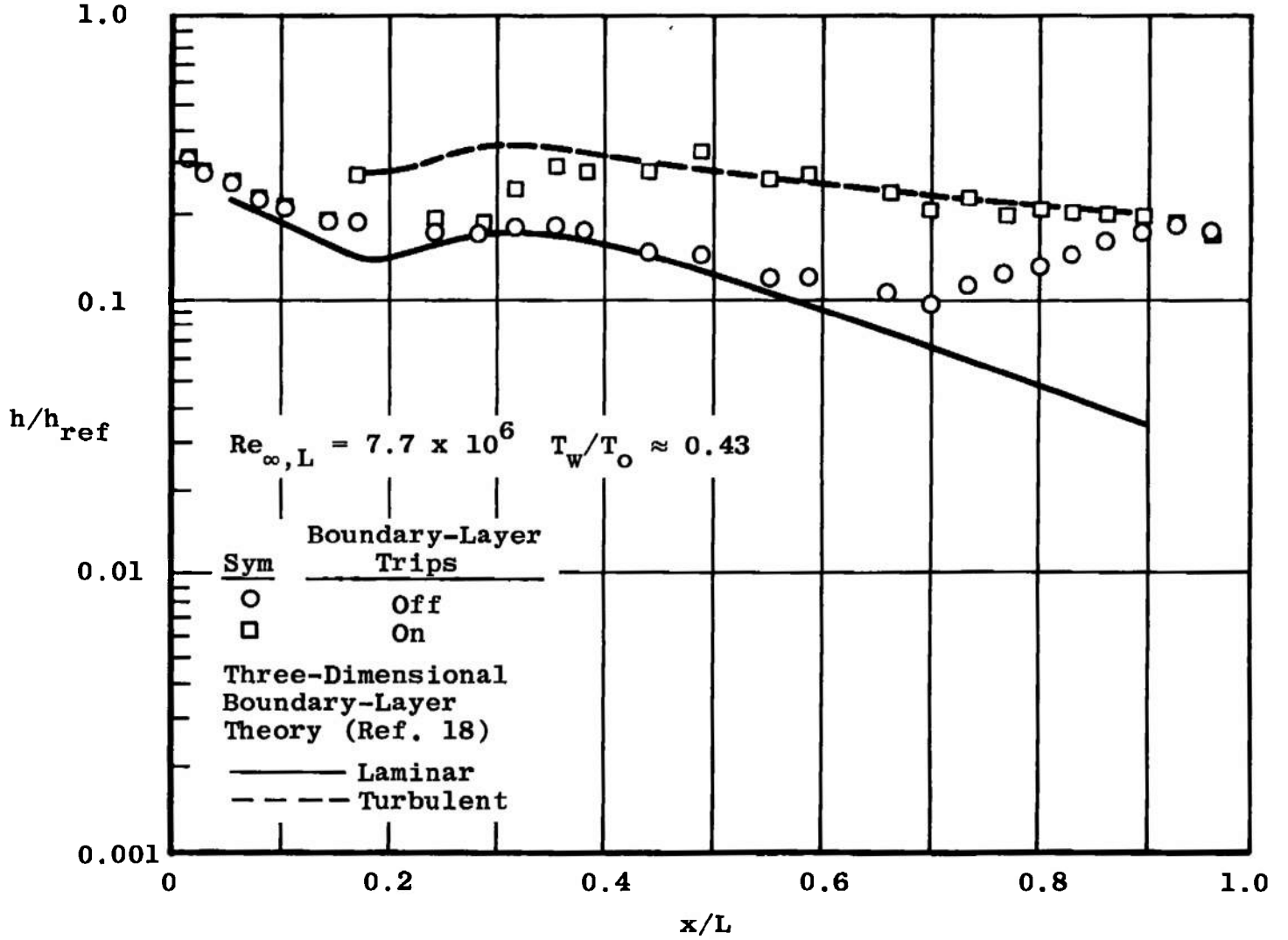

d. α = 60 deg

Fig. 17 Concluded

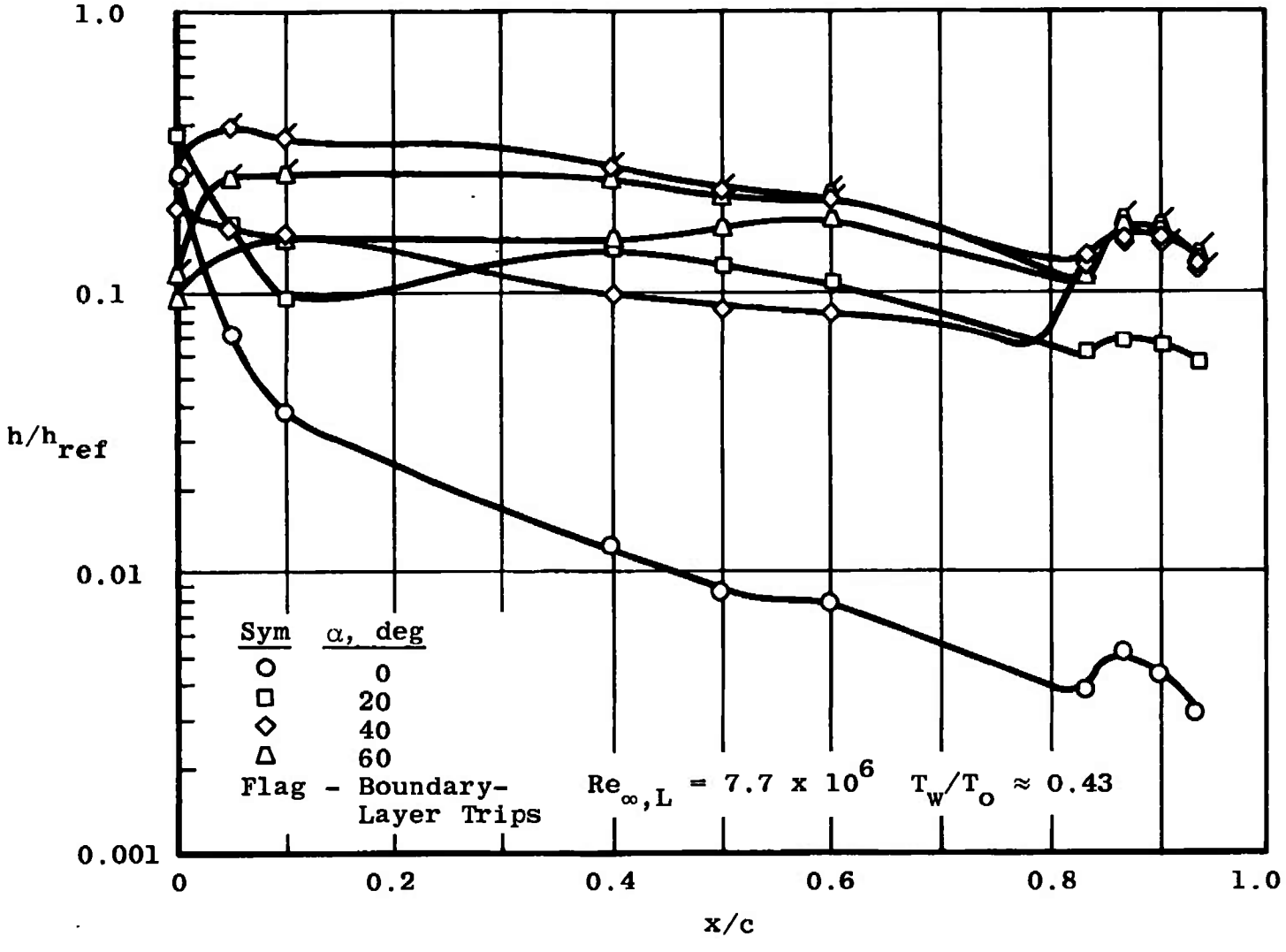

Fig. 18 Booster Windward Wing Heat-Transfer Distributions at Quarter Span

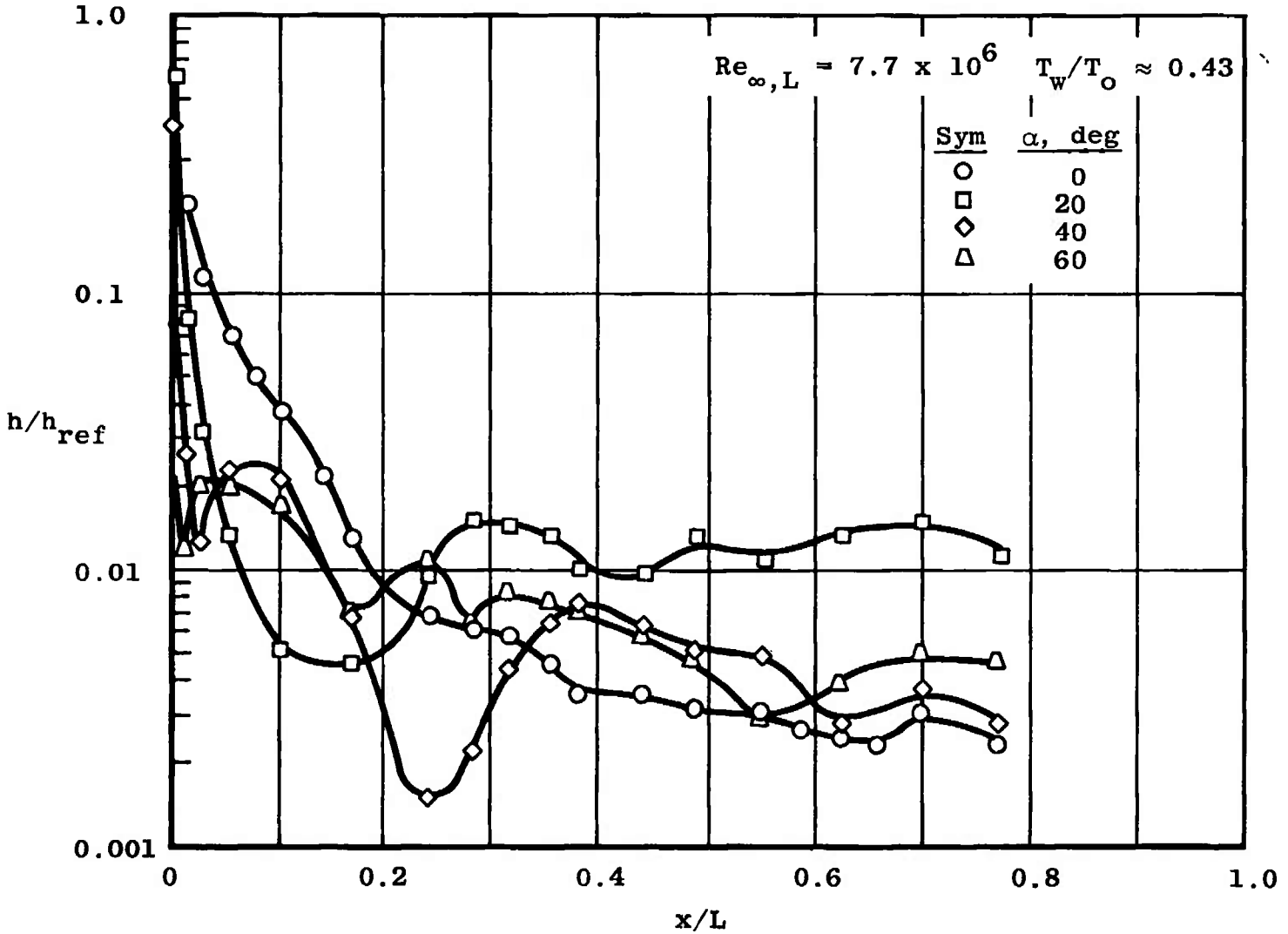

Fig. 19 Booster Leeward Centerline Heat-Transfer Distributions

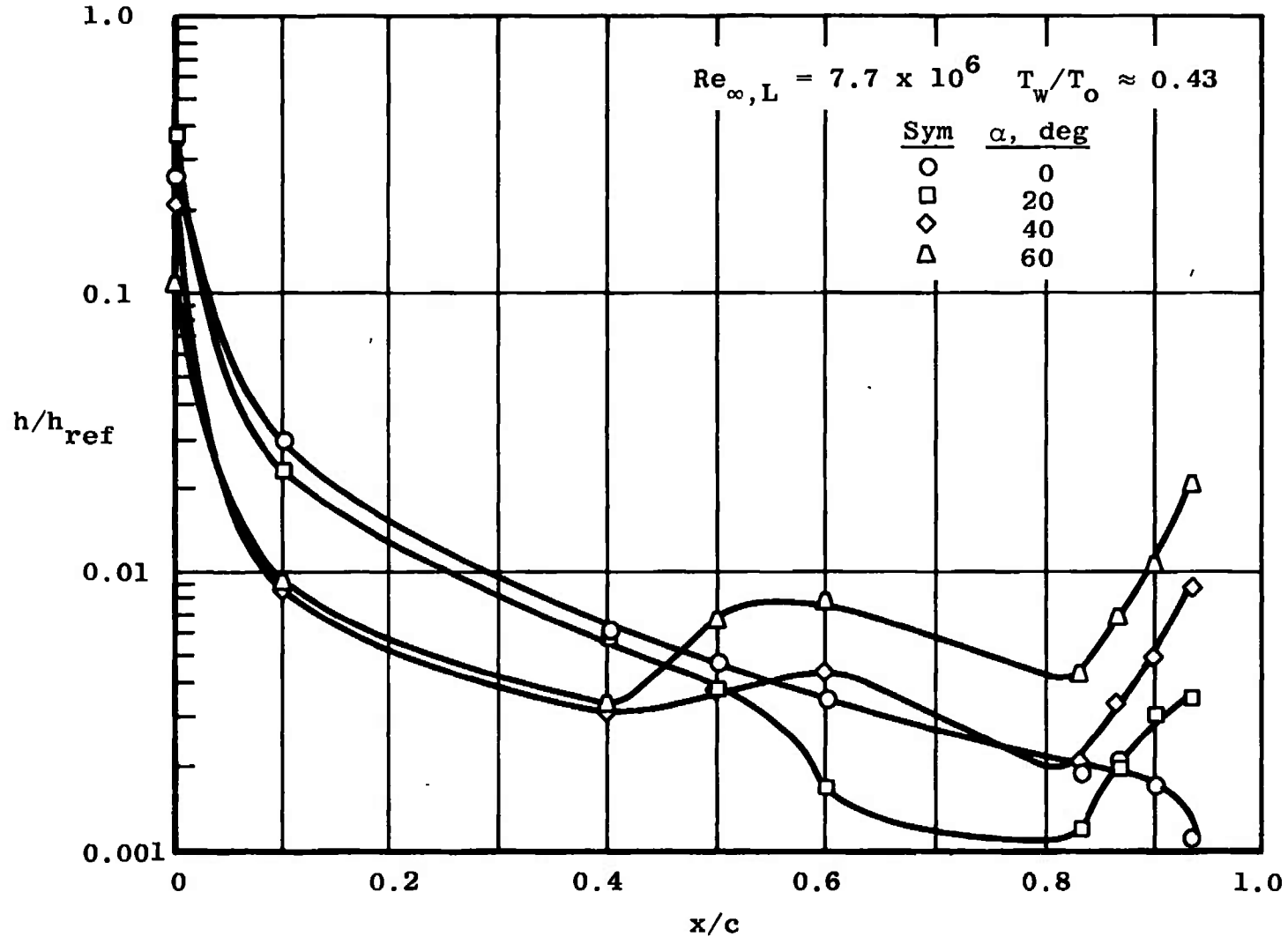

Fig. 20 Booster Leeward Wing Heat-Transfer Distributions at Quarter Span

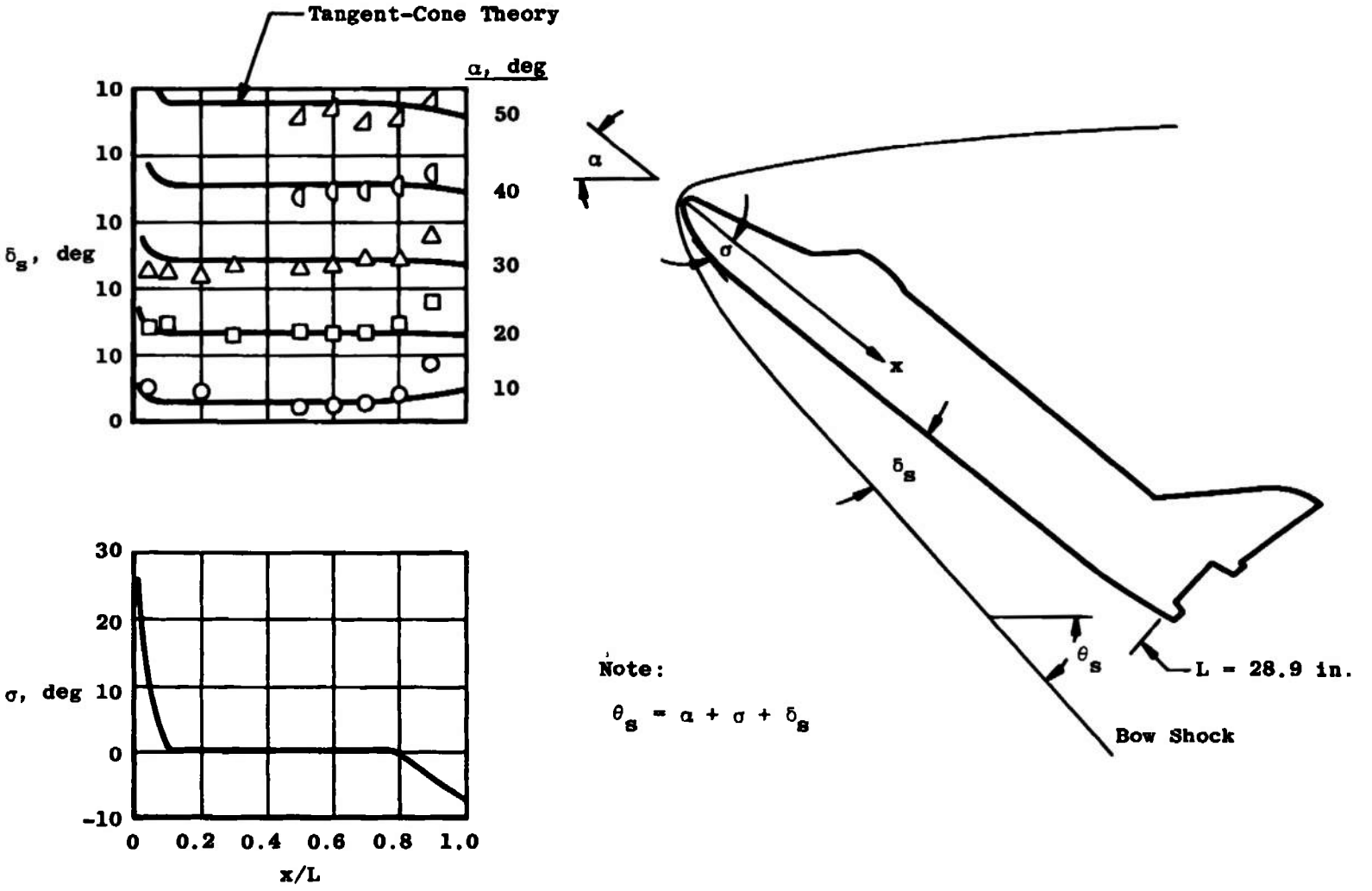

Fig. 21 Comparison of Experimental and Theoretical Orbiter Shock Angles

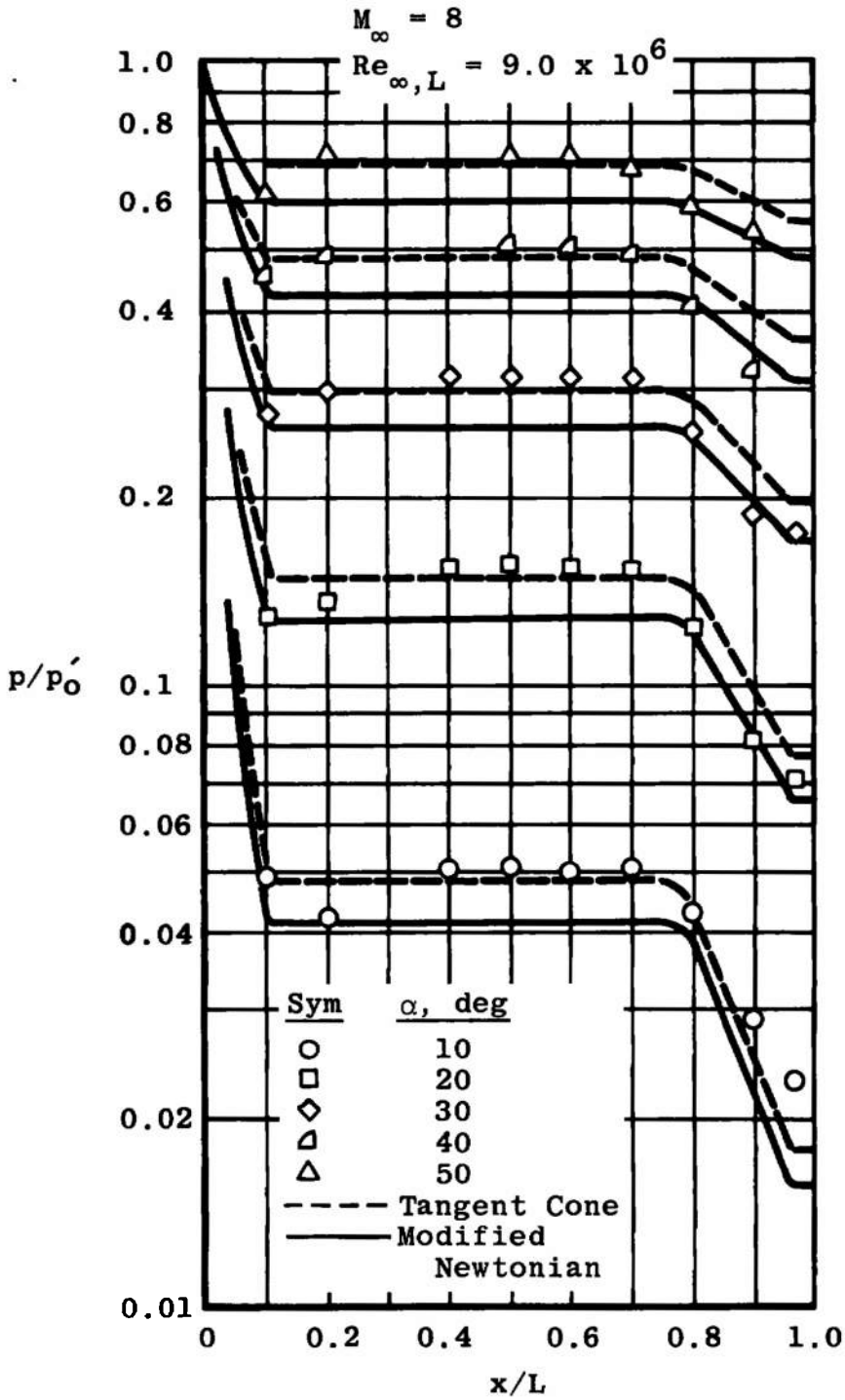

Fig. 22 Orbiter Windward Centerline Pressure Distributions

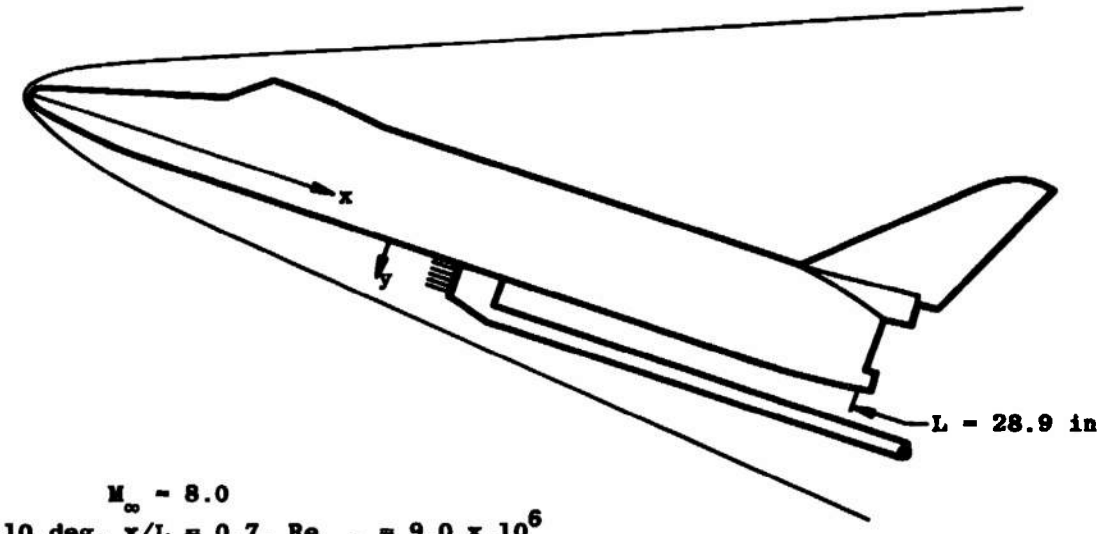

$M_\infty = 8.0$
$\alpha = 10$ deg, $x/L = 0.7$, $Re_{\infty,L} = 9.0 \times 10^6$

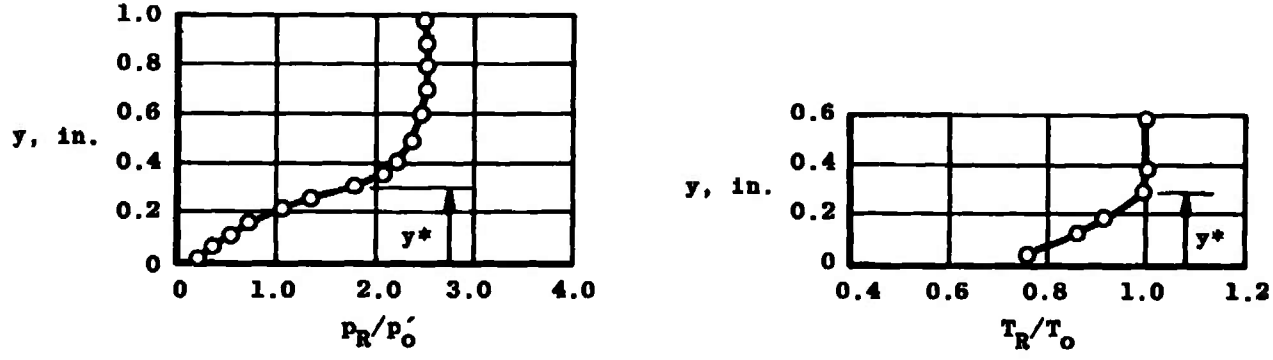

Fig. 23 Typical Pitot Pressure and Total-Temperature Profiles

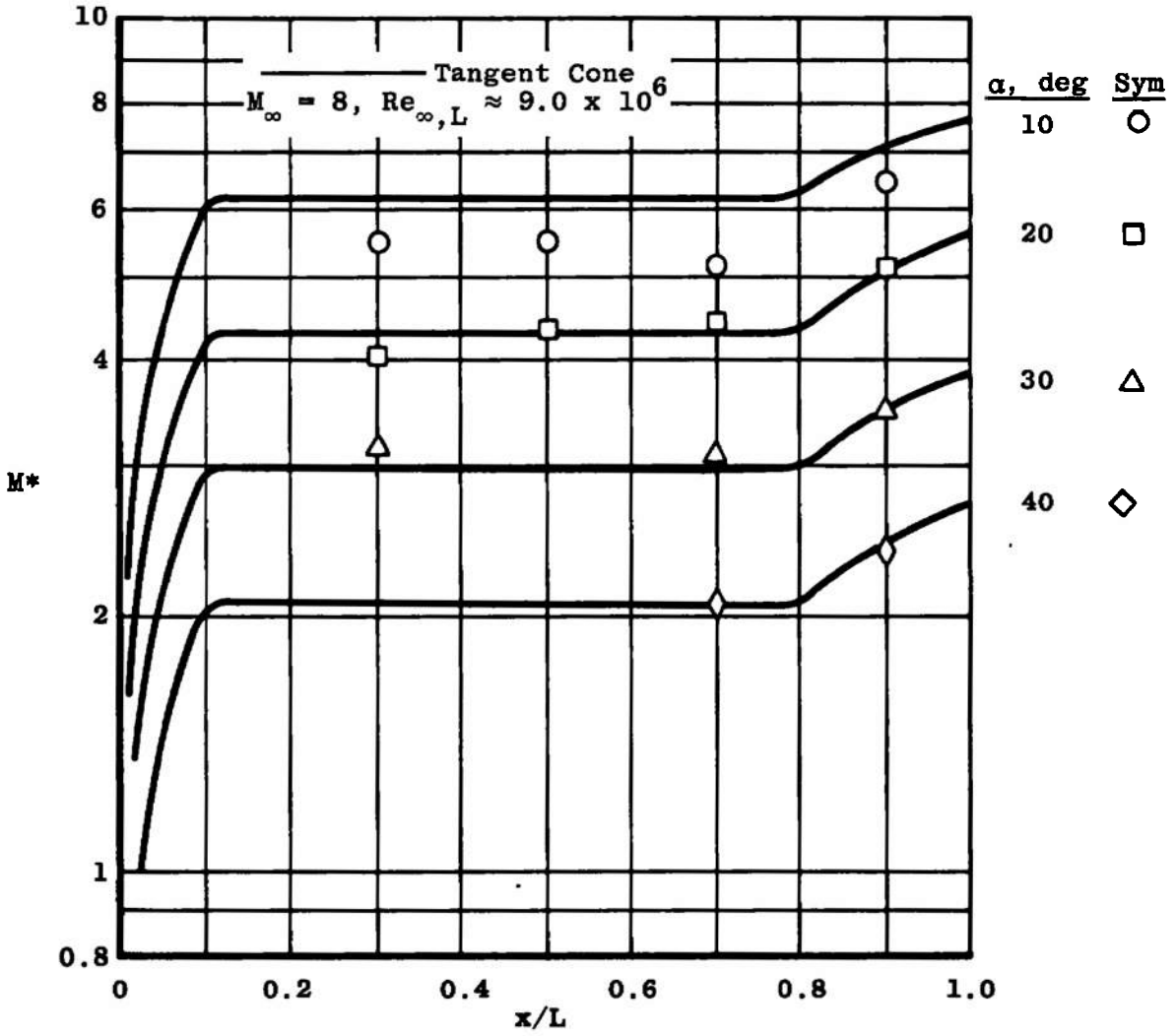

Fig. 24 Orbiter Windward Centerline Inviscid Mach Number Distributions

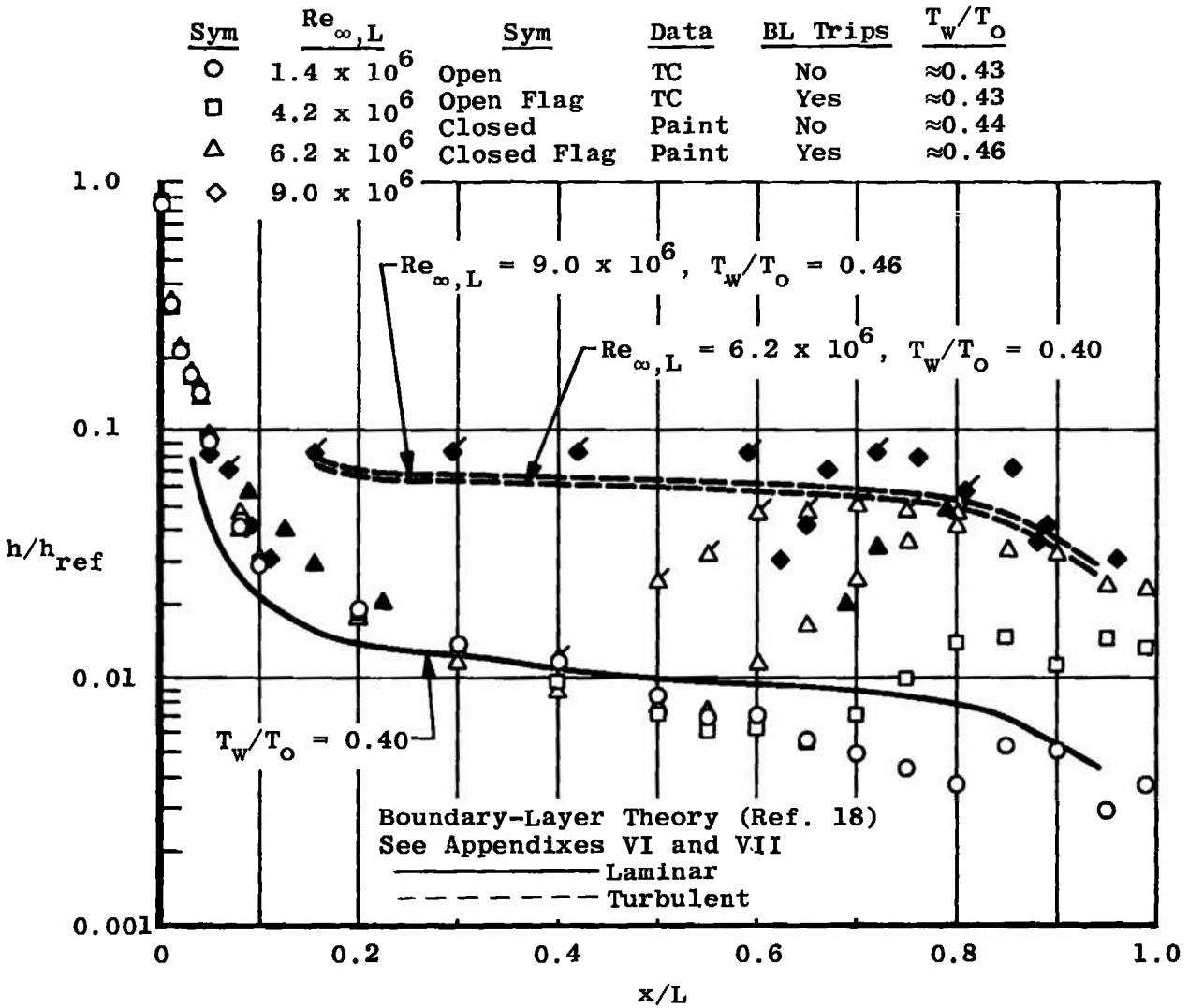

a. α = 10 deg

Fig. 25 Comparison of Experimental and Theoretical Orbiter Windward Centerline Heat-Transfer Distribtuions

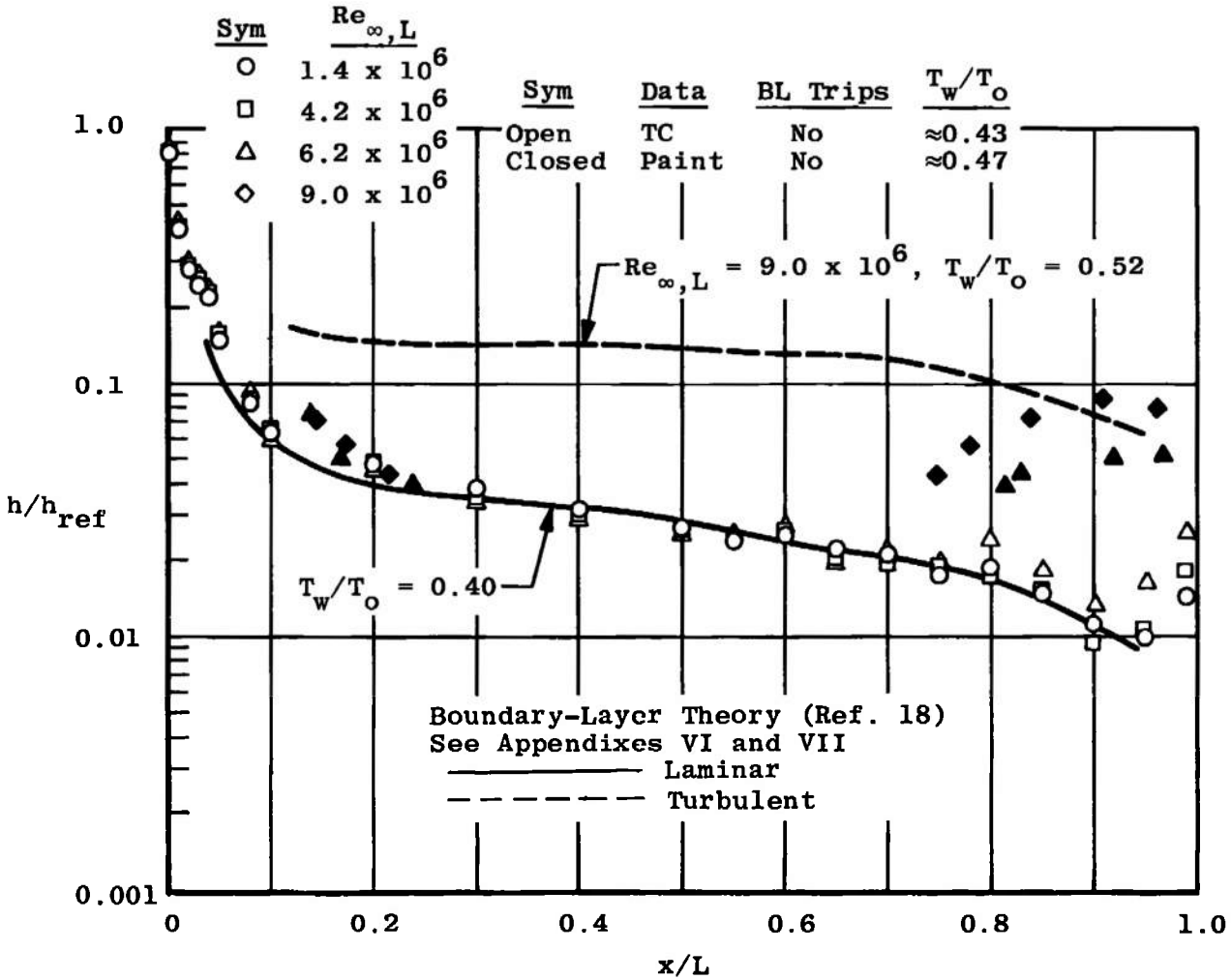

b. α = 20 deg

Fig. 25 Continued

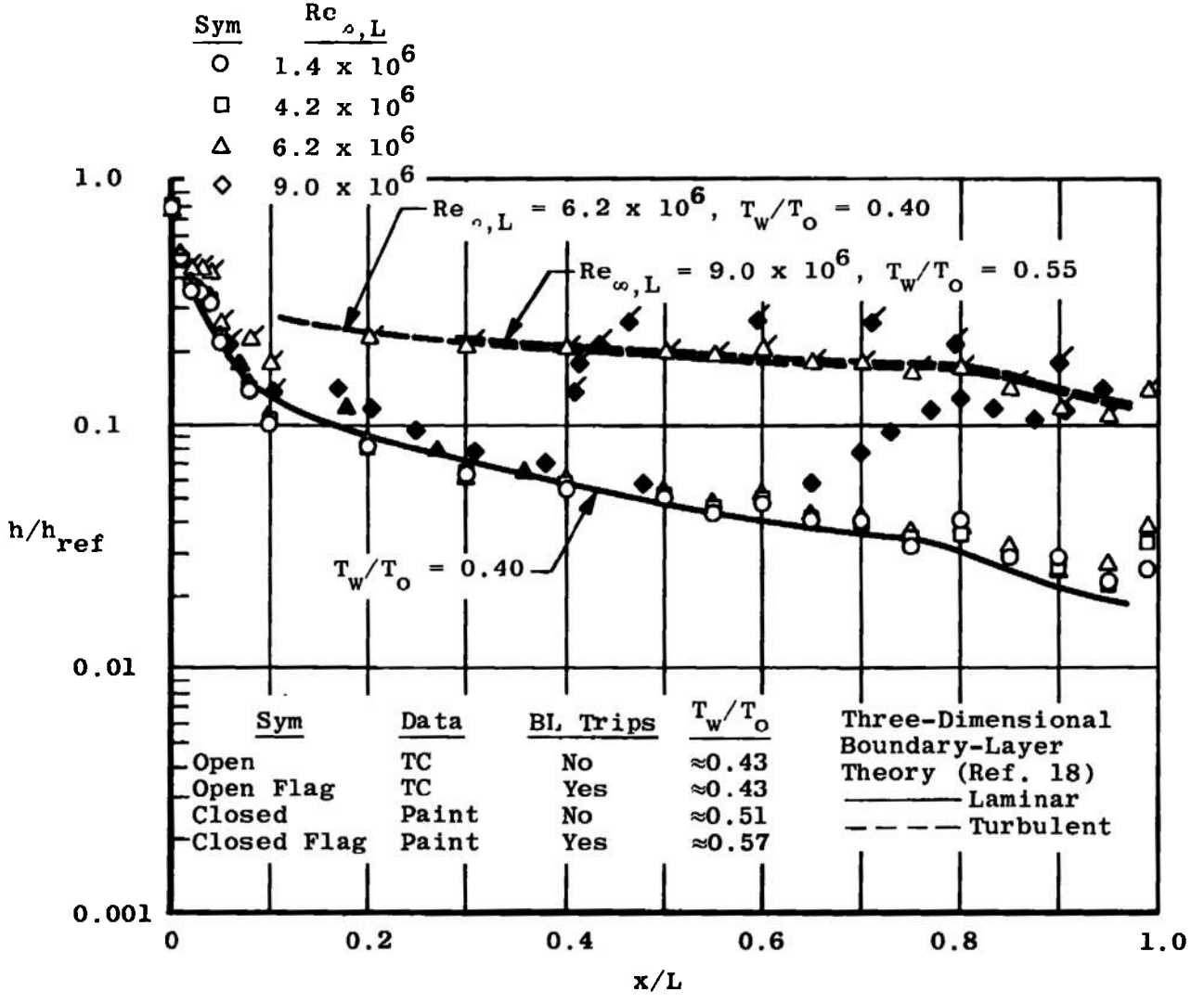

c. α = 30 deg

Fig. 25 Continued

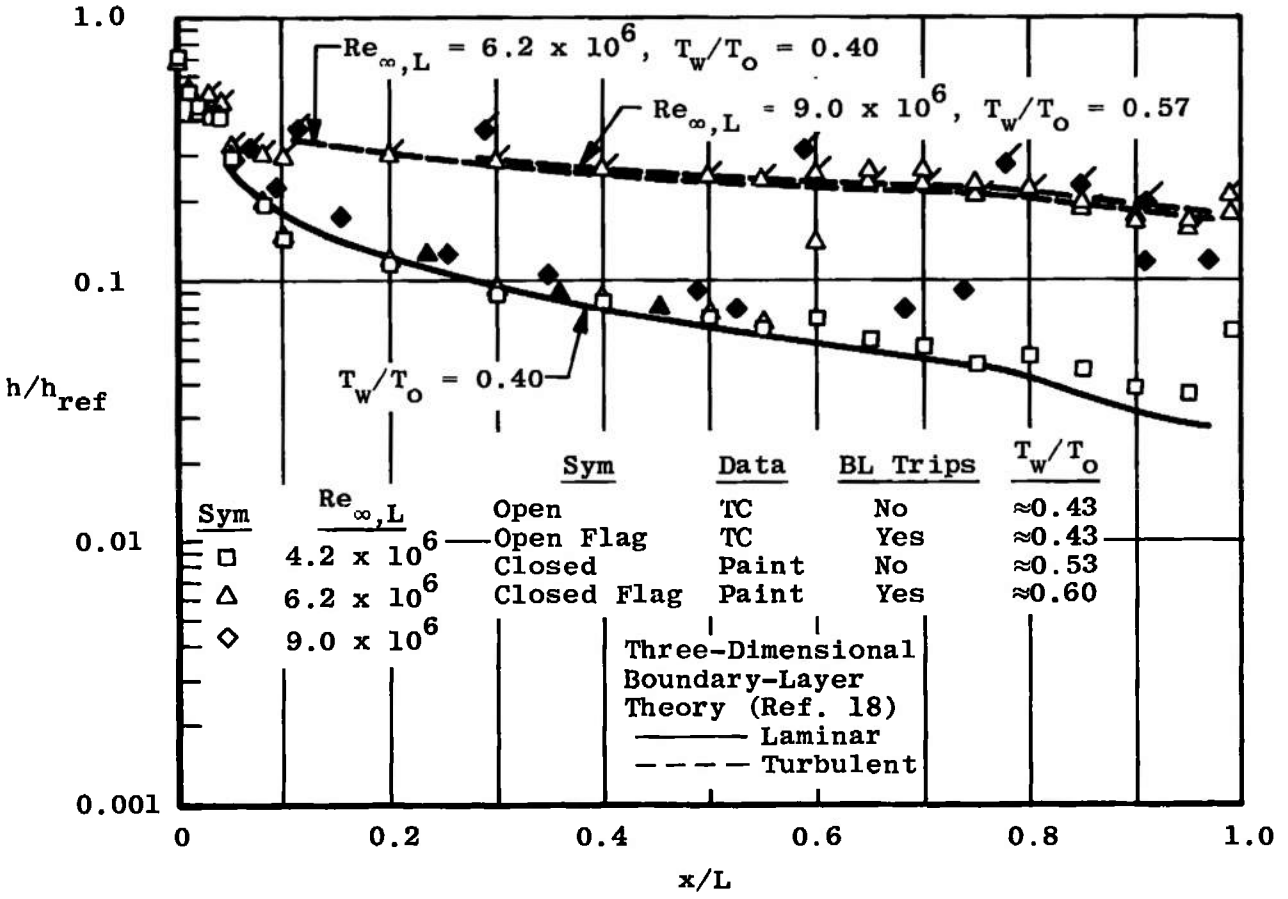

d. α = 40 deg

Fig. 25 Continued

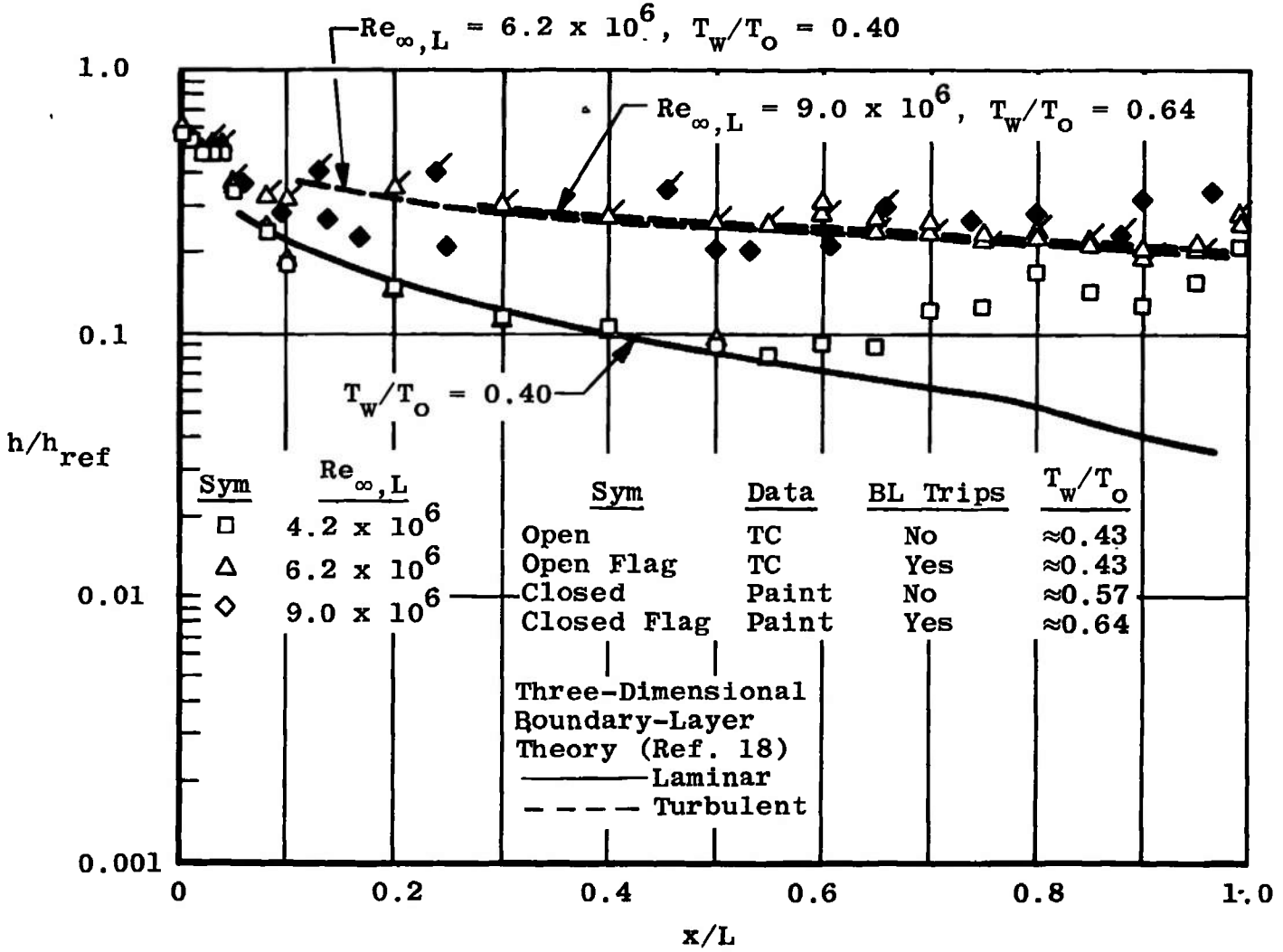

e. α = 50 deg

Fig. 25 Concluded

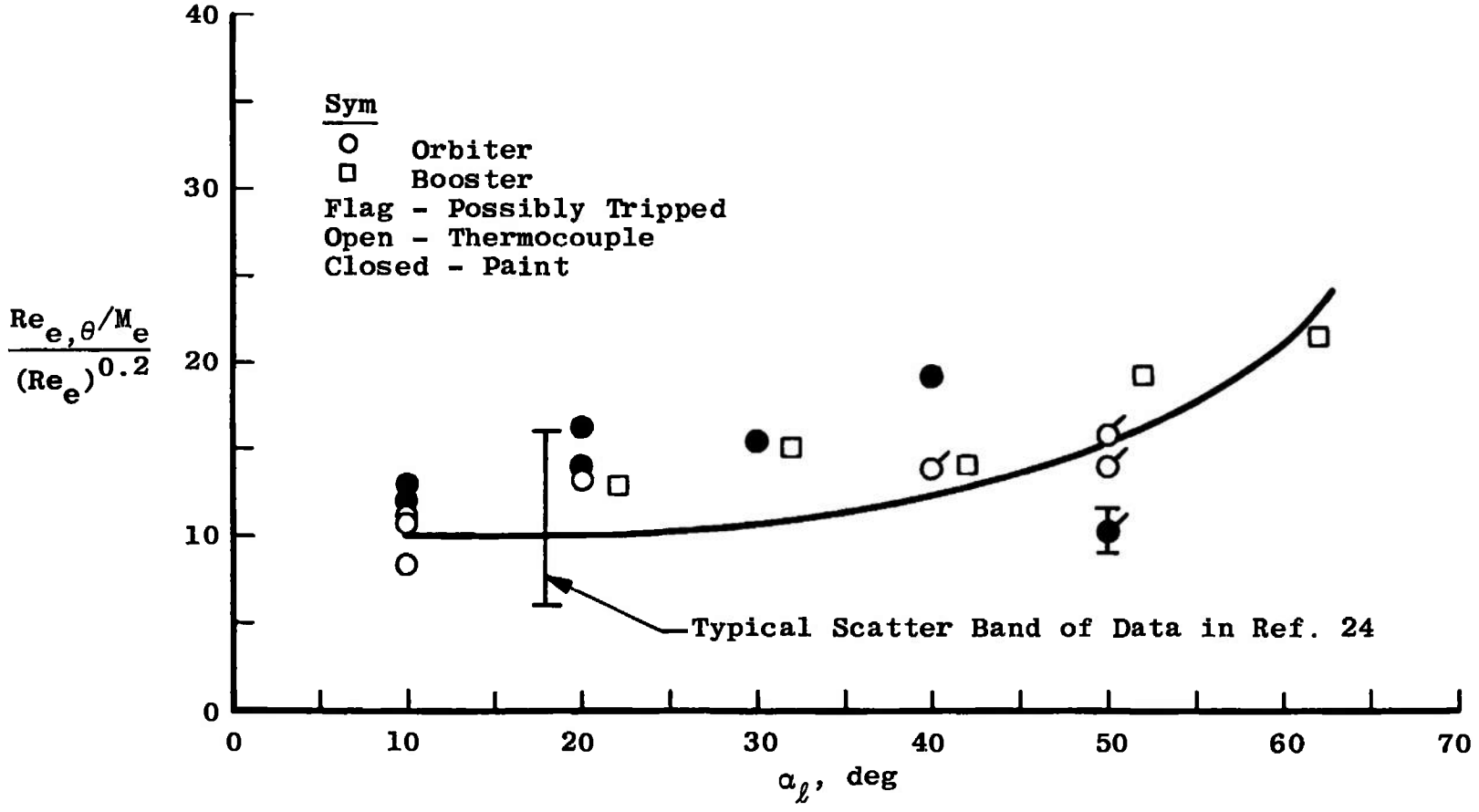

Fig. 26 Comparison of the Present Transition Results with the Kipp-Masek Correlation

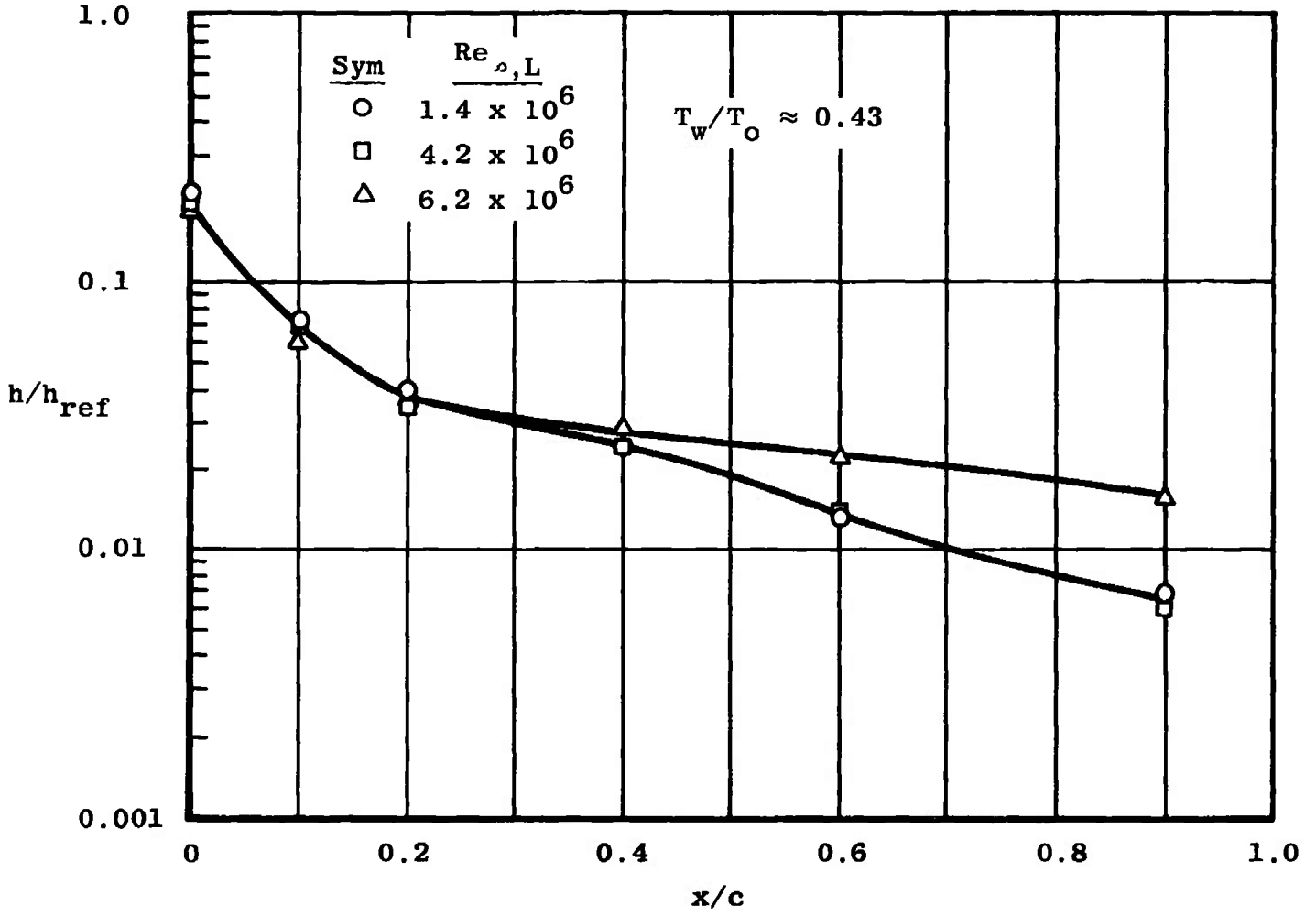

a. α = 10 deg

Fig. 27 Orbiter Windward Wing Heat-Transfer Distributions at Quarter Span

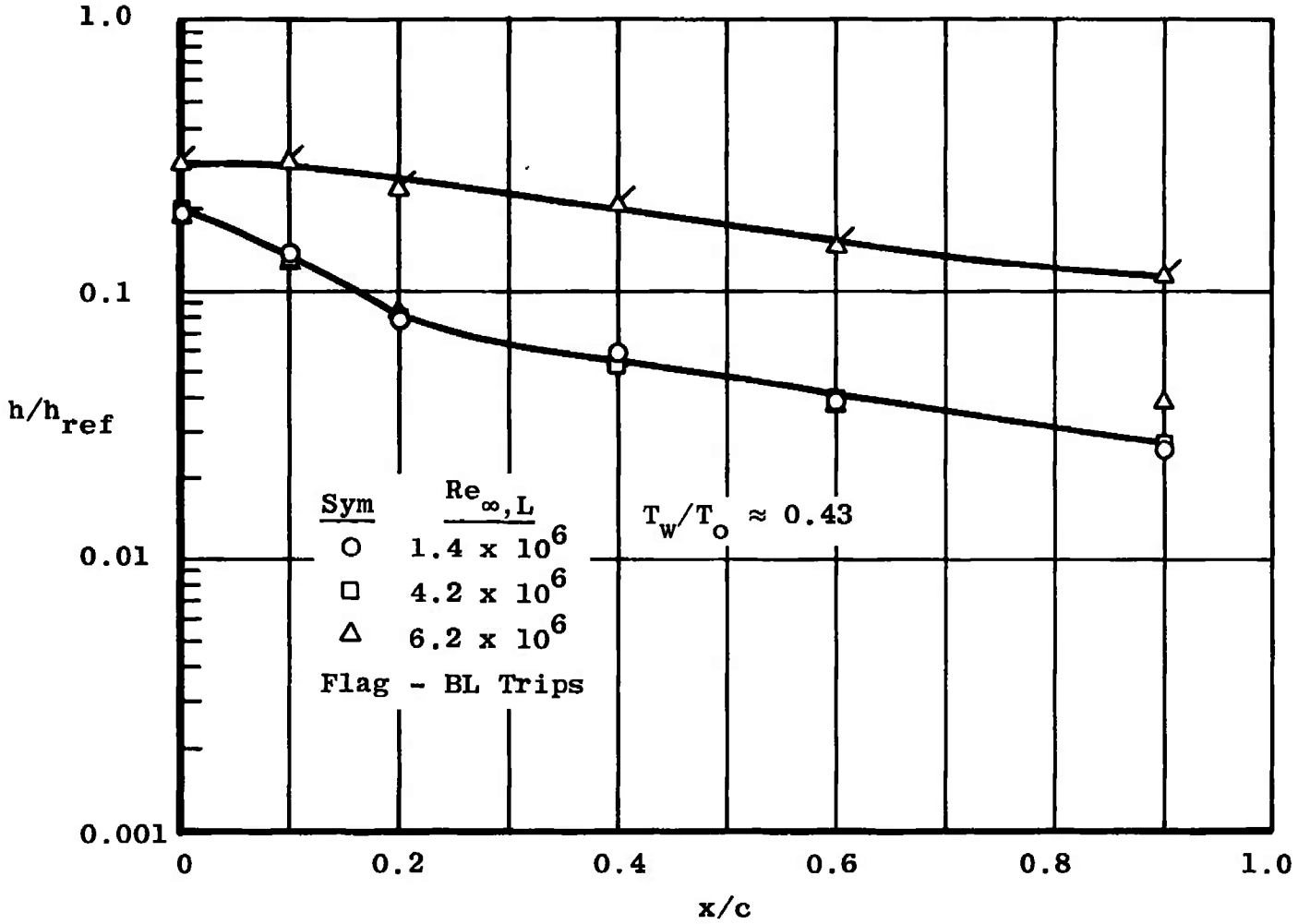

b. α = 30 deg

Fig. 27 Continued

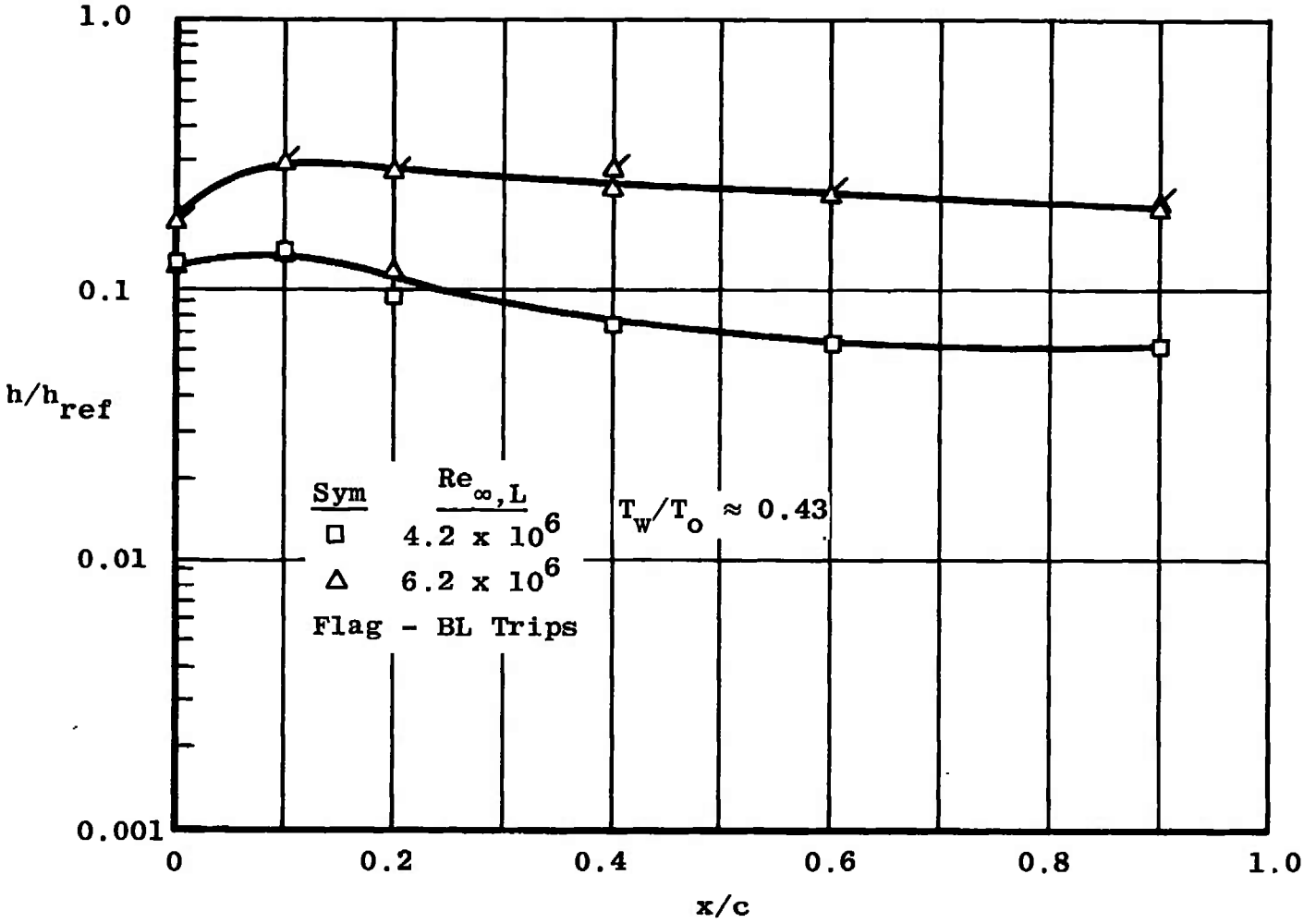

c. α = 50 deg

Fig. 27 Concluded

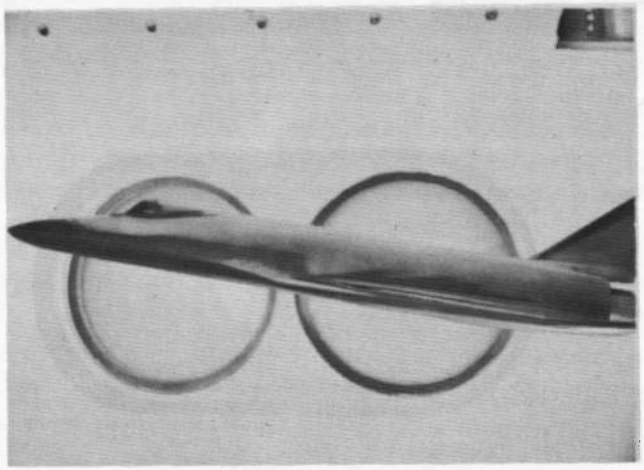

a. α = 10 deg, h/h_{ref} = 0.022, $Re_{\infty,L}$ = 6.1 x 10^6

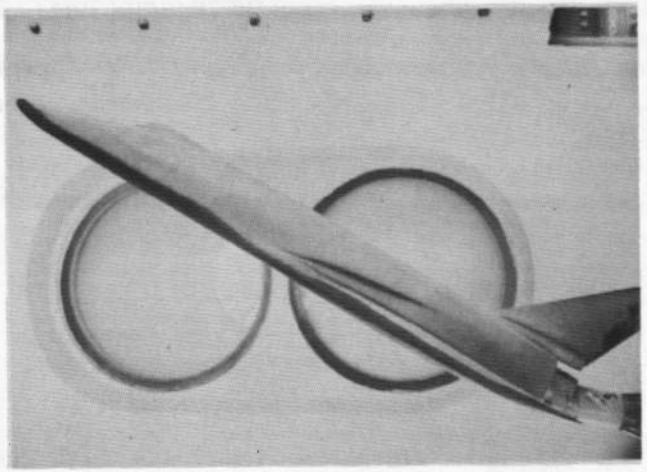

b. α = 30 deg, h/h_{ref} = 0.078, $Re_{\infty,L}$ = 9.0 x 10^6

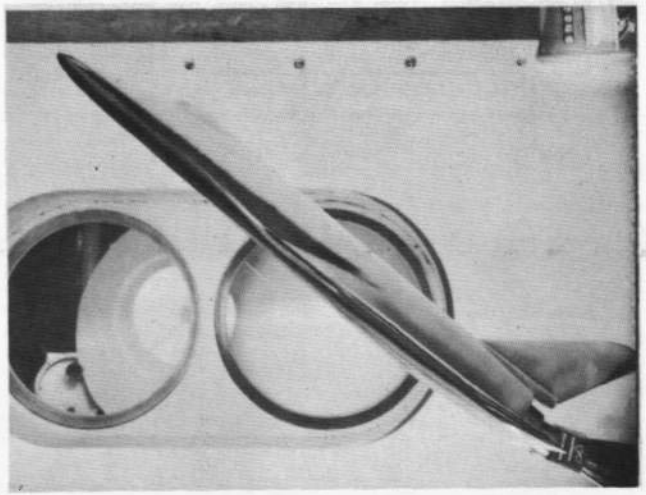

c. α = 40 deg, h/h_{ref} = 0.019, $Re_{\infty,L}$ = 6.1 x 10^6

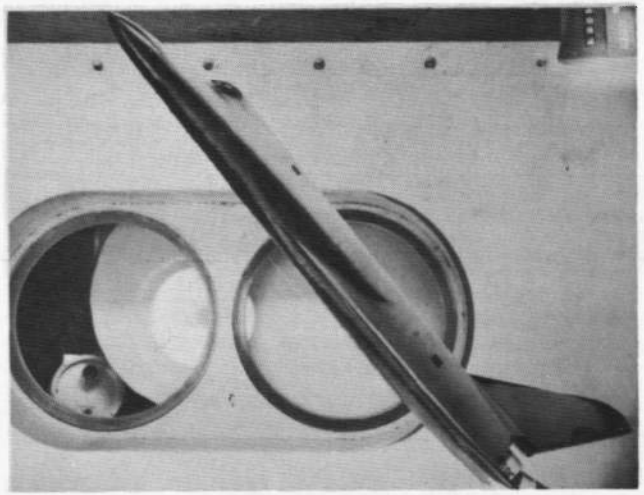

d. α = 50 deg, h/h_{ref} = 0.019, $Re_{\infty,L}$ = 9.0 x 10^6

Fig. 28 Samples of Side-View Phase-Change Paint Photographs

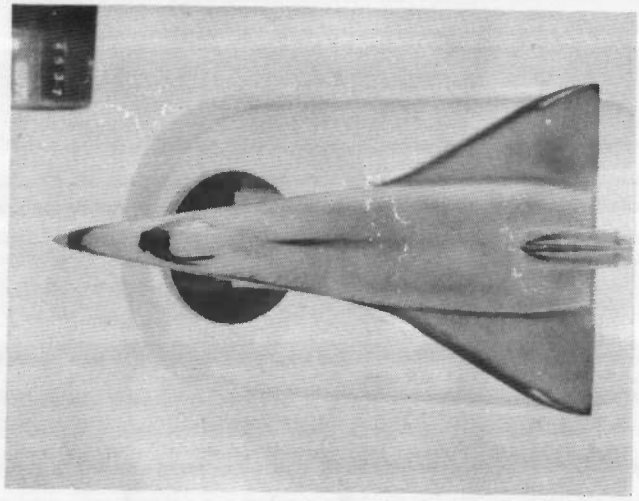

a. α = 10 deg, h/h_{ref} = 0.030, $Re_{\infty,L}$ = 9.0 x 10^6

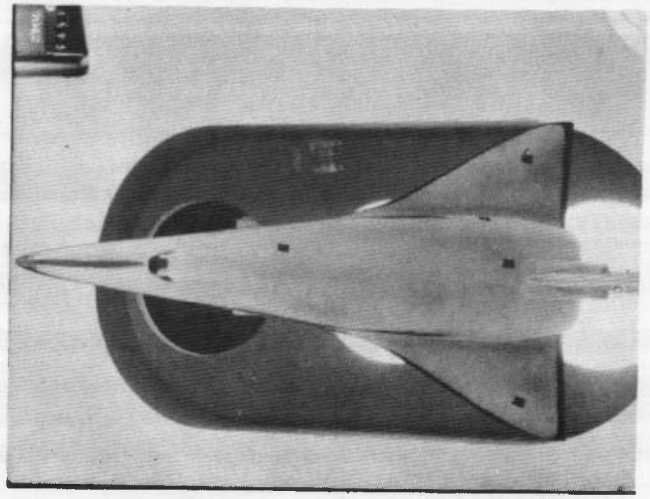

b. α = 40 deg, h/h_{ref} = 0.021, $Re_{\infty,L}$ = 9.0 x 10^6

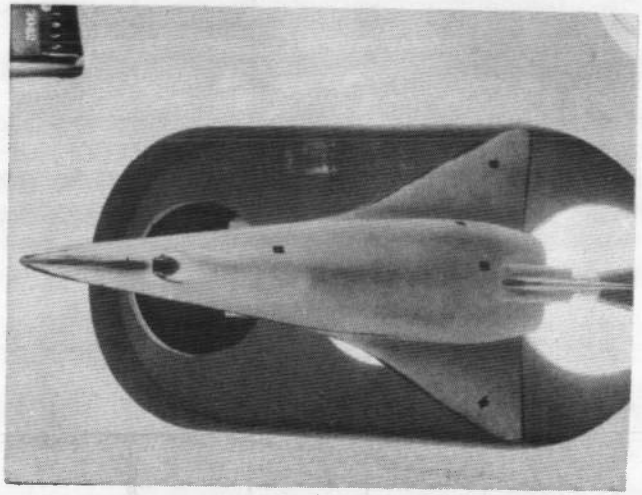

c. α = 50 deg, h/h_{ref} = 0.034, $Re_{\infty,L}$ = 9.0 x 10^6

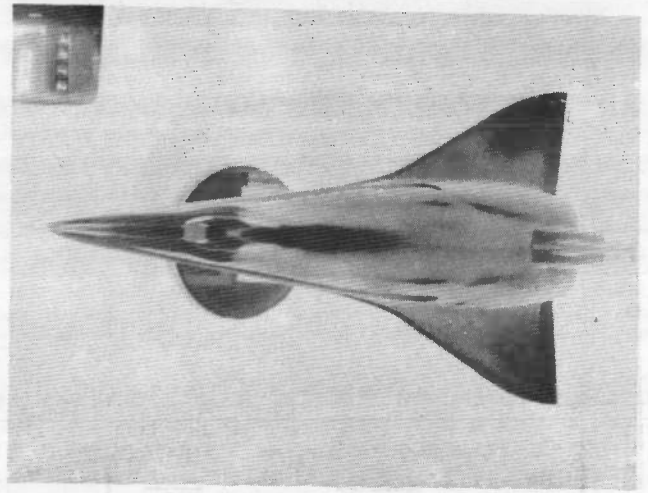

d. α = 50 deg, h/h_{ref} = 0.014, $Re_{\infty,L}$ = 9.0 x 10^6

Fig. 29 Lee Surface Phase-Change Paint Photographs

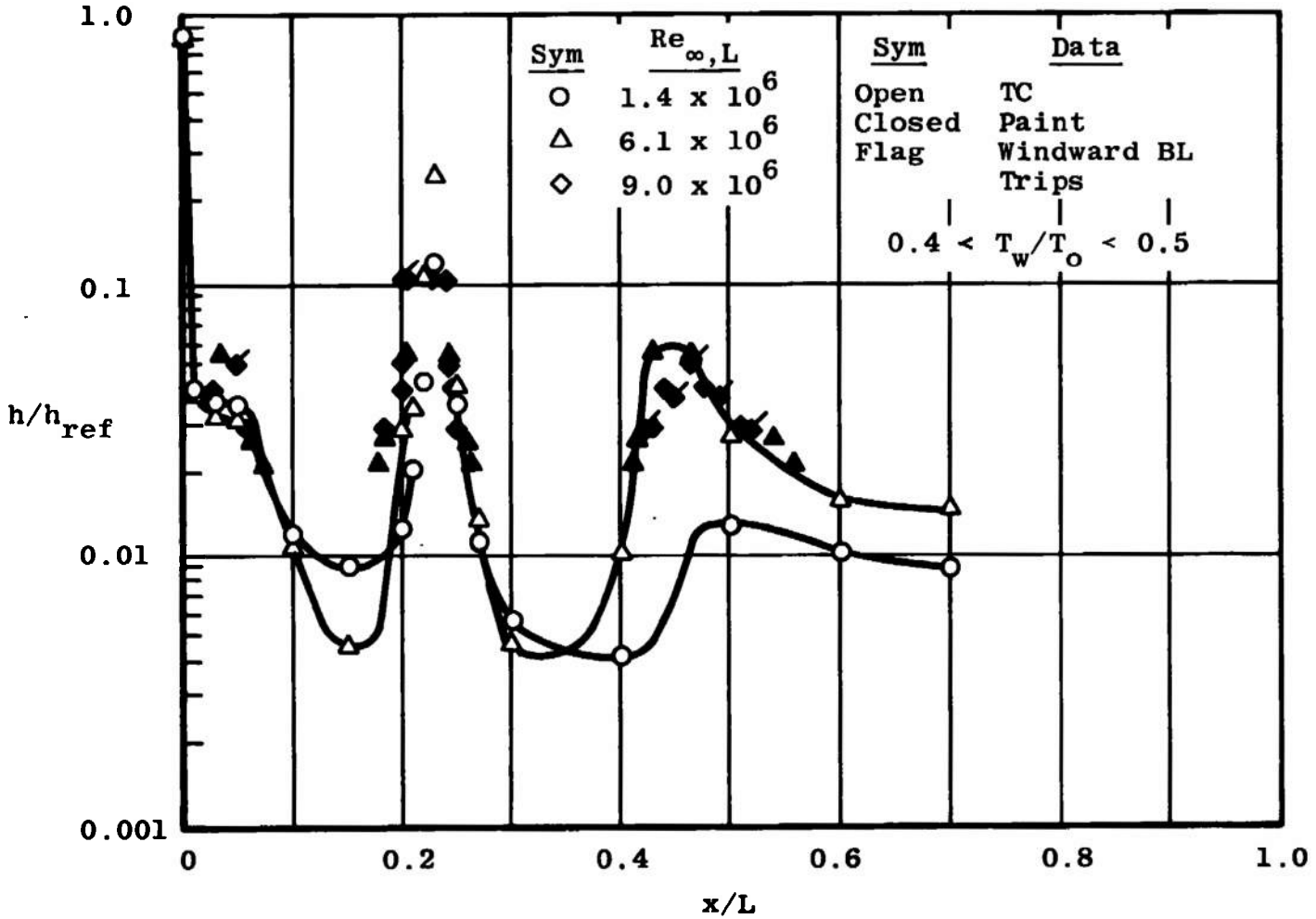

a. α = 10 deg

Fig. 30 Orbiter Leeward Centerline Heat-Transfer Distributions

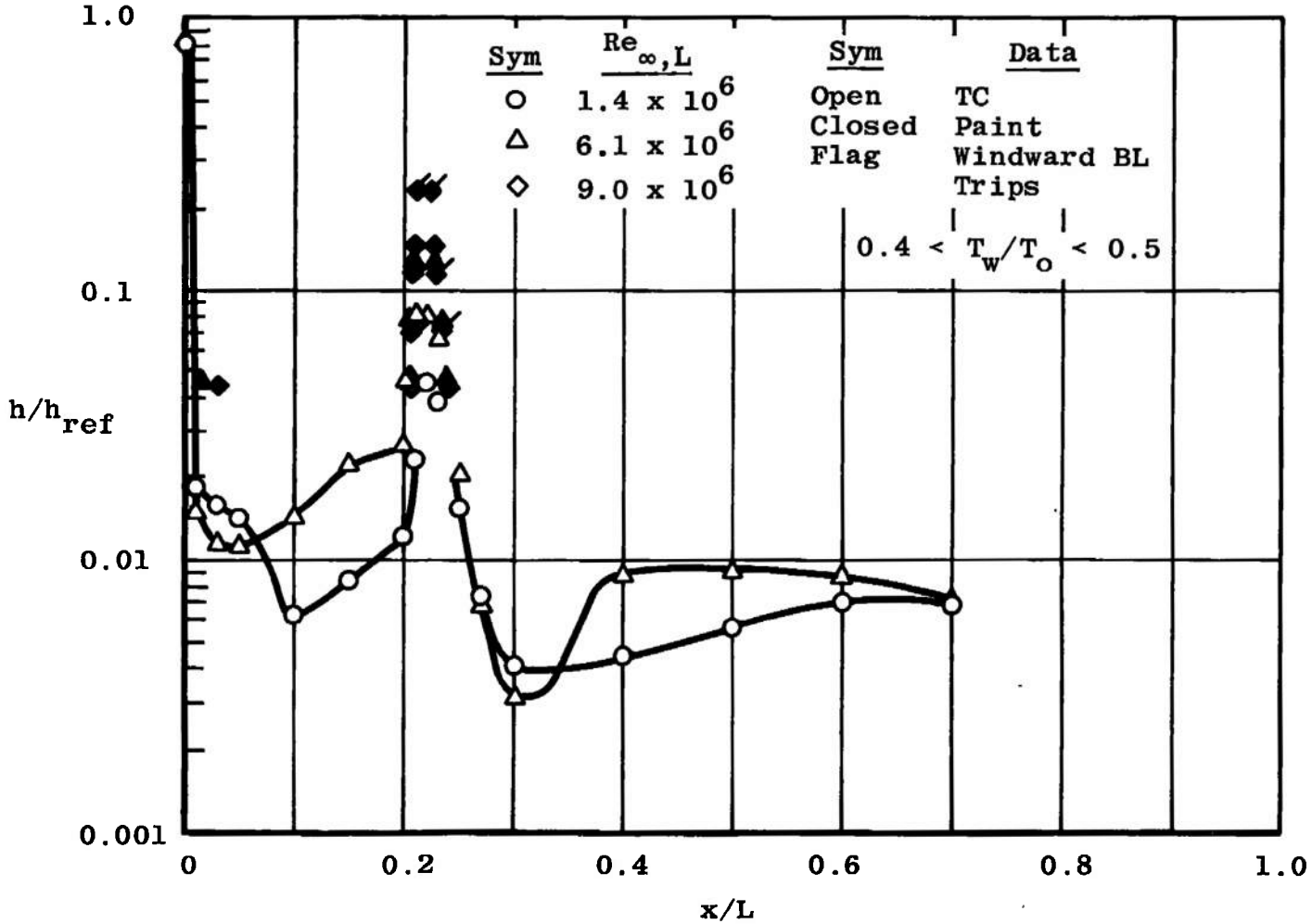

b. α = 20 deg

Fig. 30 Continued

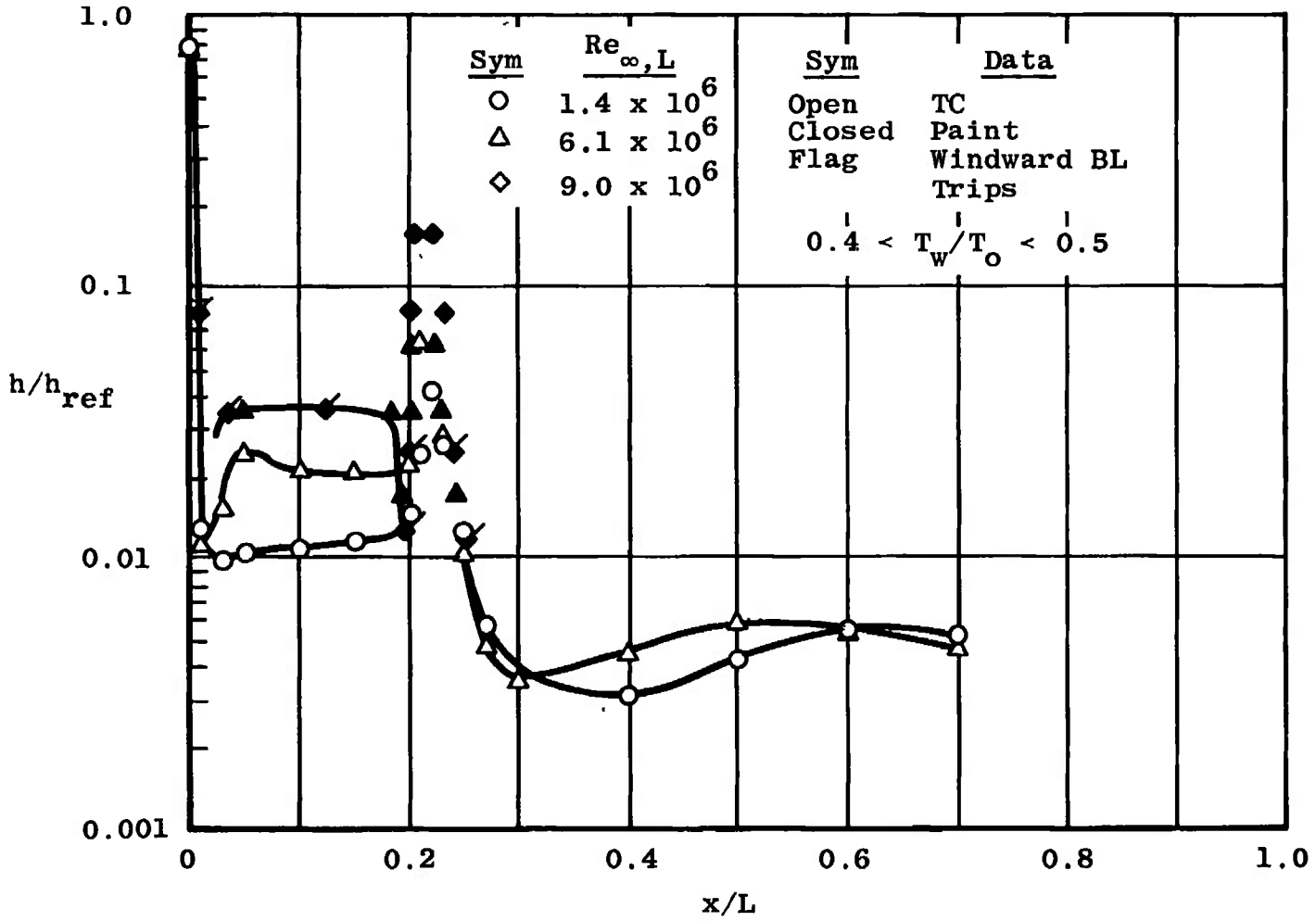

c. α = 30 deg

Fig. 30 Continued

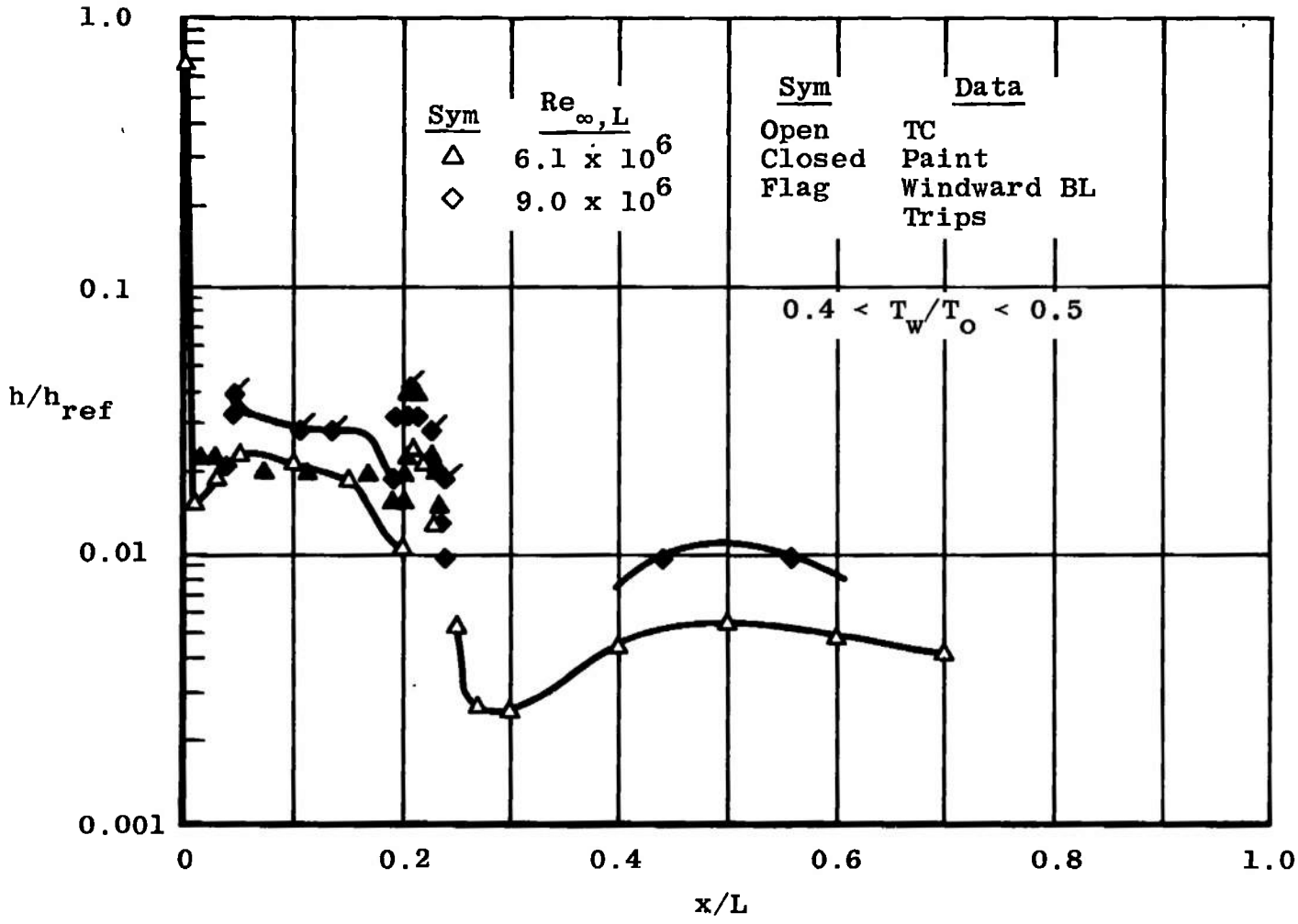

d. α = 40 deg

Fig. 30 Continued

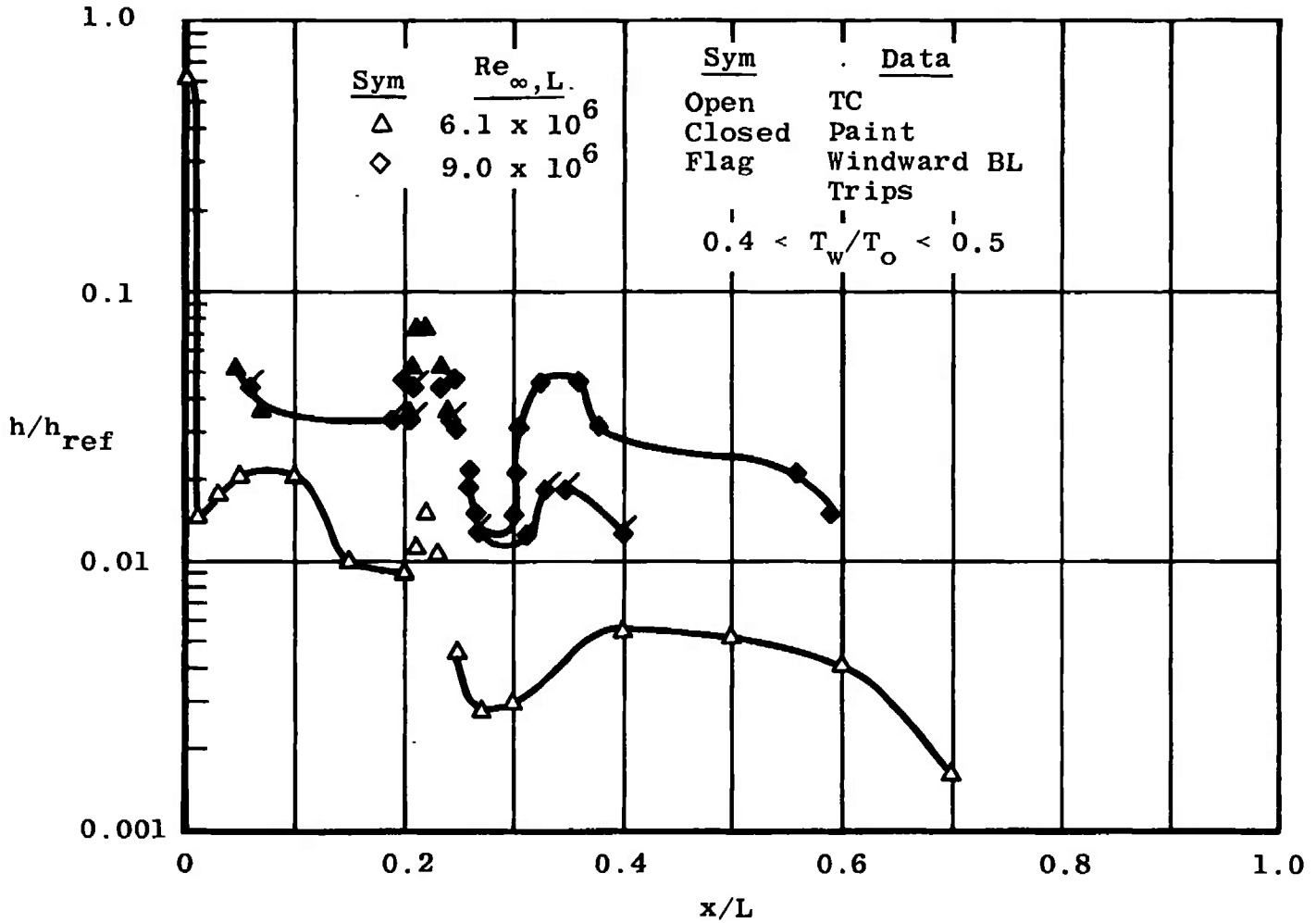

e. α = 50 deg

Fig. 30 Concluded

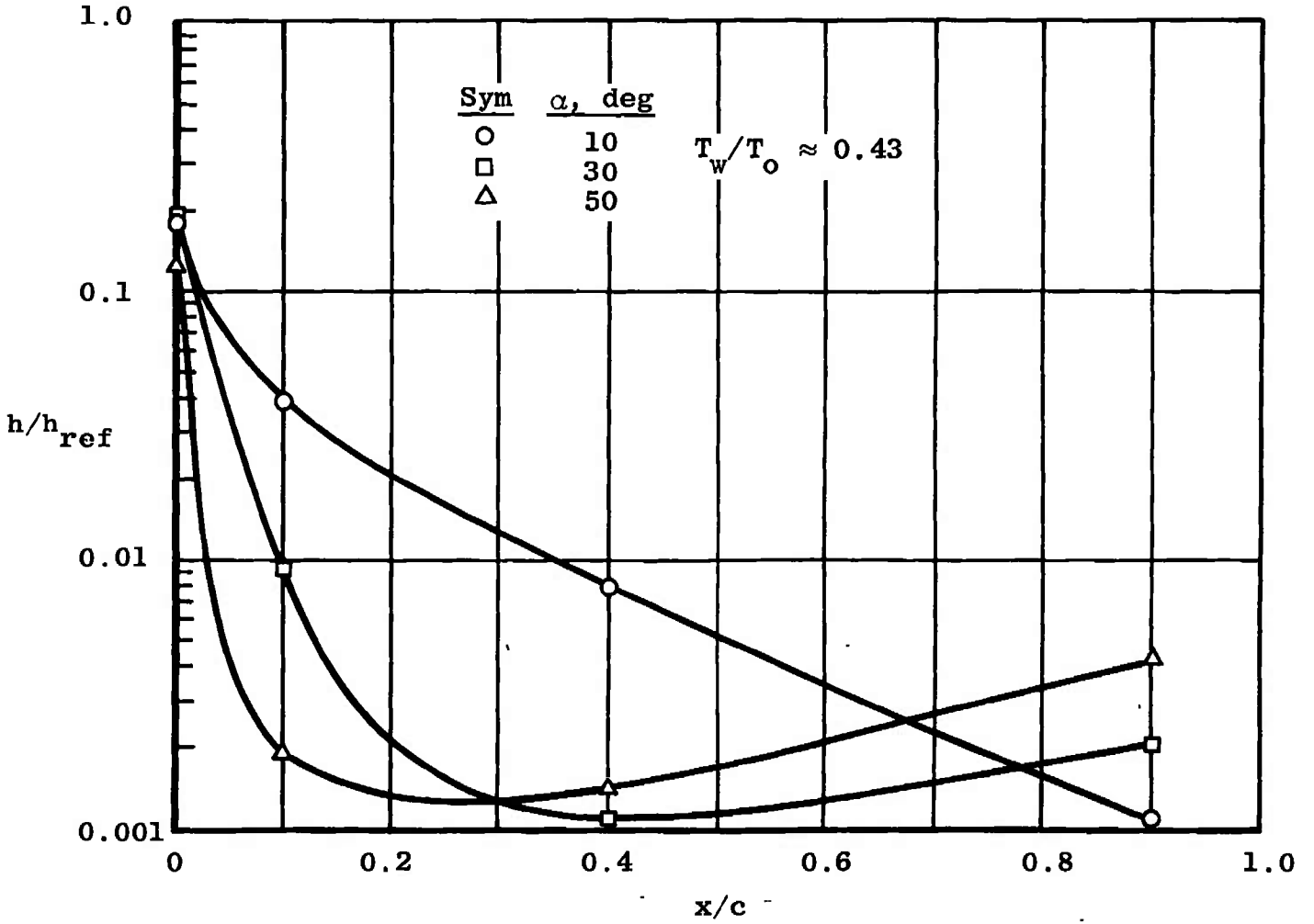

Fig. 31 Orbiter Leeward Wing Heat-Transfer Distributions at Quarter Span

APPENDIX II
EVALUATION OF STYCAST THERMAL PROPERTIES

A large portion of the present test program was devoted to testing phase-change paint models fabricated from Stycast 2762®. Stycast has been used for this purpose for several years because of its low diffusivity, ability to withstand the high temperatures experienced in hypersonic wind tunnels, and its molding characteristics.

The reduction of phase-change paint data to quantitative results requires knowledge of the model material thermal properties. Normally, models are fabricated from materials having low diffusivity, and semi-infinite solid assumptions are used to infer heating rates from the observed surface temperature response. Specifically, the product ρck, where ρ is density, c is specific heat, and k is thermal conductivity, is needed. There are two basic methods of obtaining the ρck values. First, an analysis of the material can provide values for the individual properties. Second, a technique which utilizes a known heat input to the material can be used to infer the material properties from the surface temperature response. This method normally takes the form of a wind tunnel test of a sphere model of the subject material. For this test program, both techniques were employed to provide a check of the procedures and to optimize data precision.

ANALYSIS

Phase-change paint data reduction, including the sphere calibration technique, utilizes the equation governing the surface temperature response of a semi-infinite solid which experiences a step heating input.

$$\frac{T_w - T_{wi}}{T_{aw} - T_{wi}} = 1 - e^{\beta^2} \operatorname{erfc}\beta$$

where

$$\beta = \frac{h\sqrt{\Delta t}}{\sqrt{\rho ck}}$$

For normal data reduction, this equation is solved for h, the heat-transfer coefficient. The sphere calibration technique uses a theoretical value for h, and the model thermal properties ($\sqrt{\rho ck}$) are determined.

For the present test program, a 6-in.-diam hemisphere model was cast and cured with each Stycast model to permit evaluation of batch-to-batch uniformity. Because of apparent inconsistencies in the hemisphere data, a number of repeat runs were made on one hemisphere model, and these results follow.

Prior to testing, the model was striped with a thin coat of high-temperature paint to permit visual identification of the phase-change locations. The stripes were applied circumferentially at 10-deg intervals from the stagnation point (θ = 0) to the shoulder (θ = 90 deg). During a typical test run, the model was exposed to the tunnel flow about 20 sec. Several longer runs were made when the test conditions (i.e., the model wall temperature) permitted. The progression of the phase-change paint melt line over the model surface was recorded on 70-mm black-and-white film at 0.5-sec intervals.

The results of five runs shown in Fig. II-1 are plotted versus the model location at which the data were obtained. Two paint temperatures were used on runs 296 and 297 (the model was masked along the vertical centerline and the paints were sprayed on either side) to increase the amount of data from each run. The data scatter (±20 percent) was in excess of that expected, and a reason for the scatter was sought. The data were obtained at two Reynolds numbers and with four different paint temperatures. Since some variation of the material properties with temperature was expected, the data from Fig. II-1 were replotted versus paint (or wall) temperature, as shown in Fig. II-2. The results of an analysis of the model material (individual ρ, c, k measurements) are also shown and indicate a slight trend with temperature for the lower wall temperatures. The hemisphere data, however, show no discernible trend with temperature. Note that the symbols defined in Fig. II-1 are used in all figures to permit identification of the individual data points.

Referring to Fig. II-1, a trend with θ is observed; that is, as θ increased, $\sqrt{\rho ck}$ generally decreased. It was speculated that, since the model was cast with the nose (θ = 0) down, heavier parts of the material may have settled toward the nose during curing, thus altering the material thermal properties. To experimentally evaluate this possibility, a run was made with the hemisphere at 30-deg angle of attack. The results of this run are compared with run 296 in Fig. II-3. To facilitate data comparison, θ was measured from the stagnation point in each case so that, if the material properties varied around the model, a shift of 30 deg in the data should be evident. In fact, no shift occurred, and it was concluded that material uniformity in the θ direction was not a problem. Note that these additional data increased the total data spread to ±34 percent.

Since the only discernible trends appeared to be related to θ, the theoretical predictions used for h versus θ were reviewed and compared with data from thermocouple and heat-rate gage models. This comparison confirmed the technique being used and thus shed no light on the problem.

Attention was turned to the heating time since this is one of the basic experimental variables. Injection of the model through the tunnel boundary layer could introduce up to 0.5-sec uncertainty in the heating time. However, an error of about three seconds would be required to produce the $\sqrt{\rho ck}$ variation shown in Fig. II-3. The data were plotted versus $\sqrt{\Delta t}$ as shown in Fig. II-4, and some improvement in data scatter was observed, although the $\sqrt{\rho ck}$ variation still existed. A straight-line fairing of the data is shown and correlates the $\sqrt{\rho ck}$ variations within about ±10 percent. A variation of $\sqrt{\rho ck}$ with time could be caused by variation of thermal properties with material depth since the diffusion of heat in a solid is basically a function of time. To check this possibility, two investigations were made. First, the model was sliced normal to the surface, and the sliced surface was polished to expose the structure of the material. A 40-X photographic enlargement of this surface is shown in Fig. II-5. The photograph clearly shows a concentration of lighter colored particles near (<0.050 in.) the model surface. Since Stycast is a mixture of epoxy (black) and alumina (Al_2O_3), the light particles are assumed to be alumina. The epoxy has thermal properties quite different from alumina. Typical values for $\sqrt{\rho ck}$ are 0.04 for epoxy and 0.35 for alumina. Obviously the thermal properties of the mixture (Stycast) are sensitive to the distribution of the alumina particles.

To check the effect of the apparent alumina concentration near the surface, the second investigation was made. Two samples of the model material were checked for thermal properties in the VKF Instrument Laboratory. Thin-film resistance elements were deposited on the surface of the samples. Temperature-resistance calibrations of the elements were made, and the surfaces were then subjected to a very short (0.1-sec) calibrated convective heat pulse. This procedure is commonly used to calibrate heat-rate gages for short-duration test applications and permitted a $\sqrt{\rho ck}$ evaluation similar to the sphere calibration technique. The $\sqrt{\rho ck}$ values thus obtained are plotted in Fig. II-4 and identified as VKF laboratory data. Each point represents the average of three runs, and about ±10 percent scatter existed in these data. These results pre-

sent a strong confirmation of the time correlation since the fairing of the hemisphere data extrapolates very near to the laboratory points.

To check the compatibility of the $\sqrt{\Delta t}$ correlation with the observed material nonuniformity, an analytical model was formulated. A distribution of material thermal properties with depth was assumed, and the surface temperature response to a convective heat input was computed. This surface temperature response was compared with constant property solutions to infer an effective constant $\sqrt{\rho ck}$. From these solutions, the variation of the effective $\sqrt{\rho ck}$ with time was plotted and compared with the hemisphere data. These results are presented in Fig. II-6 and basically confirm the validity of the $\sqrt{\Delta t}$ correlation. The analytic models of $\sqrt{\rho ck}$ variation with depth were chosen to approximate the limits in $\sqrt{\rho ck}$ variation shown in Fig. II-4 and the alumina distribution shown in Fig. II-5.

CONCLUSIONS AND RECOMMENDATIONS

1. The scatter in the Stycast 2762 thermal property data obtained at VKF was reduced from ±34 percent to ±10 percent by correlation with time. The equation used in the data reduction was
   $\sqrt{\rho ck} = 0.11 - 0.008\sqrt{\Delta t}$.
2. The validity of the time correlation is attributed to variation in the alumina filler distribution in the material.
3. These results should not be applied directly to other test data since the cause of the nonuniform filler distribution is unknown.

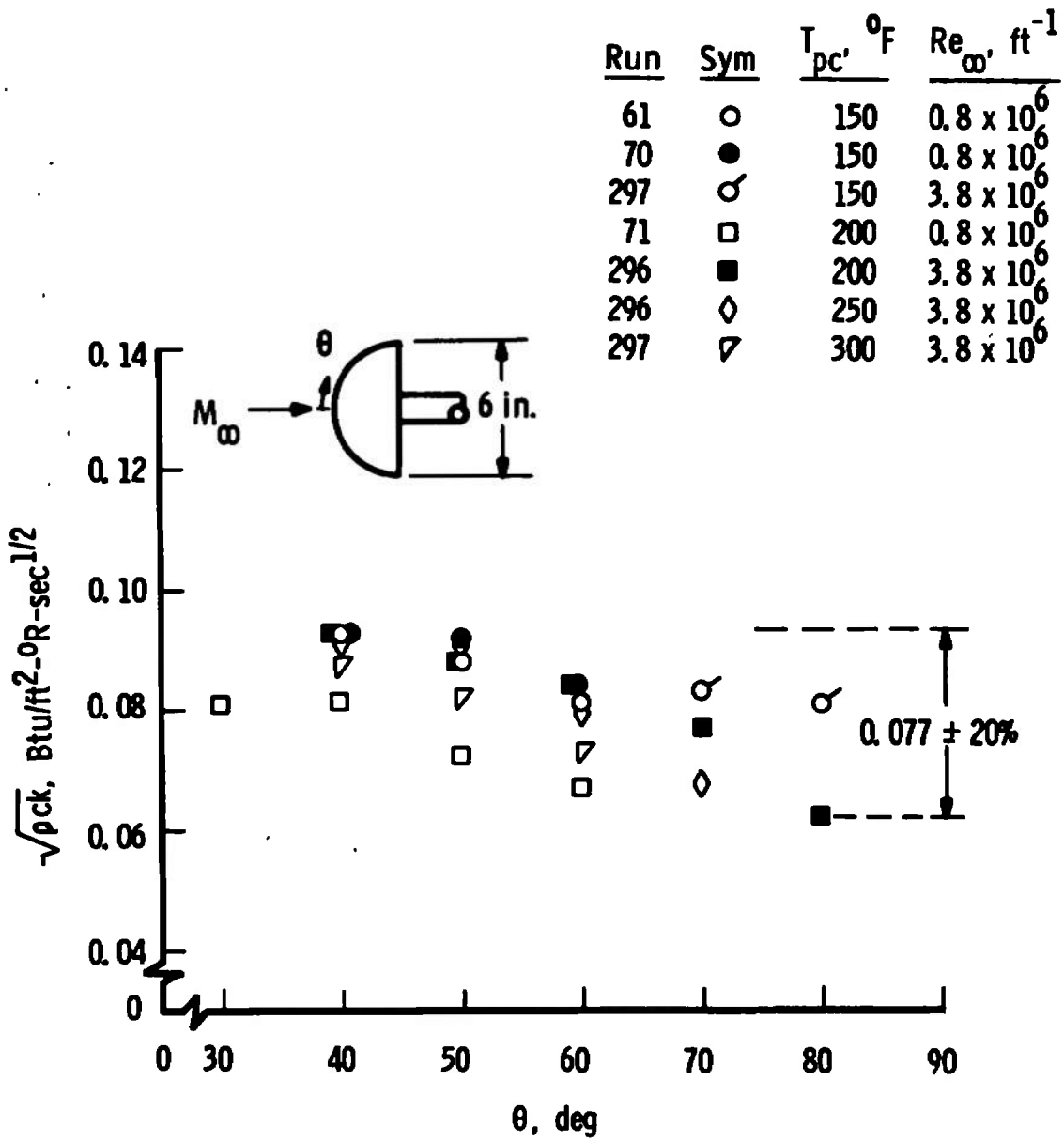

Fig. II-1 Model Material Thermal Property Variation with Model Location

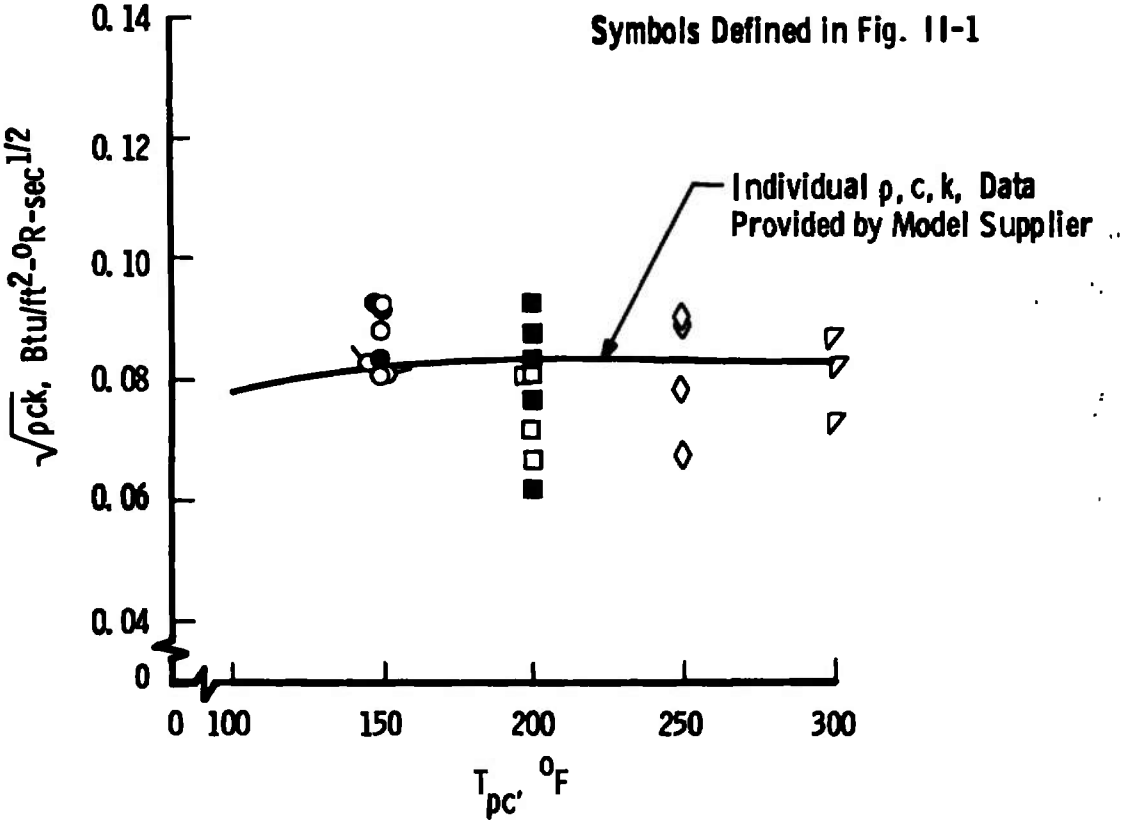

Fig. II-2 Thermal Property Variation with Wall Temperature

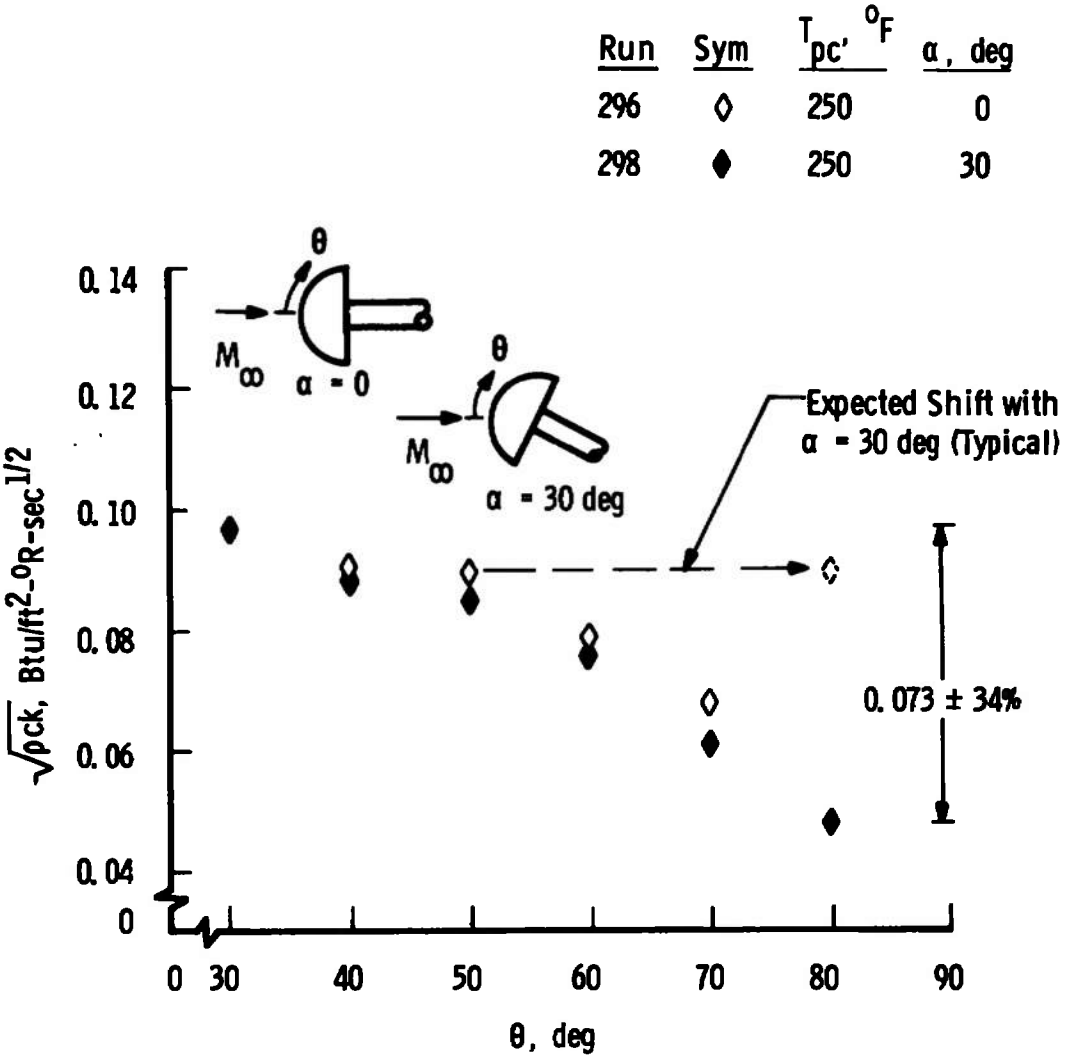

Fig. II-3 Thermal Property Variation with Location for 0- and 30-deg Angle of Attack

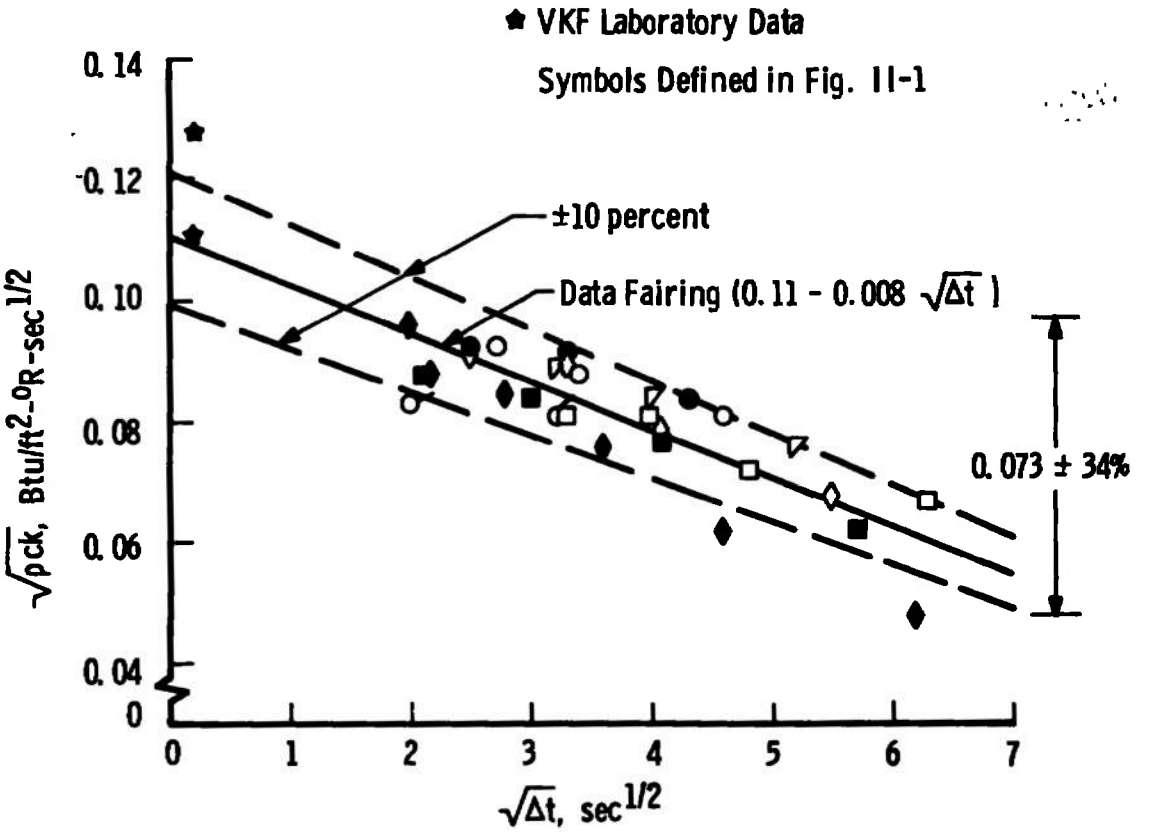

Fig. II-4 Correlation of Thermal Properties with Time

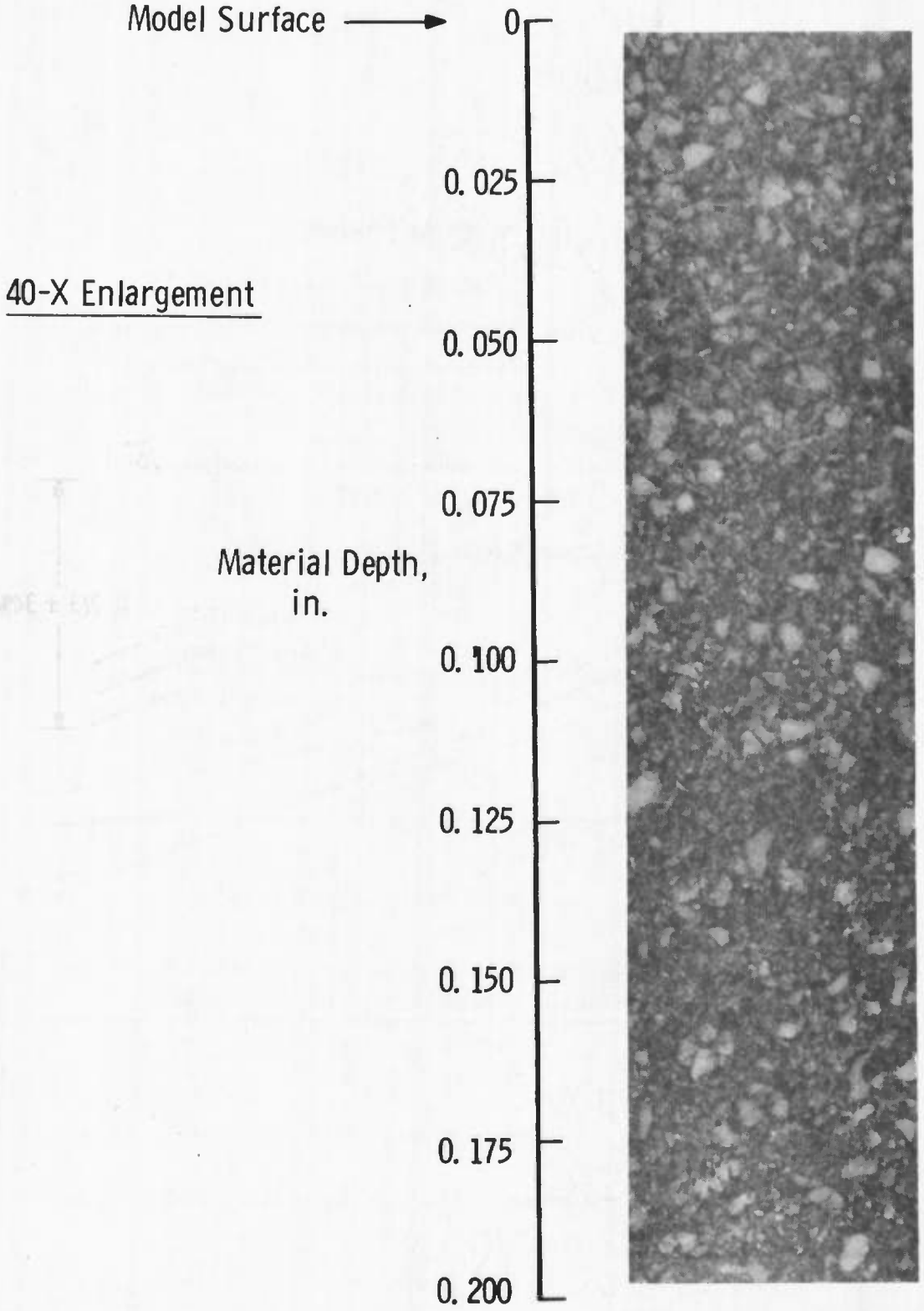

Fig. II-5 Photographic Enlargement of Stycast Structure near the Model Surface

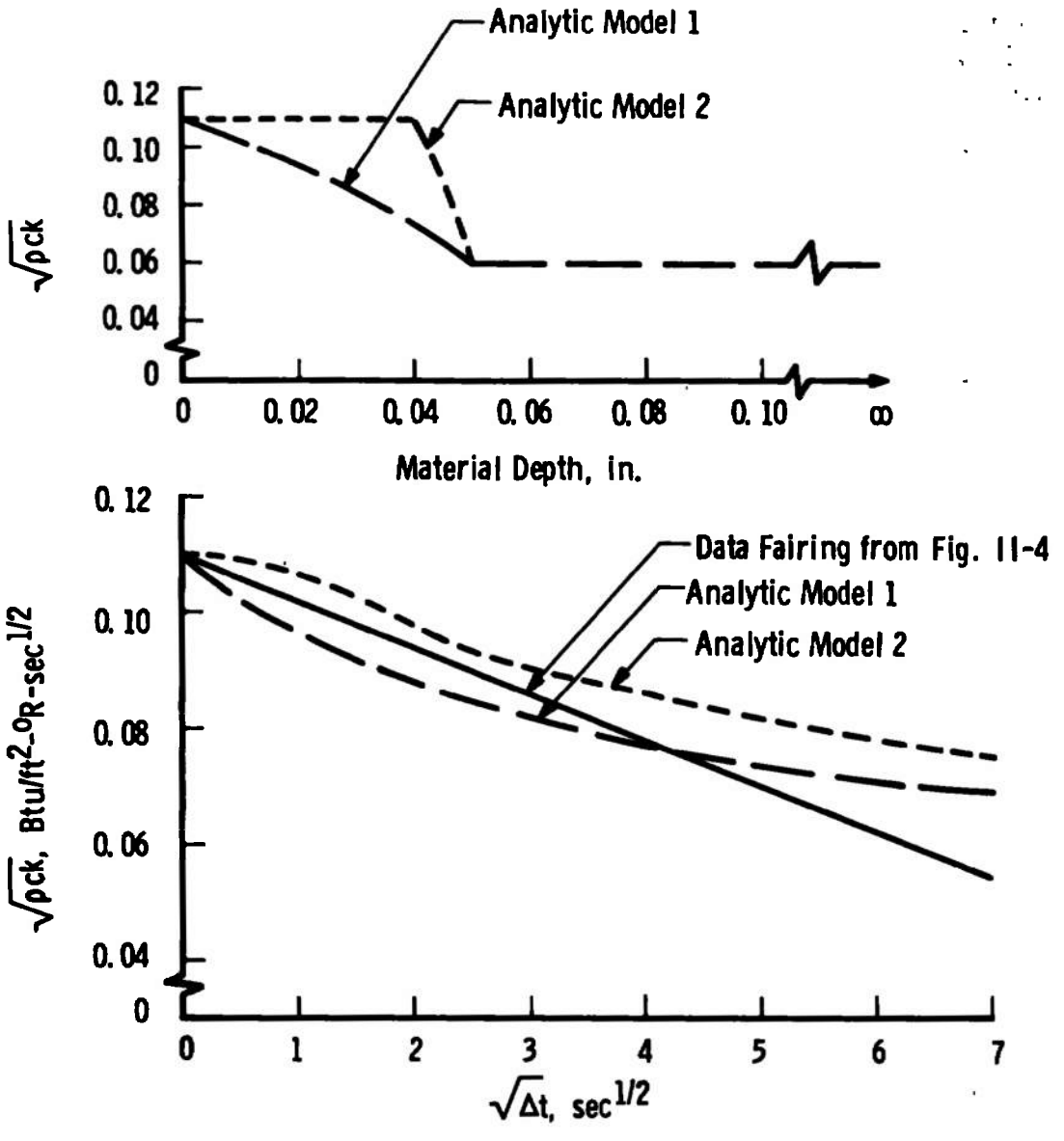

Fig. II-6 Comparison of Analytic Results with Hemisphere Calibration Data

APPENDIX III
PHASE-CHANGE PAINT DATA REDUCTION ASSUMPTIONS

A complete description of the phase-change paint technique, including the assumptions made, was presented in Ref. 25. A summary of the assumptions listed in Ref. 25, and others applicable to the present tests, is given below.

1. The depth of heat penetration into the wall is less than the wall thickness and very small compared to the surface radius of curvature so that the wall acts like a one-dimensional semi-infinite slab. The present models were solid Stycast, and therefore this assumption should be valid with the exception of small radius edges.

2. The model is isothermal before injection into the airstream. Thermocouples embedded within the model were monitored to ensure that the model was isothermal before injection.

3. The surface experiences an instantaneous step in local aerodynamic heat-transfer coefficient at time zero, and this coefficient is invariant with time. The models were exposed to the tunnel airflow approximately 0.7 sec before reaching the tunnel centerline and this time is considered in determining time zero. By not considering photographs obtained during the first 3 sec of model exposure, uncertainties in heat-transfer coefficient attributable to errors in time are minimized. Analysis of thermocouple data has indicated that in some instances the heat transfer coefficient overshoots the steady-state value as the model is being injected. In these cases more than 3 sec may be needed before errors in the measured heat-transfer coefficient are negligible.

4. The thermal diffusivity and conductivity of the wall is invariant with temperature. An evaluation of the Stycast thermal properties is presented in Appendix II.

5. The phase-change coating melts when the wall temperature reaches the specified value (i. e., $T_{pc} = T_w$). Uncertainties in the specified phase-change temperature are estimated by the manufacturer to be ±1 percent.

6. The radiation heating produced by the fluorescent lighting and model radiation to the tunnel walls are negligible compared with the aerodynamic heating.

7. The metallic noses did not distort either the temperature distribution in the model material or the development of the boundary layer.

8. As discussed by Throckmorton (Ref. 26) the largest uncertainty in the reduction of phase-change paint data is probably caused by observer interpretation. The reduction of phase-change paint data requires the visual identification of the melt line, and its identification may vary from one observer to another.

APPENDIX IV
FLOW-FIELD REGIMES ON THE WINDWARD SURFACE OF THE NORTH AMERICAN ROCKWELL ORBITER

The planform of the North American orbiter can be fairly well represented by an 81.5-deg sweep delta wing for values of x/L between 0.1 and 0.6. Even though the edges are rounded, the flow field should be basically similar to that of a sharp-edged delta wing at least at intermediate and high angles of attack.

The $\rho_r \mu_r$ heat-transfer method presented in Ref. 27 relates the variation in inviscid delta wing flow-field properties to centerline values through the use of the variable, n, which is the centerline flow divergence angle derivative,

$$\left[\frac{d\omega}{d\phi}\right]_{\phi=0} .$$

By assuming that the influence of the spanwise pressure gradient is negligible and combining Equations A10a, A10c, and A18 from Ref. 27, the following expression is obtained:

$$\frac{h}{h_{2D}} = \sqrt{1 + 2n}$$

Note that for

$$n = \left[\frac{d\omega}{d\phi}\right]_{\phi=0} = 1.0,$$

the result is the same as that obtained for the sharp cone to flat plate heating ratio.

$$\frac{h}{h_{2D}} = \sqrt{3}$$

An estimate of

$$\left[\frac{d\omega}{d\phi}\right]_{\phi=0}$$

for sharp-edged delta wings of various sweep angles at Mach Number 9.6 is shown in Fig. 74 of Ref. 28 and is reproduced here as Fig. IV-1. Values of $\frac{h}{h_{2D}}$ calculated from Eq. (1) using values of

$$\left[\frac{d\omega}{d\phi}\right]_{\phi=0}$$

obtained from the 80-deg sweep curve of Fig. IV-1 are shown in Fig. IV-2. Also shown are data taken from Ref. 29 for a blunt-nosed round-edged 80.0-deg sweep delta wing. These data indicate that at low angles of attack (15 deg or less) the sharp-edged delta flow model of Ref. 27 is not valid and heat-transfer ratio may be below the two-dimensional level. It can also be seen, however, that the data are approaching the sharp-edged delta values as angle of attack is increased to 30 deg.

Note that for angles of attack greater than approximately 30 deg that the value of

$$\left[\frac{d\omega}{d\phi}\right]_{\phi=0}$$

is greater than 1.0. A streamline path illustrating this condition is shown in the sketch in Fig. IV-1. This flow pattern is similar to that produced on an infinite swept cylinder which implies that spanwise strip theory (crossflow theory) may be valid. This is shown to be the case in Ref. 18 where a complete discussion of this approach is given.

Noting the trend of

$$\left[\frac{d\omega}{d\phi}\right]_{\phi=0}$$

with sweep angle and that the present configuration has an 81.5-deg sweep, the following flow models are proposed. These are: two-dimensional flow for α = 10 deg, conical flow for α = 20 deg, and spanwise strip theory for α = 30 to 50 deg. At values of x/L greater than 0.6 the North American orbiter has an effective sweep angle of approximately 60 deg. Values of

$$\left[\frac{d\omega}{d\phi}\right]_{\phi=0}$$

for a 60-deg sweep delta wing in Fig. IV-1 are less than 0.5 at angles of attack of 10 and 20 deg. This indicates that the flow field is close to being two dimensional

$$\left[\frac{d\omega}{d\phi}\right]_{\phi=0} \ll 1,$$

at these angles of attack. On the other hand, the values of

$$\left[\frac{d\omega}{d\phi}\right]_{\phi=0}$$

for 30- to 50-deg angle of attack indicate that the flow is nearly conical

$$\left[\frac{d\omega}{d\phi}\right]_{\phi=0} \approx 1,$$

at these conditions.

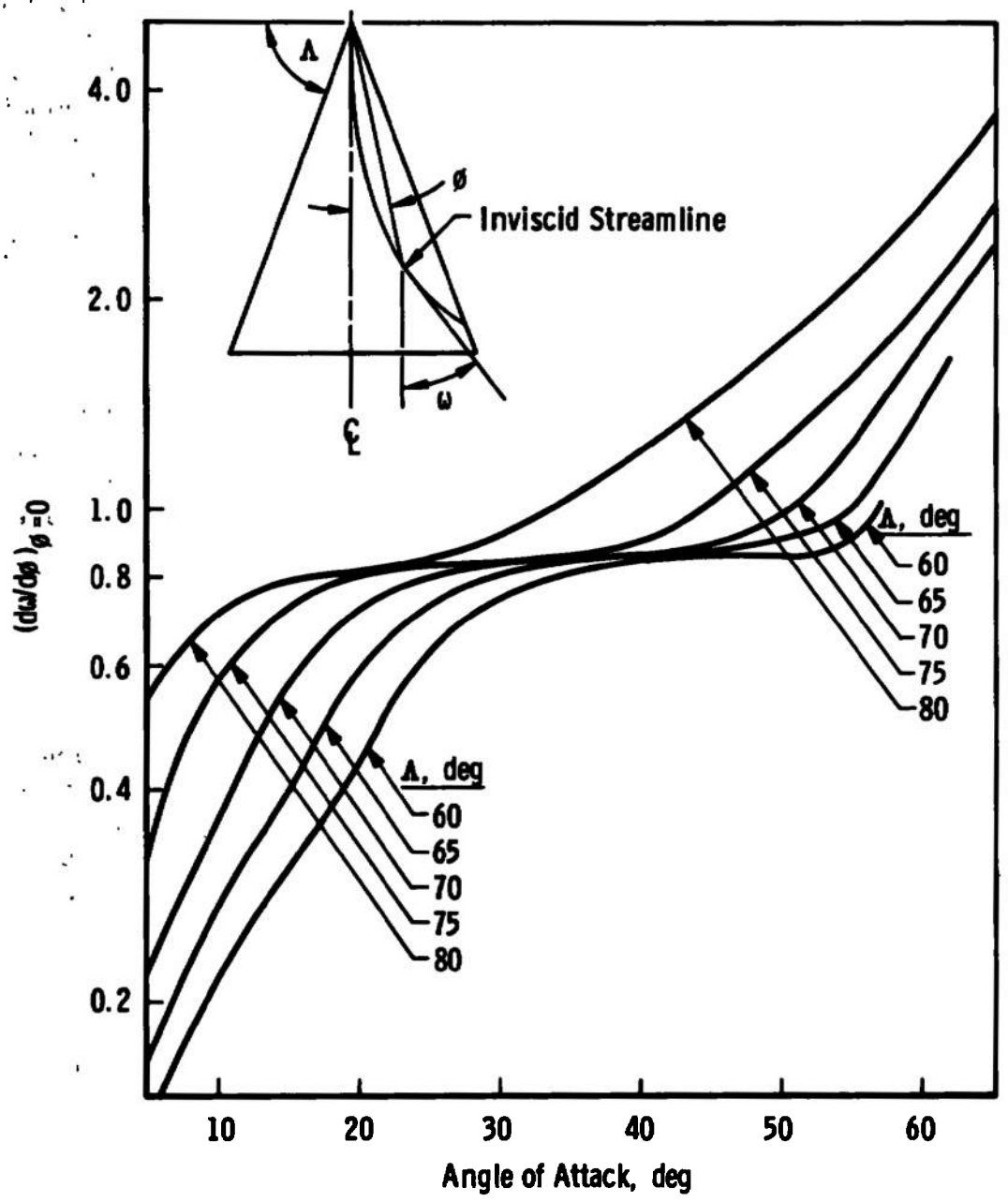

Fig. IV-1 Rate of Change of Inviscid Streamline Angle Along the Centerline of a Sharp Delta Wing, M_∞ = 9.6

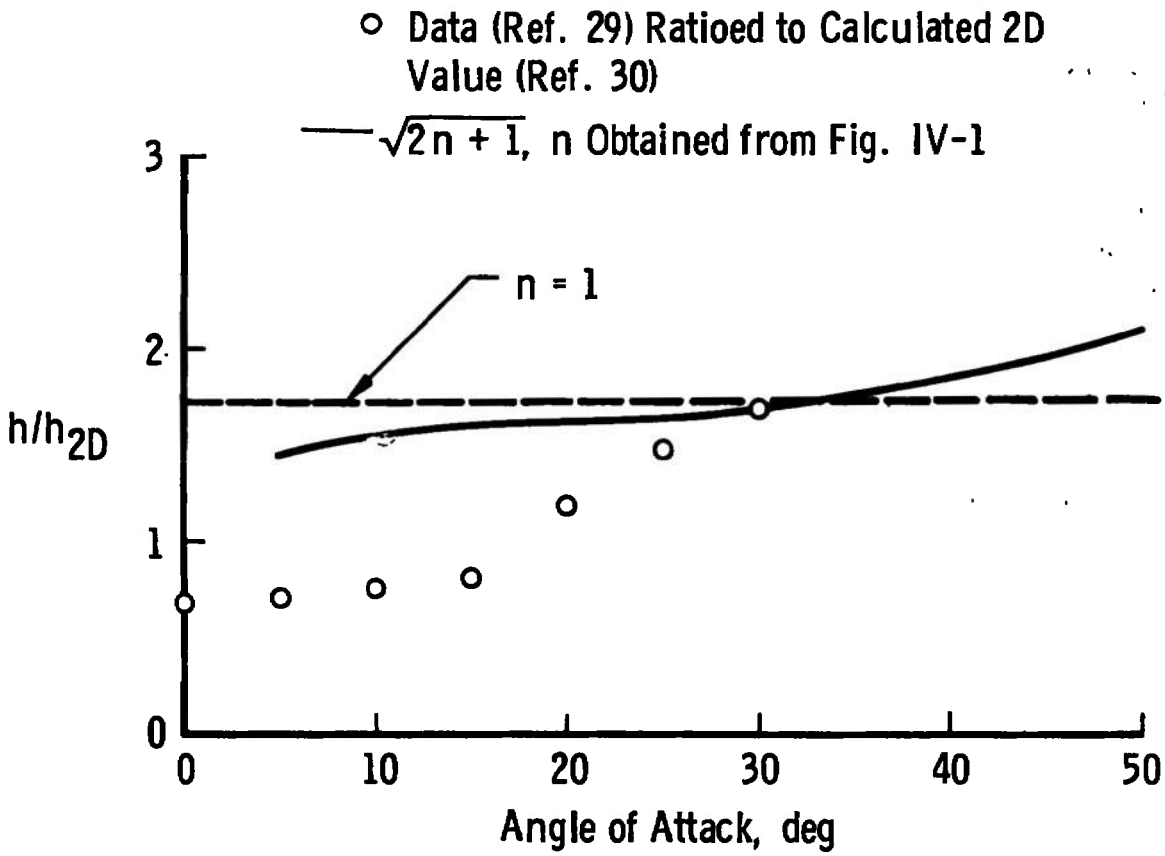

Fig. IV-2 Comparison of Calculated and Experimental Heating Rates on an 80-deg Sweep Round-Edged Delta Wing

APPENDIX V
BOUNDARY-LAYER CALCULATIONS

The boundary-layer calculations presented in this report were obtained from the method of Adams (Ref. 18). The basic calculation procedure was employed in one of two ways, depending upon the flow-field model under consideration. The orbiter centerline flow was shown in Appendix IV to be approximately two-dimensional at 10 deg. At 20 deg the flow was shown to be conical for values of x/L between 0.1 and 0.6 and approximately two-dimensional for x/L greater than 0.6. Since these flows are basically along the body, the calculation procedure of Ref. 18 was used to calculate the boundary layer with the component of velocity normal to the longitudinal axis set equal to zero. Input data were determined as follows.

Surface pressures were determined from experimental data. Boundary-layer edge conditions were then computed using these pressures and the tangent cone shock angles. These values were input into the calculation procedure, along with equivalent axial distances which were determined from the following relations from Ref. 31:

$$\text{laminar} \quad \bar{x}_{eq} = \frac{\int_0^{\bar{x}_\ell} h^2 d\bar{x}}{h^2} \tag{V-1}$$

$$\text{turbulent} \quad \bar{x}_{eq} = \frac{\int_0^{\bar{x}_\ell} h \, d\bar{x}}{h} \tag{V-2}$$

The metric coefficient h is controlled by the rate of streamline spreading. For two dimensional flow h is constant. For radial flow h is equal to r, the local semispan of the body. In the case of crossflow normal to the centerline, h can be approximated by Eq. (4) from Ref. 31, which can be integrated to give

$$h = r\, e^{\int_0^{\bar{x}_\ell} \frac{1}{v_e} \frac{\partial u_e}{\partial s} d\bar{x}} \tag{V-3}$$

To calculate the boundary layer axially along the body, the nose also must be considered. In this case the nose of the body ($x/L \cong 0.1$) has circular cross sections with a curved axial centerline. Arbitrary

assumptions were made regarding the flow on the nose to begin the calculations. In the α = 10-deg case the flow was assumed to be conical, while at α = 20 deg crossflow was assumed.

Using the general form of the equation for the metric coefficient (Eq. 3) and recalling the assumed flow models for x/L > 0.1, the following values of r and $\frac{\partial u_e}{\partial s}$ result.

α = 10 deg			α = 20 deg		
x/L	r	$\frac{\partial u_e}{\partial s}$	x/L	r	$\frac{\partial u_e}{\partial s}$
0 to 0.1	r	0	0 to 0.1	r	Newtonian Cylinder Value
0.1 to 1.0	r at x/L = 0.1	0			
			0.1 to 0.6	r	0
			0.6 to 1.0	r at x/L = 0.6	0

Note that upstream history effects are carried through the calculations in the integrals in Eqs. (1), (2), and (3).

For angles of attack of 30, 40, and 50 deg, the boundary-layer theory was applied in a spanwise strip manner. The details of these calculations are given in Ref. 18.

UNCLASSIFIED

Security Classification

DOCUMENT CONTROL DATA - R & D

(Security classification of title, body of abstract and indexing annotation must be entered when the overall report is classified)

1 ORIGINATING ACTIVITY (Corporate author)

Arnold Engineering Development Center
Arnold Air Force Station, Tennessee

2a. REPORT SECURITY CLASSIFICATION: UNCLASSIFIED

2b. GROUP: N/A

3 REPORT TITLE

HEAT-TRANSFER AND FLOW-FIELD TESTS OF THE NORTH AMERICAN ROCKWELL/ GENERAL DYNAMICS CONVAIR SPACE SHUTTLE CONFIGURATIONS

4 DESCRIPTIVE NOTES (Type of report and inclusive dates)

Final Report - June to September 1971

5 AUTHOR(S) (First name, middle initial, last name)

W. R. Martindale, R. K. Matthews, and L. L. Trimmer, ARO, Inc.

6 REPORT DATE	7a. TOTAL NO OF PAGES	7b. NO. OF REFS
January 1973	95	31

8a CONTRACT OR GRANT NO

b. PROJECT NO

c. Program Element 921E-2

d.

9a. ORIGINATOR'S REPORT NUMBER(S)

AEDC-TR-72-169

9b. OTHER REPORT NO(S) (Any other numbers that may be assigned this report)

ARO-VKF-TR-72-123

10 DISTRIBUTION STATEMENT

Approved for public release; distribution unlimited.

11 SUPPLEMENTARY NOTES

Available in DDC

12 SPONSORING MILITARY ACTIVITY

NASA-MSFC
A&E-AERO-AAE
Huntsville, Alabama 35812

13 ABSTRACT

Aerothermodynamic tests of Phase B space shuttle configurations proposed by North American Rockwell/General Dynamics Convair were conducted at Mach number 8. Test conditions provided both Mach number and Reynolds number simulation for typical ascent and reentry trajectories. This report provides a comprehensive analysis of the major test results and also presents data comparisons with theoretical calculations. Specific areas covered are: ascent heating and shock interference, booster reentry heating and flow fields, and orbiter reentry including leeside heating, windward shock angles and flow fields, windward surface heating, and boundary-layer transition.

DD FORM 1 NOV 65 1473

UNCLASSIFIED

Security Classification

14. KEY WORDS	LINK A		LINK B		LINK C	
	ROLE	WT	ROLE	WT	ROLE	WT
heat transfer						
flow distribution						
tests						
North American Rockwell						
General Dynamics Convair						
space (shuttle)						
configurations						
Mach numbers						
Reynolds numbers						
boundary-layer transition						
interference heating						

AFSC
Arnold AFS Tenn